Data: Author (Year) Title. URI [dataset]

University of Southampton

Faculty of Engineering and Physical Sciences

Zepler Institute

Distributed curvature sensing using Brillouin scattering and multicore fibres

by

Angeliki Zafeiropoulou

Thesis for the degree of Doctor of Philosophy

February 2021

"All human wisdom is summed up in two words: wait and hope"

Alexandre Dumas

University of Southampton

Abstract

Faculty of Physical Sciences and Engineering
Optoelectronics Research Centre

Doctor of Philosophy

Distributed curvature sensing using Brillouin scattering and multicore fibres

by
Angeliki Zafeiropoulou

Optical fibre shape sensing refers to the reconstruction of the shape of an object by using the strain measurements induced to the fibre by the bend. By routing an optical fibre through the structure of interest, the strain induced by the bending can be correlated to the radius of curvature of this structure, thus extracting information about its shape. This emerging new technology can be applied to many different fields varying from medical robotics to the health monitoring of structures leading to significant improvements to the quality of life. Multicore fibres are very good candidates for shape sensing thanks to the integrated 3D coordinate system they offer owing to the fixed position of the cores inside their cladding.

In this thesis a Brillouin Optical Time-Domain Reflectometry (BOTDR) setup was built to interrogate the multicore optical fibres. BOTDR is a single-ended technique that makes its deployment into the field very practical. To overcome the issue of fibre twist during installation, a D-shaped and a flat, multicore fibre were designed and fabricated for use in shape sensing applications.

The fabrication process as well as various ways of handling, cleaving and splicing those novel fibres that present a preferential bend, are analytically described in this work. The D-shaped fibre was used for curvature measurements demonstrating deviations from the real values between 9% and 15%.

Contents

List of Figures

List of Symbols

r_{core}	core radius
r_{cladding}	cladding radius
n_{core}	core refractive index
n_{cladding}	cladding refractive index
R	bending radius
r_i	radial distance of the i-core from the centre of the fibre
y_i	distance of the i-core from the neutral axis
f_B	central Brillouin frequency
δf_B	minimum detectable change in f_B
α	total attenuation rate
α_{Rayleigh}	Rayleigh scattering coefficient
$\alpha_{\text{Brillouin}}$	Brillouin scattering coefficient
δz	spatial resolution
ϵ	strain
κ	curvature
τ_p	pulse width
λ_0	vacuum wavelength
υ_g	group velocity

Declaration of Authorship

I, Angeliki Zafeiropoulou, declare that this thesis entitled, "Distributed curvature sensing using Brillouin scattering and multicore fibres" and the work presented in it are my own and has been generated by me as the result of my own research work.

I confirm that:

1. This work was done wholly or mainly while in candidature for a research degree at this University.
2. Where any part of this thesis has previously been submitted for a degree or any other qualification at this University or any other institution, this has been clearly stated.
3. Where I have consulted the published work of others, this is always clearly attributed.
4. Where I have quoted from the work of others, the source is always given. With the exception of such quotations, this thesis is entirely my own work.
5. I have acknowledged all main sources of help.
6. Where the thesis is based on work done by myself jointly with others, I have made clear exactly what was done by others and what I have contributed myself.
7. Parts of this work have been published as journal and conference contributions listed in the List of Publications.

Signature: ..... Date: .....

Acknowledgements

First and foremost, I am grateful to my academic supervisors Prof. Gilberto Brambilla and Dr. Ali Masoudi for the supervision, guidance and discussions we had throughout the years of my PhD.

A big thanks to all the people of Fibercore for making me feel welcome when I first stepped my foot in the company and everything was so new to me. An even greater thank you though is dedicated to my industrial supervisor Dr. Laurence Cooper for the effective collaboration we had in the fibre fabrication part of the PhD as well as for keeping my spirits high during difficult times. A heartfult thanks goes to Liz Leathem and Tim Hart who both made the transition to the UK and to a company environment a smooth and fun experience.

I would also like to thank all the members of the Metamaterials group and particularly Hao Li, Dimitris Papas, Jinxiang Li, Jie Xu and Dr. Jun-Yu Ou for all the nice chats and experiences we shared together. Dr. Tatev Chalyan, Astghik Chalyan, Prof. Ana Quirce and Sergei Mikhailov made my stay in Brussels during my 3-month secondment a unique experience and greatly contributed to feel at home. Nektaria Chamakou, my lifelong friend was always there for me when I needed her. It is such a great privilege to call all these people my friends.

A heartfelt thank you also goes to Dr. Yongmin Jung for his help and the fruitful discussions we had.

I would like to thank all the people involved in the Innovative Training Network FINESSE for giving me the opportunity of participating in various networking events and workshops around the world. I will be forever grateful to the Marie Skłodowska-Curie Actions for the opportunities they offer to young researchers to pursue research abroad providing the funding and the organisational framework for this to be implemented.

My sincere gratitude goes to Dr. Christopher Emslie, Fibercore's CEO for extending my funding and helping me to carry on my research with a greater comfort.

Last but not least I would like to thank my life partner Dr. Apostolis Zdagkas for his love, understanding, support and help throughout the mutual journey we chose to pursuit in parallel. My parents and brother could not be missing from this list since it was their unconditional love that as always inspired my perseverance, kept me going during the hardest times and drove me to complete one more ambitious goal I set for myself.

Thank you all,

Αγγελική

Dedicated to my father Constantinos, for sparking my interest in science. ...

List of Abbreviations

AOM	**A**cousto- **O**ptic **M**odulator
ASE	**A**mplified **S**pontaneous **E**mission
AWG	**A**rbitrary **W**aveform **G**enerator
BFS	**B**rillouin **F**requency **S**hift
BOP	**B**eginning **O**f **P**ull
BOTDA	**B**rillouin **O**ptical **T**ime **D**omain **A**nalysis
BOTDR	**B**rillouin **O**ptical **T**ime **D**omain **R**eflectometry
BPF	**B**and **P**ass **F**iltre
CSA	**C**ross **S**ectional **A**rea
CW	**C**ontinuous **W**ave
DAQ	**D**ata **A**cquisition
DOFS	**D**istributed **O**ptical **F**ibre **S**ystems
DPP	**D**ifferential **P**ulse **W**idth **P**air
EDFA	**E**rbium **D**oped **F**ibre **A**mplifier
EOM	**E**lectro**O**ptic **M**odulator
EOP	**E**nd **O**f **P**ull
FBG	**F**ibre **B**ragg **G**rating
FC/APC	**F**ibre **C**onnector /**A**ngled **P**hysical **C**ontact
FUT	**F**ibre **U**nder **T**est
FWHM	**F**ull **W**idth at **H**alf **M**aximum
IF	**I**ntermediate **F**requency
MCF	**M**ulti**C**ore **F**ibre
MCVD	**M**odified **C**hemical **V**apour **D**eposition
MEMS	**M**icro **E**electro**M**echanical **S**ystem
MFC	**M**ass **F**low **C**ontrollers
MFD	**M**ode **F**hield **D**iameter
NA	**N**umerical **A**perture
OFDR	**O**ptical **F**requency **D**omain **R**eflectometry
OTDR	**O**ptical **T**ime **D**omain **R**eflectometry
PM	**P**olarisation **M**aintaining
SBS	**S**timulated **B**rillouin **S**cattering
SMF	**S**ingle **M**ode **F**ibre
SNR	**S**ignal to **N**oise **R**atio
SRS	**S**timulated **R**aman **S**cattering
TLS	**T**unable **L**aser **S**ource

WDM	**W**avelength **D**ivision **M**ultiplexing
YIG	**Y**ttrium **I**ron **G**arnet
7CF	**7**core **F**ibre

Chapter 1

Introduction

1.1 Motivation for shape sensing

Optical fibre sensors offer many advantages over the conventional strain gauges such as small dimensions, robustness, ability to be used in inaccessible places, and immunity to external electromagnetic fields. A pioneering field that emerges from the use of optical fibres for sensing purposes is the field of shape sensing. Shape sensing refers to the reconstruction of the shape of an object by using the strain that has been induced to the fibre by the bend. This requires at least two sensing elements for a 2D representation, or three in case we are interested in the 3D reconstruction of the structure of interest.

Multi-Core Fibres (MCFs) are considered very good candidates for this new technology due to their intrinsic advantages, such as well-defined core separation and isothermal behaviour which follows from the fact that all cores are located within the same cladding. In other words, one core can be considered as a sensing element and so a fixed coordinate system can be applied to two or three of them. Despite of that, it is very common for the fibre to get twisted during its installation on the structure of interest resulting in a subsequent twist of the cores. As a result of that the fixed coordinate system gets distorted rendering the determination of the bending direction invalid.

The purpose of this PhD project is the design of new multi-core fibres optimised for shape sensing applications. The ultimate goal is the creation of a multi-core fibre that will self-orientate when deployed along the structure of interest resulting in a suppression of the twist rendering it ideal for shape sensing applications.

At the initial stage a standard commercial 7CF was tested and the twist of the cores became prominent on the Brillouin Gain Spectra. The first design iteration resulted in a D-shaped fibre aiming to define a preferential bending direction of the fibre whilst retaining the core layout of the existing commercial product. After the first results showed a significant reduction of twists, a further refinement followed, based on the fabrication of a flat fibre with the same core layout as the standard 7CF. The last fibre completely suppressed the twist rendering it an ideal candidate for field deployment and shape reconstruction.

The fabrication of all the multi-core fibres used in this project, took place at the Fibercore facilities in Southampton UK, while the interrogation setup used for the shape sensing tests was developed anew at the Optoelectronics Research Centre,

Univesity of Southampton. The project described in this thesis was a part of a bigger collaborative Marie Sklodowska-Curie Innovative Training Network (ITN), called FINESSE, involving 26 European Universities, research centres and industrial partners that teamed up together for the development of a new optical "artificial nervous system".

FINESSE's aim (FIbre NErvous Sensing SystEms) was to mimic the nervous system of living bodies by turning man-made and natural structures into objects that are sensitive to external stimuli owing to advanced distributed fibre-optic sensor technology, with the objective to give early warning in case of possible danger or occurrence of damage.

Curvature sensing, is the first logical step to be investigated before the full 3D shape reconstruction is attempted and is particularly useful, as it was mentioned before, in the integrity monitoring of structures such as pipelines, tunnels dams and cables to name just a few. More specifically, there are many challenges in the offshore subsea power cable industry with a significant number of cable failures to have been recently reported [1], mainly attributed to cable laying issues and mechanical damage such as over-bending or over tensioning. During installation of such a cable, the monitoring of its strain can help preventing its over-tension ensuring that it does not bend below its minimum bending radius. Typical minimum bending radii for subsea power cables reported in the literature is 5m with performance requirements of spatial and strain resolution less than 4m and $100\mu\epsilon$ respectively [2]. Also, another important application of curvature sensing can be found in the monitoring of the lateral deformation of the railway tracks due to naturally occurring phenomena such as landslides, avalanches, mud flows or rock slides. The lateral displacements that are expected in this type of deformation are in the range of a few cm [3].

In this project, Brillouin Optical Time-Domain Reflectometry (BOTDR) was the technique selected for the interrogation of the multi-core fibres since it is well suited for long range sensing, rendering it appropriate for the shape reconstruction of civil engineering structures or subsea cables. Lastly it requires access from one end of the fibre only, rendering its implementation in the field more practical.

1.2 Research Objectives

The aim of this research project was to demonstrate shape sensing capabilities using multicore fibres that would be interrogated using Brillouin Optical Time-Domain Reflectometry technique. In the framework of this PhD research, the experimental setup would be developed anew and optimised at the Optoelectronics Research Centre, University of Southampton. The performance of the current commercially available multi-core fibres would be investigated and new designs would be conceived and fabricated at Fibercore, to eliminate the limitations of the standard MCF. The ultimate goal was the optimisation of the performance of the optical fibre sensor for the sensing regime the BOTDR technique targets.

1.3 Thesis Outline

The thesis is organised in six chapters and a brief description of each is given below:

In chapter 2 a basic theory of optical fibres is given and various methods of fabricating spatial multiplexing/demultiplexing devices needed for multicore fibres are briefly discussed. The light scattering mechanisms in optical fibres are mentioned providing the necessary background to the reader to understand the shape sensing techniques described in a next section. Finally, a comparison between the different shape sensing methods is given and the applications of this emerging technology are discussed.

Chapter 3 discusses the Modified Chemical Vapour Deposition method used for fabricating the multi-core fibres used in this thesis. The fabrication stages of the flat fibre preform as well as the fibre draw process are described in detail. The fabrication of the D-shaped fibre is also presented in the last section of this chapter.

In chapter 4, curvature sensing using a D-shaped fibre is demonstrated. The principle of operation of a sensor based on a multi-core fibre is described and the Brillouin Optical Time-Domain Reflectometry setup used for interrogating the fibre is discussed.

In chapter 5 various methods for cleaving and splicing a flat to flat fibre are presented and the challenges associated to its handling as well as ways to overcome them, are discussed. Three-beam test results using this unique multi-core fibre are also presented in the final section of the chapter.

Finally chapter 6, summarises the research and offers recommendations about ways to expand the work presented in this thesis.

Chapter 2

Optical fibre sensing: Overview

2.1 Introduction

In this chapter the principles of the three scattering mechanisms used in Distributed Optical Fibre Sensors (DOFS) will be described, before the detection principle of Brillouin backscattering is analysed. The conditions under which non-linear phenomena may arise are discussed and the basic shape sensing equations are derived.

2.2 Basic theory of optical fibres

Numerical Aperture (NA) is defined as the limiting angle $< \theta_\alpha$ for rays to be guided inside an optical fibre [4]. For the case of a step index, multi-mode fibre, with a core diameter between 50μm and 100μm, geometric optic applies and the acceptance angle θ_α can be expressed as:

$$\theta_\alpha = \arcsin\sqrt{n^2_{\text{core}} - n^2_{\text{cladding}}}, \tag{2.1}$$

where the square root element is the numerical aperture of the fibre,

$$NA = \sin\theta_a = \sqrt{n^2_{\text{core}} - n^2_{\text{cladding}}}. \tag{2.2}$$

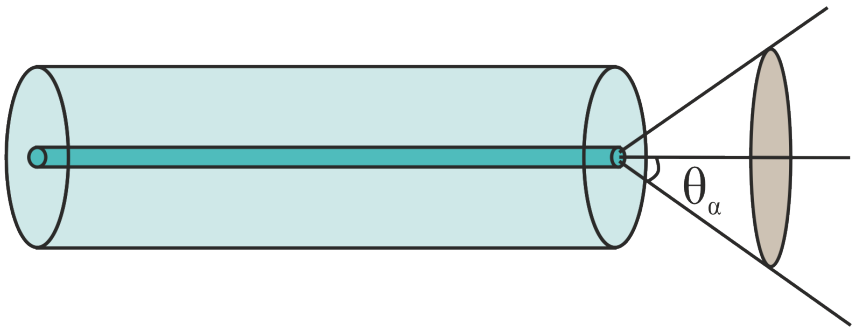

FIGURE 2.1: Acceptance and exit cone of a fibre.

In the case of a step index single-mode optical fibre with a typical core size of 8μm-9μm, the core dimension is comparable to the wavelength of light. As a result, the

ray optics approximation starts to break down, and the NA can be calculated by rigorous electromagnetic methods.

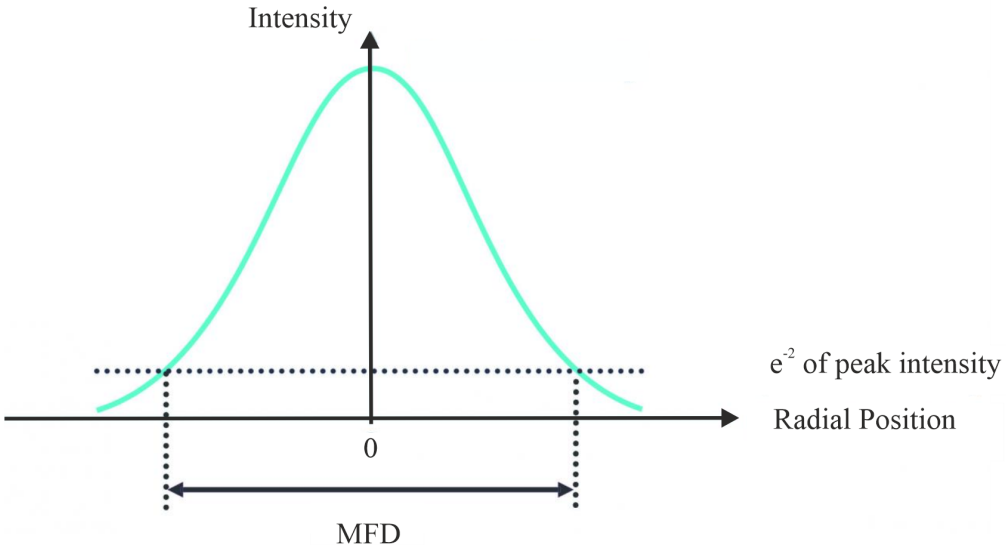

FIGURE 2.2: Gaussian beam approximation of the fundamental LP_{01} mode. The Mode Field Diameter is defined as the distance from the centre where the intensity drops by $1/e^2$.

V-number (V) or normalized frequency is the fundamental relationship between numerical aperture, operating wavelength and core radius in step-index fibres. By definition V=2.405 at the cut-off wavelength of every single-mode fibre waveguide. When the V-number is greater than 2.405 the fibre will support multiple modes. On the contrary, if the V-number is less than 2.405 then the light propagated through the fibre will be single-mode [4],

$$V = \frac{2\pi r_{\text{core}} NA}{\lambda_0} \tag{2.3}$$

where

- r_{core} is the core radius
- NA is the numerical aperture
- λ_0 is the vacuum wavelength

$$V < 2.405 \;\text{ or }\; \lambda > \lambda^{\text{cutoff}} \quad \text{single-mode operation} \tag{2.4}$$

$$V > 2.405 \;\text{ or }\; \lambda < \lambda^{\text{cutoff}} \quad \text{multimode operation} \tag{2.5}$$

Mode Field Diameter (MFD) MFD is typically defined as the radial position where intensity falls to $1/e^2$ of the peak intensity. For a step index fibre the MFD is given by Marcuse's empirical formula [5],

$$MFD = r_{\text{core}} \cdot \left(0.65 + \frac{1.619}{V^{3/2}} + \frac{2.879}{V^6}\right) \tag{2.6}$$

where r_{core} is the core radius and V the normalised frequency (V-number) of the fibre.

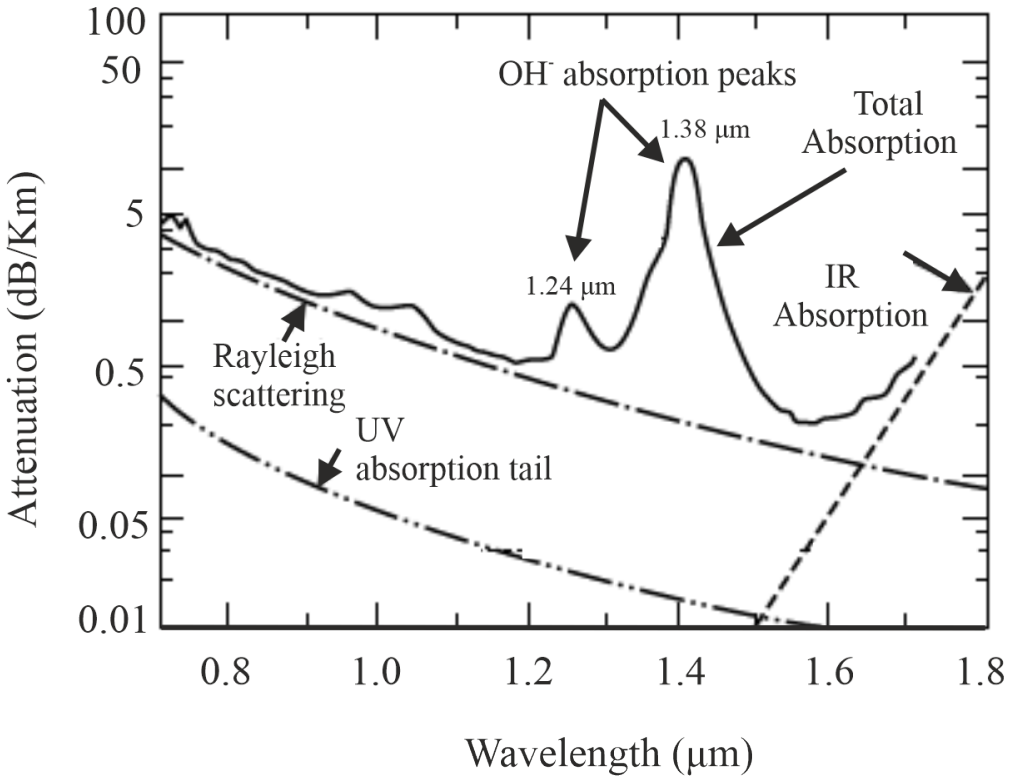

FIGURE 2.3: Attenuation spectrum for a typical germano-silicate single-mode fibre. Figure by [6].

Loss mechanisms in glass There are four main contributions to the attenuation of a fibre [4].

- **UV absorption**

  At the short wavelength end of visible spectrum (blue and violet) the leading factor is contributions from electronic resonances of silica glass.

- **Rayleigh scattering**

  At the visible range and in the first and second telecommunication window Rayleigh scattering dominates. Rayleigh scattering arises from thermodynamically driven fluctuations in the density of the glass that are frozen inside the glass during the draw as the glass cools.

- **Absorption by impurities**

  The most important impurity affecting fibre loss is the OH^- ion that has a fundamental vibration absorption peak at 2.43μm. The overtones of this OH^- absorption peak are responsible for the dominant peak at 1.39μm and a smaller at 1.23μm.

- **IR absorption**

  Beginning at around 1.6μm the contribution from vibrational resonances overtakes the Rayleigh contribution and becomes the dominant attenuation mechanism.

2.3 Multi-core fibres

Multi-core fibres (MCF) were first exploited as a way to increase the data-carrying capacity of a single optical fibre [7], [8], [9]. MCF contain multiple cores in the same cladding allowing for parallel paths resulting in an increase in the bandwidth capacity. MCFs can be divided into two categories: 1) Weakly-coupled and 2) Strongly-coupled MCF. The first type refers to a MCF where each core is an individual waveguide with low interference between adjacent cores. The second type involves MCF where the cores are close enough to allow coupling between them [10]. Apart from their use in the telecom industry the MCF has also been used for sensing applications.

The idea of using multi-core fibres for sensing applications traces back to the late 70s. Meltz and Snitzer were granted patents in 1981 for a fibre optic strain sensor that relies on the cross-talk phenomenon in a two-core fibre. As light propagates along one core in the optical fibre, changes in strain due to hydrostatic pressure cause a change in the relative energy that is cross-coupled between the cores [11]. Gander's work published in 2000, is the first report of a bend sensor based on Bragg gratings written in multi-core fibres [12]. FBGs were written simultaneously in two-cores of a 4-core fibre for one-axis measurements and a gradient of 48.9pm/m^{-1} corresponding to a strain sensitivity of 0.997pm/$\mu\epsilon$ is reported. In 2003 is reported for the first time the use of FBGs for two-axis curvature measurement in three separate cores of a 4-core multi-core fibre [13]. In 2006 a patent by Luna Innovations describes a fibre optic position and shape sensing device based on a 3-core weak-coupled multi-core fibre with an array of FBGs inscribed into each core [14]. Villatoro et al. [15] used coupled-core MCF to detect vibrations.

The advantage of using MCF for sensing, rely on the well-defined structure thanks to the fixed position of the cores inside the cladding. The fact that there are cores that are located away from the geometric centre of the fibre makes them sensitive to strain and as a result to bend. It is also possible to distinguish the bending direction and that makes the MCF the perfect candidate for curvature and 3D shape sensing. By measuring the differential strain between cores the shape of

the fibre can be retrieved. One more advantage is the implementation of multiple distributed techniques in the same fibre [16].

For the purpose of shape sensing tests the MCF design was based on parameters of the commercially available MCF. More specifically, both the D-shaped and the flat fibre had an *NA* of 0.2, a core pitch of 35μm and 6 cores in a hexagonal geometry surrounding the central core. The NA of the multi-core is higher than that of a standard SMF to increase the modal confinement and mitigate the crosstalk[17]. Although a minimum number of 3-cores is required to infer the shape of a curve in the 3D space, the use of a larger number offers redundancy thereby reducing the error in the calculations and improving the reliability of the measurement [18], [19].

To couple light from a multi-core fibre to a standard SMF a spatial demultiplexer/multiplexer or fanin/fanout is used. There a few ways to achieve this coupling mainly based on free-space schemes, waveguide coupling or fibre-tapers [20]. In the next two sections the focus will be on the latter two since these are the fabrication methods used for the fanout devices of this project.

2.3.1 Fanout devices based on waveguide coupling

In this technique a femto-second laser beam is tightly focused on the dielectric material to directly write three-dimensional waveguide structures in its volume. The non-linear absorption of the energy from the dielectric material induces a series of processes such as shockwave propagation and thermal diffusion that after the resolidification of the material induce permanent changes in its structure. These structural changes are reflected to a change in the refractive index of the irradiated region [21].

Fig. 2.4 shows the fanout device as well as the way the device is coupled to the MCF and to the SMF ends [22], [23]. The SMF fibres are placed on a V-groove array which is then glued onto the fanout device using UV curing epoxy [24]. Likewise the MCF is bonded to the MCF end of the fanout and the device is packaged. This technique has been commercialised by Optoscribe [25].

The advantages of inscribing the waveguides inside the glass are the compact size of device as well as the highly accurate core positioning. This technique also offers significant scalability in the manufacturing process enabling low cost-high volume production. Also arbitrary configurations of the cores are possible (e.g non circularly symmetrical patterns such as 2x4). Typical insertion losses of this type of fanout are $<$ 1.5dB for a 7-channel fanout however this is dependent on the fibre.

2.3.2 Fanout devices based on fibre-tapers

The flat fibre fanout was fabricated by Chiral Photonics. The method used for this type of waveguide is based on the "vanishing core concept" [27]. More specifically a custom-made preform is fabricated containing seven core regions with refractive index n_1 surrounded by sections of slightly lower refractive index n_2 that are in turn

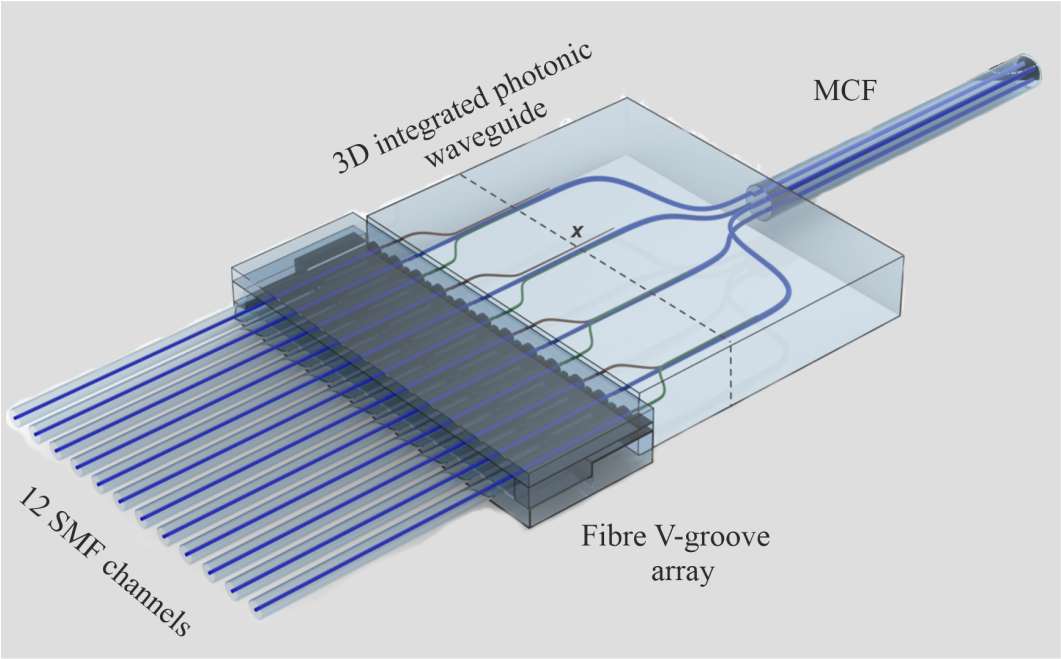

FIGURE 2.4: Schematic of the fanout demultiplexer. The device allows each core of a MCF to be addressed individually through a single mode fibre held in a fibre V-groove array. Figure by [26].

surrounded by cladding material with refractive index of n_3, where $n_1 > n_2 > n_3$. Fig. 2.5 (b),(c) show how one "core" looks like.

One side of the preform is then tapered as shown in the Fig. 2.5(a). As the preform is tapered [28], the inner core becomes too small to support propagation, Fig. 2.5(d). The waveguide then acts as if it had a single core of index close to n_2 surrounded by a cladding of lower index n_3. The indices of refraction are chosen in such a way so as for the two sides to have a matching NA and the sizes of the inner and outer core are designed in such a way for the two fibres to have the same MFD. On the untapered side, the inner core guides the light and is matched in this case to a standard SMF. The SMF pigtails are integrated directly into the untapered preform, ostensibly via standard SMF-SMF splices. The tapered side of the preform is spliced to a multi-core fibre using a commercial PM splicer, Fig. 2.5(d) [29], [30].

The advantage of this technique is its compactness as well as the minimisation of the losses in the interfaces, due to the fact that everything is fibre-based. The average insertion loss per channel, not including the connectorisation, is 0.6dB for a 7-channel fanout however this is dependent on the fibre.

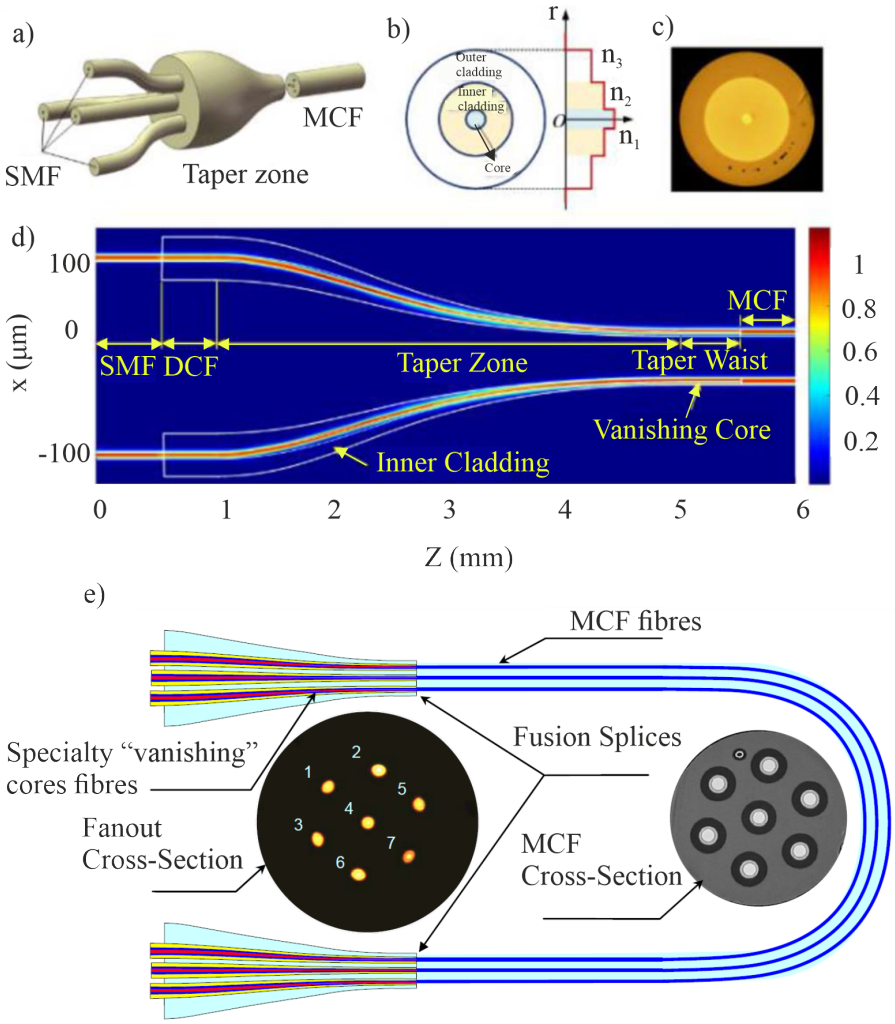

FIGURE 2.5: Configuration of a multi-core fibre fanout component a) A four-core fibre fanout device is fabricated by four double cladding fibres embedded in a fibre substrate. The fanout device, is typically spliced to standard SMF in its wide end and connected with a multi-core fibre in its narrow end b) The double cladding fibre has a central core, an inner cladding, and an outer cladding, with refractive indices of n_1, n_2, and n_3, respectively; c) Cross section of the double-clad fibre; d) Depiction of the mode field propagation and the vanishing core process in the fibre coupler device. The central core (n_1) can support a single propagating mode in the wide end. However, in the narrow end the central core is vanishing and the inner cladding (n_2) serves as a fibre core to ensure efficient optical mode field transformation between the narrow end and the connected multi-core fibre; e)"Vanishing" core concept. The tapered side of the preform is fusion spliced to the multi-core fibre end. Figure adapted by [29],[27].

2.4 Light scattering in Optical Fibres

2.4.1 Rayleigh scattering

Rayleigh scattering is the dominant scattering mechanism in an optical fibre. It results from inhomogeneities occurring in a small scale compared to the wavelength

of light. These inhomogeneities arise from density fluctuations and compositional variations which are frozen into the glass during cooling, resulting in refractive index fluctuations [31]. As the fibre is drawn, it is cooled very fast resulting in a density distribution inside the glass that does not correspond to room temperature. Instead the distribution of density is frozen in a degree of disorder corresponding to a higher temperature which is called fictive temperature [32]. Although an optimised fabrication process can reduce the size and concentration of these inhomogeneities, it cannot eliminate them since a degree of disorder will always remain in the glass due to its amorphous structure. Rayleigh scattering is characterised by an attenuation coefficient which is proportional to $1/\lambda^4$ and is therefore dominant to short wavelengths. This coefficient is given by [33]:

$$\alpha_{\text{Rayleigh}} = \frac{8\pi^3}{3\lambda_0^4} n_{\text{core}}^8 p^2 \beta_c K T_F, \tag{2.7}$$

where λ_0 is the vacuum wavelength, n_{core} is the core refractive index, p is the average photoelastic coefficient, T_F is the fictive temperature, β_c is the isothermal compressibility in T_F and K is the Boltzmann constant. The photoelastic effect in a material couples the mechanical strain to the optical index of refraction. More specifically the photoelastic coefficient p relates the change in the inverse permittivity tensor to the strain tensor [34]. The isothermal compressibility β_c is a measure of the relative volume change of the solid as a response to a pressure [35]. Tables 2.1 contains the physical parameter of silica for a standard single-mode fibre.

Description	**Symbol**	**Value**
Core refractive index	n	1.46
Average Photo elastic coefficient	p	0.286
Fictive Temperature	T_F	1950K
Isothermal Compressibility at T_F	β_c	$7 \cdot 10^{-11}\text{m}^2\text{N}^{-1}$
Boltzmann constant	K	$1.381 \cdot 10^{-23}\text{J} \cdot \text{k}^{-1}$

TABLE 2.1: Physical parameters of silica for a standard single-mode fibre [31].

One more type of scattering is Mie scattering. Mie scattering is due to homogeneities that are comparable or larger than the wavelength of light. In glass, such defects could be created in the core-cladding interface, due to diameter fluctuations or due to bubbles in the fibre. However in commercial fibres the effects of Mie scatterings are insignificant. In the Modified Chemical Vapour Deposition process which is the technique used for the fabrication of the MCF of this research, there is a perfectly clean interface between core and cladding, with no roughness. Also the diameter control of the fibres is better than about 0.3μm so the diameter fluctuation is insignificant.

2.4.2 Optical Time-Domain Reflectometry (OTDR)

A typical OTDR setup is depicted in Fig. 2.9. Light from a pulsed laser is sent though a coupler into the fibre under test where it gets scattered in all directions. The backscattered signal is then received by a detector and analysed by an oscilloscope.

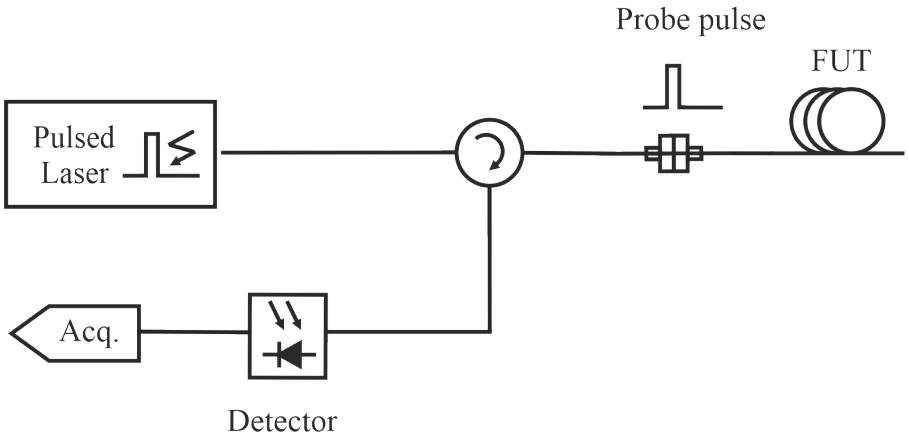

FIGURE 2.6: OTDR basic configuration. A probe pulse travels down the fibre and gets scattered due to the various attenuation mechanisms. A fraction of the scattered light that falls within the acceptance angle of the fibre is captured in the reverse direction and is directed to a detector.

P_{BS} is the backscattered power returning to the launching end of the fibre at time $t = 2z/v_g$ [32].

$$P_{BS} = \frac{dE_{\mathrm{BS}}}{dt} = \frac{v_g}{2} \cdot E_p(0) \cdot \alpha_{\mathrm{Rayleigh}} \cdot B(z) \cdot e^{-2\alpha z} \tag{2.8}$$

where

- v_g is the group velocity of the probe pulse in the fibre.
- $E_p(0)$ the energy of the pulse at location $z = 0$. For a rectangular, finite duration, probe pulse of peak power P_p, the pulse energy is $E_p(0) = P_p(0) \cdot \tau_p$ where $P_p(0)$ is the average power of the pulse and τ_p is the duration of the pulse.
- $\alpha_{\mathrm{Rayleigh}}(z)$ is the Rayleigh scattering coefficient as a function of distance z.
- $B(z)$ is the fraction of captured power is the proportion of the total energy scattered at z in the return direction and is given by $B = (NA)^2/4n^2_{\mathrm{core}}$.
- α is the total attenuation rate at which the forward pulse energy is attenuated and it is expressed in dB/km.

The spatial resolution of an OTDR system is affected by the input pulse duration. For a pulse width of τ_p propagating along the fibre, the spatial resolution corresponds to half of that pulse width:

$$\delta z = \frac{c}{n_{\text{core}}}\frac{\tau_p}{2} \Rightarrow \delta z(\text{m}) = \frac{\tau_p(\text{ns})}{10}. \tag{2.9}$$

where the last term is a simplified relation for the case of the standard silica fibre where $n_{\text{core}} \sim 1.5$.

2.4.3 Raman scattering

In Raman scattering, incoming photons are scattered by the molecules which undergo a transition between two vibrational states. If the scattered photon is down-shifted in frequency, the excess energy is used to excite the molecule into a higher vibrational mode (Stokes wave). This is equivalent with the creation of a phonon. In the case that the scattered photon is up-shifted (anti-Stokes wave), it has gained its energy from a molecular de-excitation. That is equivalent to an absorption of a phonon. The frequency shifts associated with Raman scattering are in the THz range and the principal application of this type of inelastic scattering is temperature sensing [36].

2.4.4 Brillouin scattering

The atoms in a solid (such as glass) are tightly bound to each other. As a result the displacement of one or more atoms from their equilibrium position gives rise to a collective oscillation, called a phonon, of all the atoms in the arrangement. This oscillation, is essentially a periodic change in the the density of the glass. Brillouin scattering occurs from the density fluctuations which are due to pressure variations. Pressure fluctuations or sound waves propagate through the medium and hence, light scattered from them will be Doppler-shifted (inelastic scattering process)[37].

Brillouin scattering is associated to the acoustic phonons of the material and the frequency shifts observed are $\sim$ 11GHz at $\sim$ 1530nm. The quantum mechanic description, involves the interaction of an incident photon (energy = hf_{incident}, momentum = $\hbar\mathbf{k}_{\text{incident}}$) a scattered photon ($hf_{\text{scattered}}, \hbar\mathbf{k}_{\text{scattered}}$) and a phonon ($hf_{\text{phonon}}, \hbar\mathbf{k}_{\text{phonon}}$). A phonon is either created or annihilated.
In the case of the Stokes component, the scattered photon has lower energy than the incident one. This energy difference goes to the creation of a phonon. So, the conservation of energy and momentum denotes [36],

$$\begin{aligned} f_{\text{stokes}} &= f_{\text{incident}} - f_{\text{phonon}}, \\ \mathbf{k}_{\text{stokes}} &= \mathbf{k}_{\text{incident}} - \mathbf{k}_{\text{phonon}}. \end{aligned} \tag{2.10}$$

Likewise in the case of Anti-Stokes, the scattered photon has higher energy than the incident one. This excess of energy is provided through the absorption of a phonon. Likewise, the conservation of energy denotes,

$$f_{\text{anti-stokes}} = f_{\text{incident}} + f_{\text{phonon}}, \qquad (2.11)$$
$$\mathbf{k}_{\text{anti-stokes}} = \mathbf{k}_{\text{incident}} + \mathbf{k}_{\text{phonon}}.$$

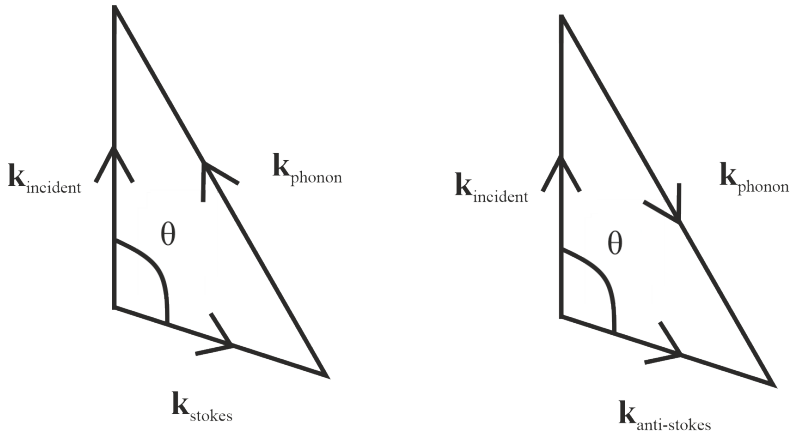

FIGURE 2.7: Conservation of momentum diagram for Stokes and anti-Stokes Brillouin scattering $|\mathbf{k}_{\text{stokes}}| = |\mathbf{k}_{\text{anti-stokes}}| = |\mathbf{k}_{\text{incident}}|$.

Since the frequency shifts involved in the Brillouin scattering are small, we can assume that $|\mathbf{k}_{\text{stokes}}| = |\mathbf{k}_{\text{anti-stokes}}| = |\mathbf{k}_{\text{incident}}|$. From the geometry of Fig. 2.7 it can be seen that for both Stokes and anti-Stokes components [36],

$$|\mathbf{k}_{\text{phonon}}| = \frac{2 \cdot \pi \cdot f_{\text{acoustic}}}{\upsilon_{\text{acoustic}}} = 2\,|\mathbf{k}_{\text{incident}}| \sin\left(\frac{\theta}{2}\right) = 2\left(\frac{2 \cdot \pi \cdot n_{\text{core}}}{\lambda_{0,\text{ incident}}}\right) \sin\left(\frac{\theta}{2}\right),$$
$$f_{\text{acoustic}} = \frac{2 \cdot \upsilon_{\text{acoustic}} \cdot n_{\text{core}}}{\lambda_{0,\text{ incident}}} \sin\left(\frac{\theta}{2}\right).$$

where n_{core} is the core refractive index and θ is the scattering angle. In the case of the forward scattering ($\theta = 0$) the frequency shift reduces to zero, while for the backward scattering ($\theta = \pi$) the frequency shift maximises to

$$f_{\text{acoustic}} = \frac{2 \cdot \upsilon_{\text{acoustic}} \cdot n_{\text{core}}}{\lambda_{0,\text{ incident}}}. \qquad (2.12)$$

The above equation shows that the Brillouin shift depends upon the acoustic velocity in the fibre (which in turn depends on the Young's modulus E of the material, the Poisson ratio μ and the density ρ [38]) as well as the fibre refractive index. Since all the above parameters are dependent on temperature and strain, the frequency shift is also a function of temperature and strain. Hence the Brillouin frequency shift provides information about the strain and temperature that caused it. The next section will explain in details how the strain information can be used for determining the shape of an object.

The Brillouin scattering coefficient is given by [39]

$$\alpha_{\text{Brillouin}} = \frac{8\pi^3}{3\lambda_0^4} n_{\text{core}}^8 p^2 KT(\rho \upsilon_{\text{accoustic}}^2)^{-1}, \tag{2.13}$$

where T is the absolute temperature and ρ is the mean density of the fibre.

The intensity of the Brillouin backscattered light at the front-end of the fibre is given by [39]

$$P_{BS} = \frac{v_g}{2} \cdot E_p(0) \cdot \alpha_{\text{Brillouin}} \cdot B(z) \cdot e^{-2\alpha z} \tag{2.14}$$

where $\alpha_{\text{Brillouin}}$ is the Brillouin scattering coefficient. The typical value of the Brillouin scattering coefficient for a silica based fibre is $\alpha_{\text{Brillouin}} = 1.17 \cdot 10^{-6} m^{-1}$ [39].

Fig. 2.8 depicts the three scattering processes happening in a fibre (not in scale). It is also noted that the total Brillouin power is a factor of ~ 30 smaller than the Rayleigh power [36].

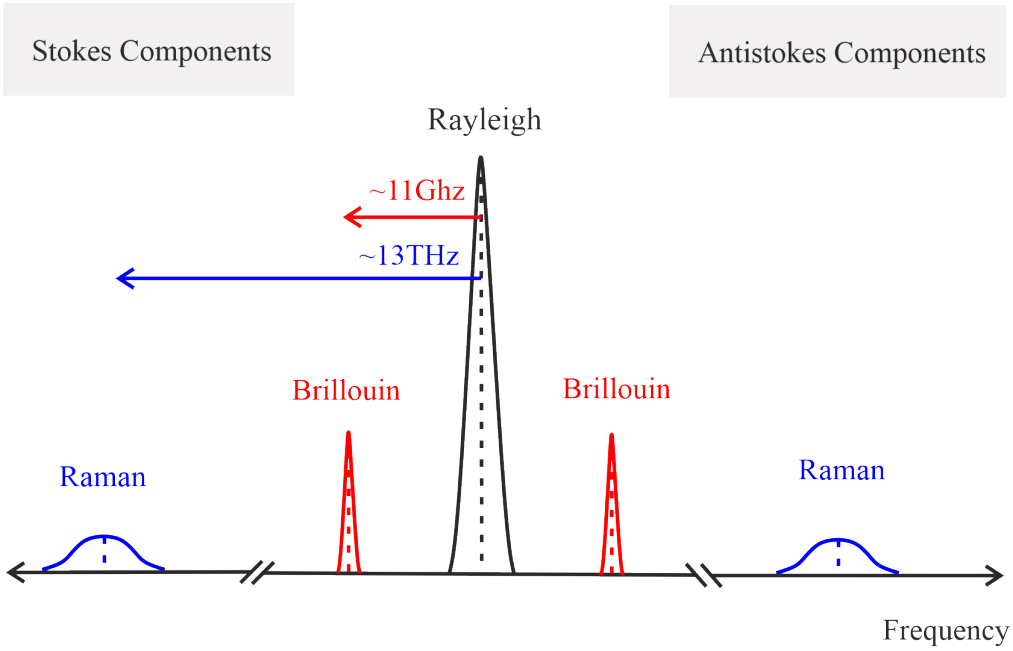

FIGURE 2.8: Schematic spectrum of the three scattering processes happening in an optical fibre. Rayleigh scattering is an elastic process. The Brillouin and Raman are inelastic scattering processes with a frequency shift of 11GHz and 13THz respectively relative to Rayleigh.

2.4.5 Stimulated scattering and non-linear effects

When the power of the pump laser beam is intense enough, that may lead to non-linear phenomena such as Stimulated Raman Scattering (SRS) and Stimulated Brillouin Scattering (SBS). In order to avoid non-linearity effects, the input power entering the sensing fibre should be less than the SRS or SBS threshold, whichever is

smaller.

The threshold for Continuous Wave (CW) stimulated Raman scattering (SRS) defined as the input pump power for which the Stokes power becomes equal to the pump power at the fibre output, is given, approximately, by [36]

$$P_{\text{threshold}}^{\text{SRS}} = \frac{16 A_{\text{eff}}}{g_{\text{R}} L_{\text{eff}}}, \tag{2.15}$$

where A_{eff} is the effective mode field area, defined as $A_{\text{eff}} = \pi(\text{MFD}/2)^2$ for a Gaussian beam, MFD is the Mode Field Diameter of the fibre, g_{R} is the Raman gain coefficient, and L_{eff} is the effective interaction length.

The relationship for the stimulated Brillouin scattering threshold is given by a similar equation [36],

$$P_{\text{threshold}}^{\text{SBS}} = \frac{21 A_{\text{eff}}}{g_{\text{B}} L_{\text{eff}}}, \tag{2.16}$$

where g_B is the Brillouin gain coefficient.

The effective interaction length L_{eff} is always shorter than the actual length of the fibre L due to losses [40] and is given by [36],

$$L_{\text{eff}} = \frac{1}{\alpha_p}\left[1 - e^{(-\alpha_p L)}\right], \tag{2.17}$$

where α_p is the attenuation coefficient ($\sim 5 \cdot 10^{-5} m^{-1}$ for silica fibre). However, in case a pulse is sent instead of a continuous wave, the interaction length has to be calculated differently for each type of scattering. In case of Brillouin scattering, which is a backward propagating process, the interaction length L_{int} will be half of the fibre length occupied by the pump pulse or the fibre length itself, whichever is smaller. Stimulated Raman scattering on the other hand, is a forward propagating process with a high free space wavelength shift of around 100nm for 1550nm pump. Due to the material's dispersion, after a walk off distance L_w the Raman photons are no longer coincident with the pump photons.

The "walk off distance" L_w is given by [36]

$$L_w = \frac{\tau_p}{D \cdot \Delta\lambda}, \tag{2.18}$$

where τ_p is the pump pulse duration, $\Delta\lambda$ is the difference in wavelength (~ 100 nm) between the pump and Raman Stokes signal and D is the fibre's material dispersion parameter (typically $0.02\text{ns} \cdot \text{nm}^{-1} \cdot \text{km}^{-1}$ at 1.5μm).
So, for the Raman scattering process, in case of a pulsed input, the interaction length L_{int} will be either the walk off length or the fibre length, whichever is smaller.

2.5 A Review of Optical Fibre Shape Sensors

2.5.1 Conventional Shape Sensors

Conventional shape sensors base their sensing technology on strain gauges, optoelectronics sensors and Micro-Electro-Mechanical System (MEMS).

A strain gauge is a device used to measure strain on an object. It consists of a metallic conductive pattern that is printed on a foil. The gauge is attached to the object and as it is being deformed, the foil is subsequently deformed and so its electrical resistance changes. The principle behind this lies in the dependence of the electrical conductance on the conductor's geometry. When an electrical conductor stretches (within the limits of its elasticity) it will become narrower and longer, which increases its electrical resistance end-to-end. Conversely, when a conductor is compressed such that it does not buckle, it will broaden and shorten, which decreases its electrical resistance end-to-end. From the measured electrical resistance of the strain gauge, the amount of induced strain may be inferred and subsequently it can be related to curvature. One example of such a strain gauge is reported in the work [41] where a skin attachable flexible sensor array is developed for respiratory monitoring in case of premature infants. The purpose of this sensor is to detect the beginning and end of the breathing cycle, through measuring the oscillating deformation between thorax and abdomen caused by breathing. In case of abnormality, the respiration device will be triggered. Another application of shape sensing based on strain gauges is GloveMAP. GloveMAP is a device consisted by a hand glove with strain gauges attached at its top surface. When a finger bends the length of the strain gauge changes and as a result its resistance. The resistance change is converted into a voltage output that is translated by an Arduino Microcontroller. The signal produced is analysed using an algorithm in order to translate the hand gestures into sign language [42].

Optoelectronics sensors used for shape sensing are based on a combination of optical electronic sensors as the name implies. An example of this technology is SensorTape. SensorTape is a flexible tape containing gyroscopes, tri-axial accelerometers as well as Time-of-Flight distance sensors which measure the time infrared light needs to bounce from an object. This device can be used as a shape-measuring tool in real-time as well as a wearable sensor for posture monitoring [43].

Another category of conventional shape sensors rely on MEMS technology. A MEMS device is comprised of a proof mass with "fingers" which is fixed on one end with a spring and that it is free to move left and right when a force is applied [44]. The movement of these "fingers" that are located between fixed electrodes, change the capacitance of the system and the acceleration can be measured. ShapeAccelArray is another example of MEMS sensors. It consists of a series of waterproof tubes each of them is equipped with tri-axial accelerometers and gyroscopes. This type of sensor is used for deformation monitoring of geotechnical structures such as borehole and pipes [44].

Although conventional sensors are low-cost and compatible with electronics, they have limitations due to their large size, complexity, since they require power supply and present a risk when used in hazardous and explosive areas owing to their sensitivity to EM interference. Lastly, they do not offer a truly distributed way of sensing. Below, a more promising category of sensors based on optical fibres is presented, with a brief overview of its principles, applications as well as advantages, compared to the conventional sensors.

2.6 Fibre Optic Shape Sensors

Optical fibre sensors convert measurands such as strain or temperature from the physical world, to an electronic signal, through the use of light. Their history dates back to the early 1970s when a low-loss glass optical waveguide was first fabricated [45]. Microbend optical fibre sensors were one of the earliest fibre optic sensors. The mechanical perturbation of a multi-mode fibre waveguide causes coupling of light between guided modes and radiation modes. The change in the light intensity of the bent fibre is measured by a photodetector and this signal can be used to detect original environmental perturbation such as pressure, temperature or acceleration [46], [47]. The idea of using multi-core fibres for bend sensing applications traces back to late 70s. Meltz and Snitzer were granted patents in 1981 for a fibre optic strain sensor that relies on the cross-talk phenomenon in a two-core fibre. As light energy propagates along one core in the optical fibre, changes in strain or in hydrostatic pressure cause a change in the relative energy that is cross-coupled between the cores [11]. These approaches did not offer the possibility of identifying the direction of the bend.

2.6.1 Discrete Shape Sensors

Shape sensing based on Fibre Bragg Gratings (FBGs)

The next improvement in the field of bend sensing comes from determining the direction of bend. To achieve this, an alternative way of sensing was used, in which the cores of a low cross-talk MCF have FBGs inscribed. FBGs are a periodic modulation of the refractive index in the core of an optical fibre. This modulation can be created through UV laser radiation resulting in a wavelength-specific dielectric mirror that reflects a very narrow band of light. The wavelength of the reflected light depends on the period of the refractive index variation [48]. FBGs offer a quasi-distributed way of shape sensing based on differential strain measurements in cores having the same axial location but an opposite position about a fibre's neutral axis. When a fibre is under bend, the strain induced in the fibre changes the period of refractive index modulation depending on the location of the grating with respect to the neutral plane (compression or tension). As a result the Bragg wavelength changes proportionately with this strain. By measuring the wavelength change, the differential strain can be extracted and the shape of the object can be determined

[49]. Gander's work, published in 2000, is the first report of a directional bend sensor based on Bragg gratings written in multicore fibres [50]. FBGs were written simultaneously in two-cores of a 4-core multicore fibre for one-axis bend measurements and the reported curvature resolution was 0.31m^{-1}. In 2003 the use of FBGs for two-axis curvature measurement in three separate cores of a 4-core multicore fibre [51] is reported for the first time, with a curvature error of 0.047m^{-1}. Three years later, distributed bend sensing was achieved thanks to a combination of FBGs and Wavelength Division Multiplexing (WDM) [52]. In this technique, each grating that is written to the fibre has its Bragg resonance at a different wavelength. Several interrogation techniques have been used for determining the Bragg wavelength such as Fabry-Perot filtres [53] or Mach-Zehnder interferometer [54]. In 2006, a fibre optic position and shape sensing device described in a patent filled in by Luna Innovations, based on a 3-core fibre with an array of FBGs inscribed into each core [14]. The disadvantage of shape sensing with WDM is the limitation with respect to the number of FBGs with different Bragg wavelength that can be written in a fibre something that restricts the length of the measurement.

2.6.2 Distributed shape sensing

An optical sensor that is able to determine the spatial distribution of one or more measurands at each and every point along a sensing fibre is called a distributed optical fibre sensor [32]. There are several distributed sensing techniques that can be used for shape sensing [55],[56]. Here we present a brief overview of the most commonly used techniques for shape sensing.

Shape sensing using OFDR

A simplified OFDR setup is shown in Fig. 2.9. A pulse from a linear chirped laser splits into the sensing arm and to the reference arm with the use of a coupler.

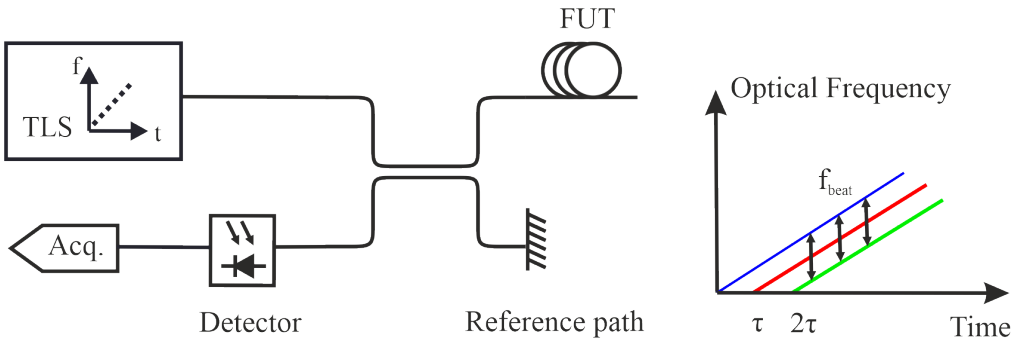

FIGURE 2.9: OFDR basic configuration. Light from a linearly tunable source travels down to the sensing and reference arm. The difference in the path lengths between the two arms results in a beat frequency that is characteristic of a specific location along the fibre.

The difference in the path length between the reference and the sensing arm results in a delay of the pulse travelling in the sensing arm [39]. As a result, the two waves

recombine at the detector with a beat frequency that is characteristic of the path length difference. The implementation of this principle to shape sensing will now be described in more detail.
The frequency of the source is linearly swept with time so we can write $f(t) = \gamma t + f_0$. Since the frequency and the phase are related as $f(t) = d\phi/dt$, the phase of the electromagnetic wave can be expressed as:

$$\phi(t) = \int_0^t f(t)dt = \int_0^t (\gamma t + f_0)dt \Rightarrow \phi(t) = \frac{1}{2}\gamma t^2 + f_0 t \tag{2.19}$$

where

- $f(t)$ is a linearly tuning frequency
- γ is the optical frequency tuning speed
- f_0 the initial optical frequency

The optical field at the reference arm can be written as [57], Fig. 2.10 a)

$$E_r(t) = E_0 \cos[2\pi\phi_r(t)] = E_0 \cos\left[2\pi\left(f_0 t + \frac{1}{2}\gamma t^2\right)\right] \tag{2.20}$$

where E_0 is the amplitude of the signal.
The backscattered light coming from a position z_i along the fibre can be represented as, Fig. 2.10 b),

$$E_s(t) = \sqrt{R(\tau_i)}E_r(t - \tau_i) \tag{2.21}$$

$$= \sqrt{R(\tau_i)}E_0 \cos\left[2\pi\left[f_0(t - \tau_i) + \frac{1}{2}\gamma(t - \tau_i)^2\right]\right] \tag{2.22}$$

where

$$\tau_i = \frac{2nz_i}{c} \tag{2.23}$$

τ_i is the time needed for the round trip from a location z_i along the fibre, $R(\tau_i)$ is the reflectivity of the fibre under test at the time delay τ_i, n is the refractive index in the fibre and c is the speed of light in vacuum.
The intensity of the beating signal reaching at the detector between a micro segment $\alpha\beta$ on the fibre and the reference signal is $I(t) = |E_r(t) + \sum_{i=a}^{b} E_{si}(t)|^2$. α, β are two positions along the length of the fibre.

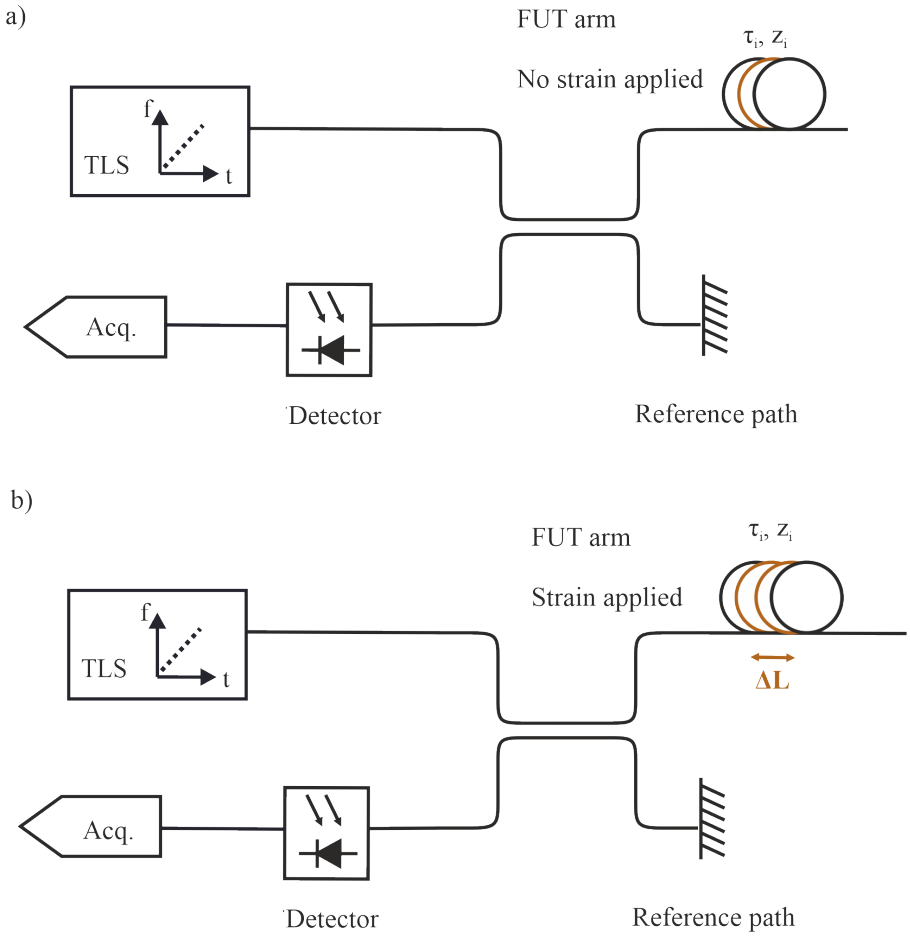

FIGURE 2.10: Simplified OFDR schematic in the case of a) an unstrained fibre b) strained fibre.

$$I_{\alpha\beta}(t) = \sum_{i=a}^{b} E_0^2 \sqrt{R(\tau_i)} \cos\left[2\pi\left(f_0\tau_i + \gamma\tau_i t - \frac{1}{2}\gamma\tau_i^2\right)\right] \tag{2.24}$$

where $f_{bi} = \gamma\tau_i$ is the beat frequency from the position with a time delay τ_i within the segment $\alpha\beta$. In Eq. (2.24) only the AC term is kept.
When the fibre is under strain the length of the segment changes from L to $L + \Delta L$. Then $I_{ab}(t)$ becomes,

$$I_{\text{stretch}}(t) = \sum_{i=a}^{b} E_0^2 \sqrt{R(\tau_i)} \cos\left[2\pi\left(f_0\tau_i + \gamma\tau_i t - \frac{1}{2}\gamma\tau_i^2 - \Delta\phi)\right)\right] \tag{2.25}$$

In other words the strain induces an extra term in the phase $\Delta\Phi = f\Delta L n/c$ which is proportional to the change in the length ΔL [57]. The central frequency is denoted with f.

A cross correlation between the spectrum (Intensity vs Distance) of a strained section of an optical fibre and the spectrum of the same section measured when

no strain applied is used to identify the shift in the strained spectrum [58]. So $\Delta\epsilon$ can be calculated from $\Delta\lambda$. More specifically, Rayleigh backscattering caused by the random refractive index fluctuations along the fibre can be modelled as long and weak FBGs with randomly varying period. The wavelength shift, $\Delta\lambda$ of the backscattered light due to a temperature or strain change can be expressed as [59],

$$\frac{\Delta\lambda}{\lambda} = K_\tau \Delta T + K_\epsilon \epsilon, \tag{2.26}$$

where K_τ, K_ϵ are the temperature and strain coefficient respectively.

Below, some of the literature work where OFDR technique is used for shape sensing purposes, is presented. In 2012 Luna Innovations demonstrated a fibre-optic sensing technology for over 30m of a tri-core twisted optical fibre with an accuracy between 0.4% and 1.3% by length [60]. The OFDR technique was used by Duncan et al in [61] in comparison with FBGs in order to detect the curvature. The results showed that the error in determining the diameter of the spool was about an order of magnitude smaller when using OFDR (0.3mm) compared to using FBGs (1.9mm). Various patents have also been filed describing the use of Rayleigh scattering in shape sensing [62], [63], [64]. In 2017, Westbrook et al. [65], [66] used continuous FBGs inscribed in helical multi-core fibres to enhance the Rayleigh scattering spectrum and demonstrated bend sensing applications.

Shape sensing based on BOTDA

In 1989, Horiguchi and Tadeda of NTT (Nippon Telegraph and Telephone) Laboratories used Brillouin Optical Time-Domain Analysis (BOTDA) to analyse attenuation characteristics in a fibre [67]. Although it was first introduced as an improvement to the Optical Time-Domain Reflectometry (OTDR) first developed in 1976 [68], it was further established in the distributed sensing field since it allows the measurement of the Brillouin frequency shift.

In this technique, two counter-propagating waves, a pulsed one (pump) and a continuous one (probe) are sent from the two ends of the sensing fibre. Their interference results in a high intensity of the electric field in the region of interaction which, due to electrostriction alters the refractive index of the core in a periodic manner leading to the creation of a density wave that moves in the same direction as the pump. The interference happens only for the length of the fibre where the frequency of the phonons match the Bragg condition that is the difference between the frequency of the pump and the probe match the BFS frequency, $f_{\text{pump}} - f_{\text{probe}} = 2n\upsilon_{\text{acoustic}}/\lambda_{\text{pump}}$. Due to the elasto-optic effect the acoustic wave acts as a moving grating leading to a power transfer from the pump to the probe resulting in a net gain for the latter and net loss for the former [69]. This process is schematically shown in Fig. 2.11.

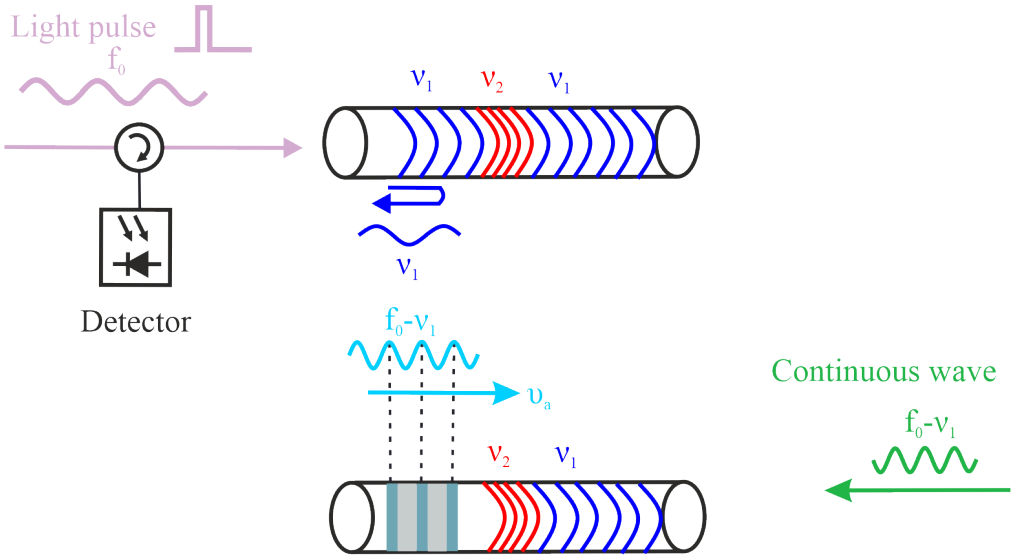

FIGURE 2.11: Principle of BOTDA. A pulse of light with frequency f_0 impinges upon the fibre. The interference between the incident light and the phonons with frequency ν_1 results in a high intensity electric field with frequency $f_0 - \nu_1$ in the region of the interaction. The refractive index of the material is altered locally in a periodic manner resulting in a periodic pattern in the density of the material that can be seen as a moving Bragg grating. The interference between the acoustic wave and a counter-propagating continuous wave leads to an even stronger grating which in turn results in an even stronger backscattering of the input pulse. This loop continues until the pump deplets completely.

By scanning the frequency of the continuous light wave, the Brillouin frequency shift and subsequently the strain distribution, are mapped along the length of the fibre and the 3D BGS is reconstructed as shown in the concept figure, Fig. 2.12.

The spatial resolution of BOTDA is limited to $\sim$ 1m due to the phonon lifetime [70], [69]. However, in order to increase the spatial resolution a combination of Differential Pulse Width Pairs (DPP)-BOTDA can be used. In this technique two Brillouin Gain Spectra (BGS), obtained from pulses shifted in time, are subtracted. The rising and falling time of the pulses define the spatial resolution [70]. Multi-core fibres (MCFs) have been recently investigated for distributed curvature sensing using a combination of DPP-BOTDA. Zhao et al. measured a range of curvatures between 10m^{-1} to 20m^{-1} using Brillouin optical time domain analysis (BOTDA), with an error of less than 8% over a 1km long 7-core fibre and with a spatial resolution of 20cm [71].

In 2017 a group from Poland, used BOTDA in combination with a multi-core microstructured fibre in order to investigate the effects of bending on the Brillouin Frequency Shift (BFS). In the research reported in [72], 26m of a 7-core fibre with air-hole isolation were coiled in a spool and it was shown that the frequency shift induced in one of the outer cores varied along the fibre while the frequency shift corresponding to the central core, remained constant [72]. Ba et al performed shape reconstruction experiments by gluing two optical fibres on both sides of three semicircles with

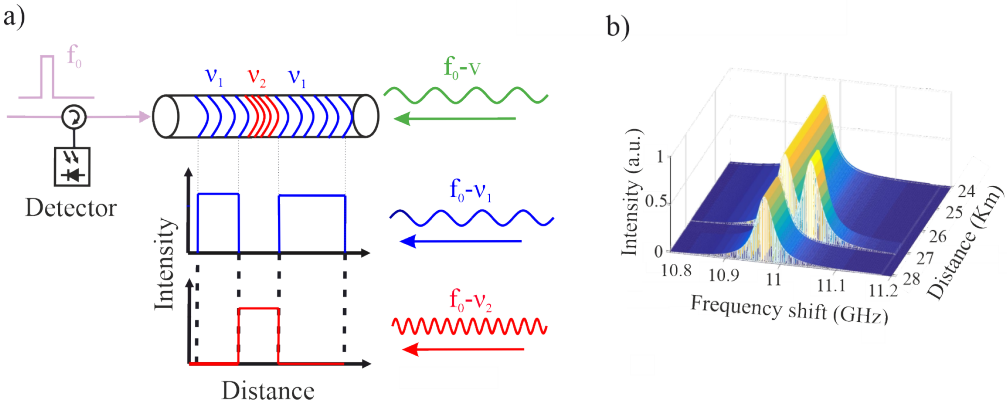

FIGURE 2.12: Schematic of BOTDA sensing process. a) The interference between the continuous wave light and the pulse happens only for the region of the fibre where the phase matching condition is met. b) As a result the strain in the fibre can be mapped along its length.

different bending radii (10cm, 7.5cm, 6.25cm) and by measuring the BFS, achieving a relative error of 5% for the entire curve [73].

Shape sensing using BOTDR

An alternative, single-ended technique based on Brillouin scattering was demonstrated in 1993 by a team also at NTT. This technique was Brillouin OTDR (BOTDR) [74] in which the wavelength and intensity of the spontaneous Brillouin backscattered signal are used to map the temperature and strain along the fibre. This is the technique that has been used in this study and a more analytical description will follow in Sec. 4.3.

2.7 Comparison of the techniques

Choosing the appropriate technology for a specific application requires to consider the spatial resolution, range, strain resolution, update time and cost needed [32]. There is not "one size fits all" technique regardless the application and so a careful judgement of all the above parameters should be made before making a selection.

Brillouin-based techniques based on spontaneous scattering offer a lower signal to noise ratio compared to the techniques based on stimulated scattering where the light is amplified [39]. That means that they require more averaging to compensate for the additional noise, rendering them more appropriate for static and quasi-static distributed temperature/strain measurements. Conversely, the access from both ends that offers the possibility for stimulated scattering in BOTDA techniques can be turned into a disadvantage when it comes to a fibre breakage. More specifically if the fibre breaks, all the measurements are lost, while in case of single-ended techniques, all the measurements that have been collected up to the point of the breakage can be acquired and analysed.

Brillouin based techniques generally have a spatial resolution in the range of 1m. This is due to two main limitations relating to the pulse width and the broadening of the BGS [75]. It is known that spatial resolution depends on the pulse width as [32],

$$\delta z = \frac{v_g}{2}\tau_p \tag{2.27}$$

where v_g is the speed of light within the fibre and τ_p is the pulse width. So it is safe to assume that the shorter the pulse width the higher the spatial resolution. However a decrease in the pulse width results in an exponential decrease of the power entering the sensing fibre [75]. One more important factor affecting the spatial resolution is the broadening of the BGS. The detected BGS is the convolution between the natural BGS which has a linewidth and the pulse spectrum [76]. The broader the detected BGS, the less accurate the determination of the central frequency becomes, affecting the frequency resolution.

The Brillouin spectrum is accurately approximated by a Lorentzian function with a resonance frequency of f_B and a Full Width Half Maximum (FWHM) of Δf_B that is related to the phonon lifetime Γ as [77],

$$\Delta f_B = \frac{1}{\pi\Gamma} \tag{2.28}$$

Since the phonon lifetime is $\sim$ 10ns the linewidth of the BGS is reported to be $\sim$ 33MHz for silica fibre [78].

Linewidth and signal-to-noise-ratio considerations determine the minimum detectable change in f_B

$$\delta f_B = \frac{\Delta f_B}{\sqrt{2}(SNR)^{1/4}}, \tag{2.29}$$

where SNR is the electrical signal-to-noise power ratio. This in turn has an effect in the strain resolution. Taking into account that the strain resolution is given by [79]

$$\delta\epsilon = \frac{\delta f_B}{f_B C}, \tag{2.30}$$

where f_B is the central Brillouin frequency and C is the strain coefficient, then the strain resolution is mainly defined by the frequency resolution and could come down to the range of a few tens of microstrain if the frequency resolution is a few MHz. By improving the SNR the frequency resolution can be further improved however there is still a limit due to the unavoidable broadening of the measured BGS.

Brillouin-based DOFS use the frequency and intensity variations of the Brillouin backscattered light to measure the absolute temperature and strain of the fibre. The Brillouin frequency shift (BFS) is linearly dependent to the temperature and axial strain exerted on a fibre [79]. As a result with the Brillouin based techniques the absolute strain or temperature can be measured. This is not possible with the Rayleigh based techniques that rely on the relative motion of the inhomogeneities in a fibre.

Rayleigh scattering occurs due to randomly distributed density fluctuations that are frozen into the fibre during the cooling process as it has already been described in section 2.4.1.

The sensing principle of the Rayleigh-based optical fibre sensors depends almost entirely on these inhomogeneities and their relative movements. Any fluctuation in the position of these inhomogeneities due to variations in temperature and strain of the fibre affects the phase, intensity and polarization of the Rayleigh scattered light in the fibre [39].

This relevant motion implies that an acquisition of a reference spectrum is always needed at the start of the process to extract the influence of the strain/temperature on the fibre. However it is worth noting that the application of strain in the fibre not only shifts the position of the inhomogeneities but also redistributes them. Since the cross-correlation method requires the data to be relatively uniform, the OFDR technique is limited to a very small strain range between 0.1 and a few $\mu\epsilon$ for which the OFDR traces remain relatively uniform [39]. It should be noted that although a reference coil is needed for the determination of the absolute strain in a BOTDR system, in the case of shape sensing where it is only the differential strain between the cores that is needed, such reference is not necessary. On the contrary, in the case of the OFDR technique, a reference measurement of all the cores is required in the beginning of the experiment.

FBGs are a quasi-distributed alternative that provide a mm resolution. So when localised measurements are of interest, at selected positions along the fibre length and at a reasonable cost, those sensors are proven to be very good candidates.

2.8 Applications of optical fibre shape sensing

There are many applications of the emerging field of shape sensing, ranging from medical robotics and aerospace, to the mining industry and structural health monitoring to name just a few. The reader can be referred to a plethora of review articles overviewing the applications of shape sensing [80–87]. This section aims to only give a taste of the range of applications that shape sensing can find use and inspire further reading.

The Da Vinci surgical system, made by Intuitive Surgical (USA) [88], is the only commercially available tele-operated surgical system. Its equipment structure is based on a master-slave system with three functional units, the operator console

(master system), the vision cart (control system) and the patient cart (slave system) Fig. 2.13. The surgeon sits as the operator control outside the operative field and through enhanced, magnified 3D images he controls the fibre optic guided instruments that are located in the patient cart (slave system) using master hand controls and foot pedals. The vision cart processes information to and from the control and patient carts.

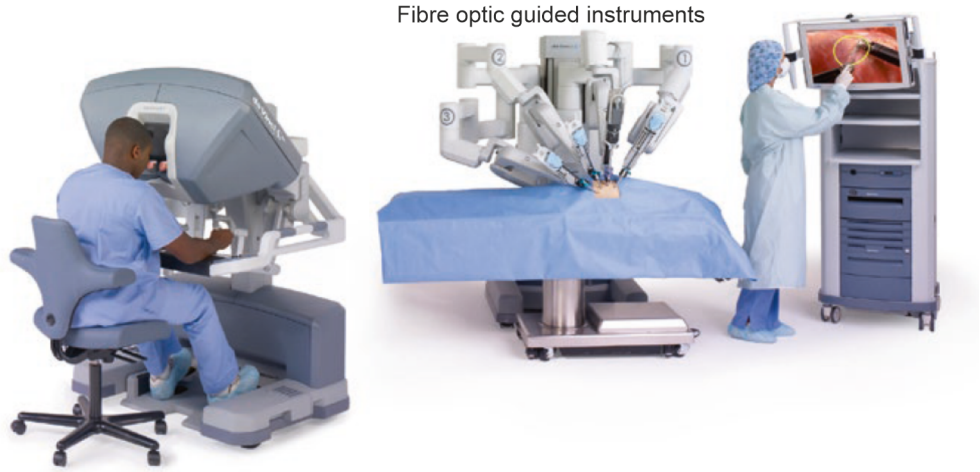

FIGURE 2.13: The three functional units of the Da Vinci robotic system: operator console (master system), vision cart (control system) and patient cart (slave system). Source [88].

The determination of the shape of a structure is based on the measurement of the shape of the optical fibres that are in contact with the articulating segments of the robotic device [89]. By knowing the shape of these optical fibres the curvature and the relative position of the instrument to which the optical fibre is associated can be determined.

In urban environments it is common to construct new tunnels close to already existing underground structures. Usually the ground movements due to the construction of a new tunnel lead to an ovalisation of the structure that is in close proximity to the newly constructed one, Fig. 2.14 a).

In the work reported by Gue et al. [90] fibre optic cables were attached to the linings (walls) of the existing cast iron Royal Mail tunnel as seen in Fig 2.14 b), c and distributed fibre optic train sensing was performed using BOTDR. As a result, a continuous strain profile was measured during the construction of Crossrail's platform tunnel less than 2m directly below it. In this way engineers can be informed about the health of the structure, preventing potential damage and catastrophic accidents.

The Industrial Centre for Geological Disposal, or Cigeo, is a deep geological disposal facility for radioactive waste to be built in France. It will serve for disposal of highly radioactive long-lived waste produced by France's current fleet of nuclear facilities, until they are dismantled, as well as from reprocessing of spent fuel from nuclear power plants.

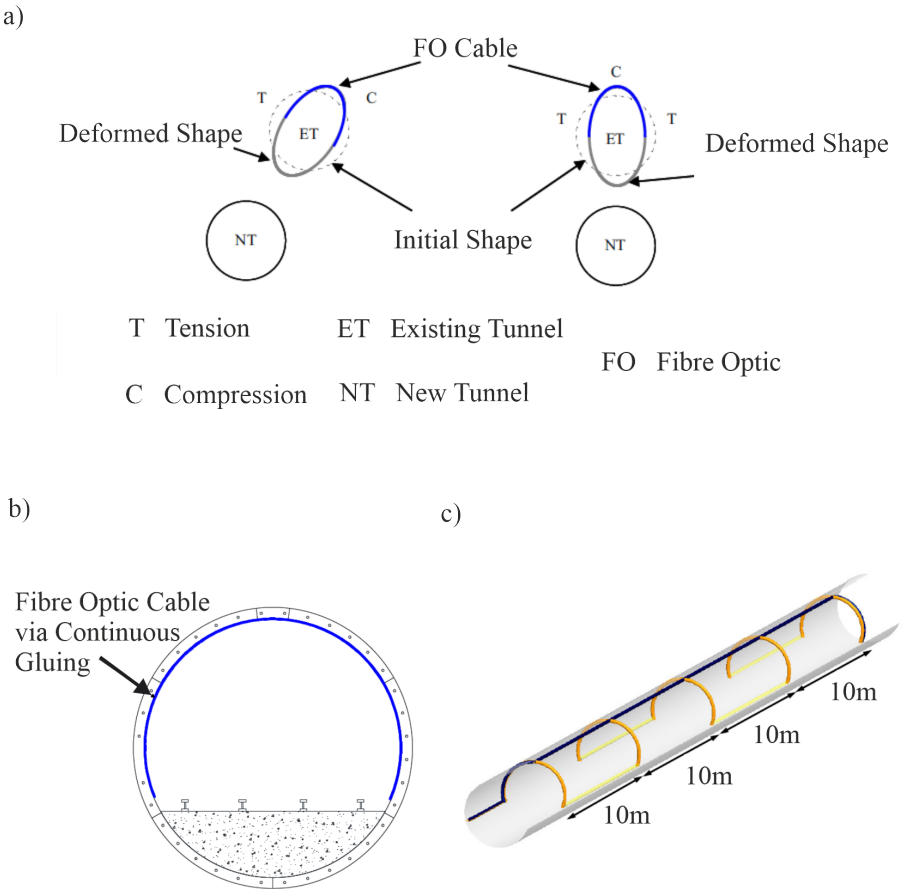

FIGURE 2.14: a) Visualisation of the tunnel deformation from fibre optic strain data b) Cross sectional fibre optic cable attachment via continuous gluing c) Fibre optic cable instrumentation layout at Royal Mail tunnel. Figure taken by 2.14.

Monitoring the convergence of a tunnel is vital when the structural health must be secured in order to ensure safety of the radioactive waste repository cells. Convergence, refers to the deformation of the circular cross sectional area of the void of a tunnel, due to the stress redistribution happening during an excavation. Recently Piccolo et al. [91] used BOTDA technique to monitor strain in a metal ring, that served as a mock-up of the Cigeo's underground radioactive waste repository Fig. 2.15.

Finally a finite element method was used to calculate convergence from strain data achieving 1mm resolution in its determination.

One of the most promising and impressive applications of fibre optic sensing technology is in the field of aerospace. As the curiosity rover is currently exploring Mars, future missions will require greater mobility and the ability to navigate through challenging terrains for in situ measurements and physical sample collection. Tethers to a stationary base provide power, decreasing the need for on board electronics. They can also be used to support the rover as it navigates steep slopes, to pull it out of loose soil or to guide it back to the base station. If the tether gets damaged the rover may lose power and communication with the base station,

FIGURE 2.15: Left: Metallic ring used in the laboratory as a mock-up of the underground cell. Right: Details of the sensors employment where the cable is fixed on the metallic ring either by [1] soldering or [2] gluing. Source [91].

limiting its lifespan to its last charge forcing to end its mission ahead of time. Knowledge of the tension, the curvature and the shape all along the length of the tether in a distributed way can help identifying cliff edges, twist, turns and sharp rocks minimising the risk of a potential damage of the rover during its expedition.

Luna and Nasa's Jet Propulsion Laboratory [92] have developed and tested in the field a prototype tether containing a specialty multicore fibre. In combination with the use of OFDR technology they demonstrated high resolution ($1.6\mu\epsilon$ and better than 50μm spatial resolution). The mechanics of this tether can be seen in the top image of Fig. 2.16, where it is shown that the MCF is located at the central axis of the cable. The rover was tested at Mars Yard which is a simulated Martian landscape with soiled and rock characteristics matched to some regions of Mars. As the rover descends a steep slope, Luna's sensing tether shows several points of interest, see bottom Fig 2.16. Point (A) is the point where the tether is clamped to an anchor point. The curvature shows a tight bend and the tension shows a sharp increase. At location (B) the tether is snagged on a rock. A local curvature event marks the bend at this location, and a rapidly changing tension feature shows that the tether is wedged tightly. Finally a small curvature feature marks the point where the tether enters Axel's boom arm at point (C). The elevated curvature for the distal end of the tether's length shows where the bulk of the tether is spooled around Axel's central hub.

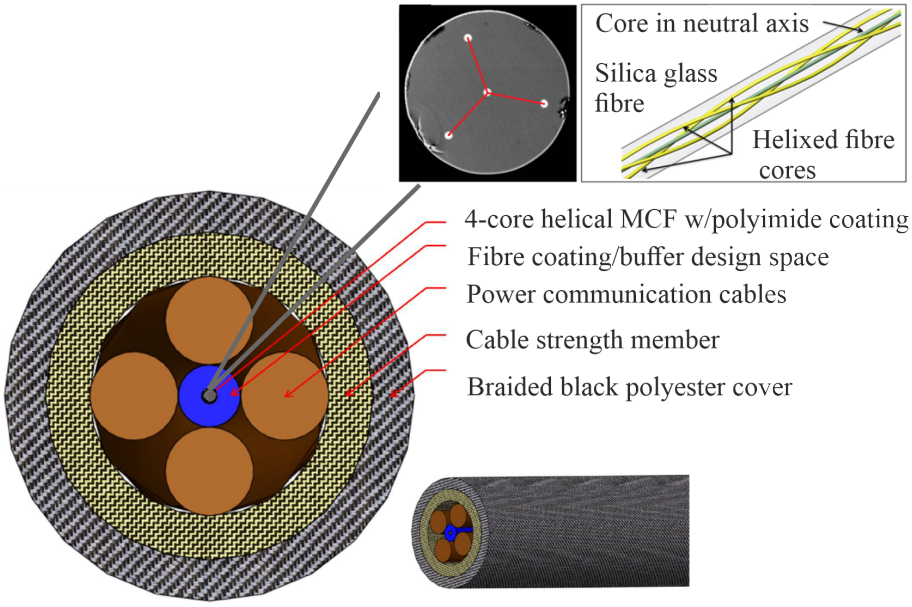

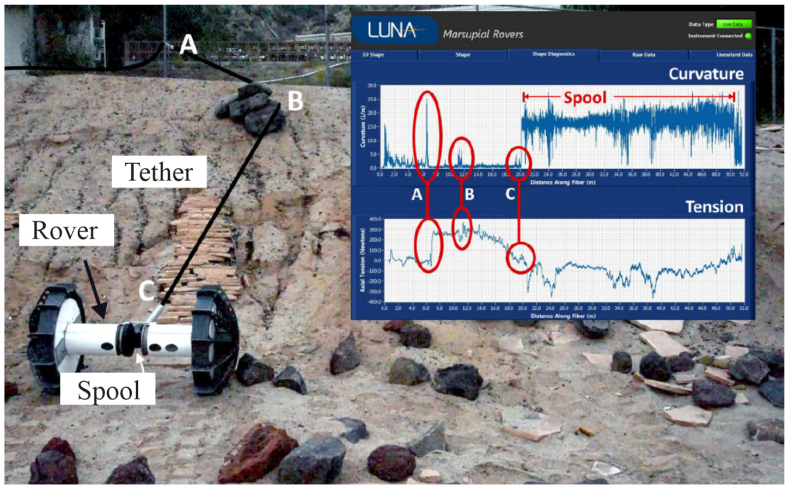

FIGURE 2.16: TOP: Tether's mechanical design. Luna's customized spun sensing multicore fibre is located at the cable's central axis. The four copper cables surrounding the sensing fibre serve for providing power and communication signal to the Axel-rover. BOTTOM: Demonstration of identification capability of several features as the rover descends a steep slope, such as the tether anchor point (A), a rock snag (B) and the cable's entrance into the rover's arm (C) by a combination of tension and curvature measurement. Figures adapted by [92].

2.9 Summary

This chapter provided a brief overview of optical fibres and their relation to distributed sensing. Two methods for fabricating spatial de/multiplexers for multicore fibres were described and the physical principles of Rayleigh, Brillouin, and Raman scattering were introduced. The basic shape sensing techniques were explained and a comparison was attempted. Brillouin-based techniques have a lower spatial resolution compared to those based on Rayleigh scattering although they

offer the advantage of measuring the absolute strain/temperature. FBGs are quasi-distributed but cost-effective alternatives. Each sensing technique has a trade-off and the choice depends on the application. Various fields of the shape sensing technology are presented in the last section.

In the next chapter the fabrication process of two novel multi-core fibres customised for curvature sensing is introduced.

Chapter 3

Multi-Core Fibre Fabrication

3.1 Introduction

Multi-Core (MC) preforms require a number of standard Single-Mode (SM) cores to be arranged in a single cladding-preform. This requires core rods, which are essentially thin SM preforms and a method to arrange them inside the cladding in order to form the required geometry.

There are a few techniques that can be used to create a multi-core fibre preform:

- Drilling holes in a large silica rod, inserting the core rods then heating until a solid rod is formed. This process is called collapsing.
- Using a Sol-Gel [93] or slurry technique [94] and a mold to make the host large silica rod. Then inserting the core rods, heating and collapsing.
- Stack and draw technique [95]. In this process SM fibre preform and spacing rods are stacked inside a high quality quartz glass tube. Then this stacked preform is heated, collapsed and drawn into a fibre.
- Sand Cladding technique which is a proprietary cladding technology used by Nextrom. In this process, the gap between the core rods and the thin wall outer tube is filled with silica granulates and then treated and sintered to clear glass.

In this chapter the fabrication process of a multi-core fibre will be described in detail. The structural unit of a MC preform is the SM core and its fabrication using the Modified Chemical Vapour Deposition (MCVD) method is presented in section 3.1.1. Next, the method the MC preform is assembled and drawn is described in 3.1.2 and 3.1.3 respectively. After the description of standard MC preform fabrication, the process for fabricating D-shaped and flat fibre are presented in sections 3.2 and 3.4.

3.1.1 Fabrication of Single Mode fibre preform

Fibercore uses Modified Chemical Vapour Deposition (MCVD) for the fabrication of the fibre preforms. The MCVD process is based on the high temperature oxidation of reagents inside a rotating tube which is heated by an external heat source [96].

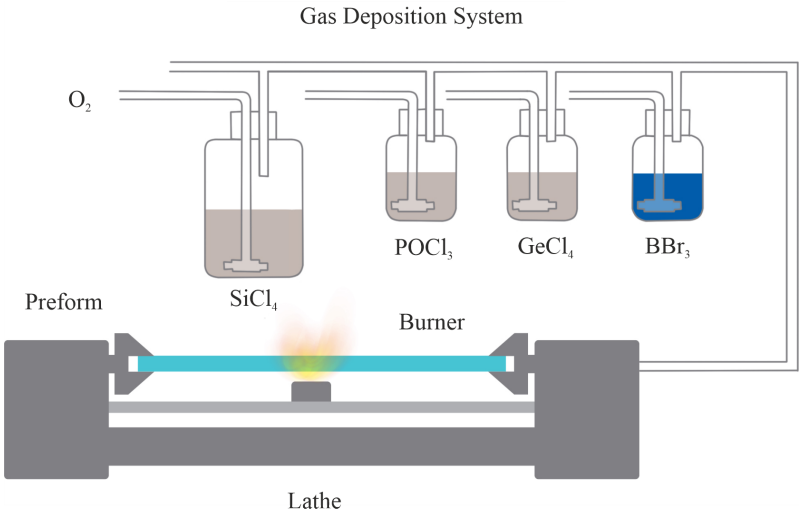

FIGURE 3.1: Schematic of the MCVD process. Different halide compounds can be used depending on the desired dopants and properties of the fibres. With the pass of carrier gas, such as O_2, the reagents are delivered in the glass working lathe through a pipe. The burner provides the heat required to initiate the reaction.

Chemistry The halides have high vapour pressure in room temperature which means that they can be easily evaporated once the temperature is just above ambient [97]. Each halide compound is kept in liquid phase inside a glass bubbler where the temperature is 25°. With the pass of a carrier gas, (N_2 or O_2) depending on the halide compound), those reagents are delivered in controlled amounts to the glass working lathe through a pipe. The flow rate of the halides is controlled by Mass Flow Controllers (MFC) that adjust the mass of the carrier gas according to the deposition. The compounds we can use are $SiCl_4, POCl_3, GeCl_4, BBr_3$.

Tubing Setup In the glass working lathe, the process starts by joining the deposition tube, which is a low water, high purity glass from Heraeus, with two lower-cost glass tubes that are called start-up and extract tube. The glass setup consists of the start-up and extract tube mounted on the chucks and the deposition tube welded in the middle. The start-up tube serves for the transfer of the gases inside the deposition tube without wasting a longer length of expensive glass. The extract tube has a double role: on the one hand it leads all the unreacted chemicals towards the extract system that ends to the scrubber; on the other hand, it helps maintaining the pressure inside the deposition tube slightly above the atmospheric. This is achieved by supplying a flow of gas into the tube to oppose the flow of gas coming from the deposition tube.

Deposition The deposition of standard Ge/Si core material was done using the MCVD process described above, but with the core scaled up such that instead of being SM when drawn to 125μm, it is SM when stretched, put into the MC preform and drawn to 125μm, Fig. 3.2. This means that it has to have a much larger

core-size than a standard SMF to give it the correct properties (NA, MFD, cut-off wavelength) when in a MCF, Fig. 3.2. The basic design parameters of the multi-core fibre are described in sections 2.2, 2.3.

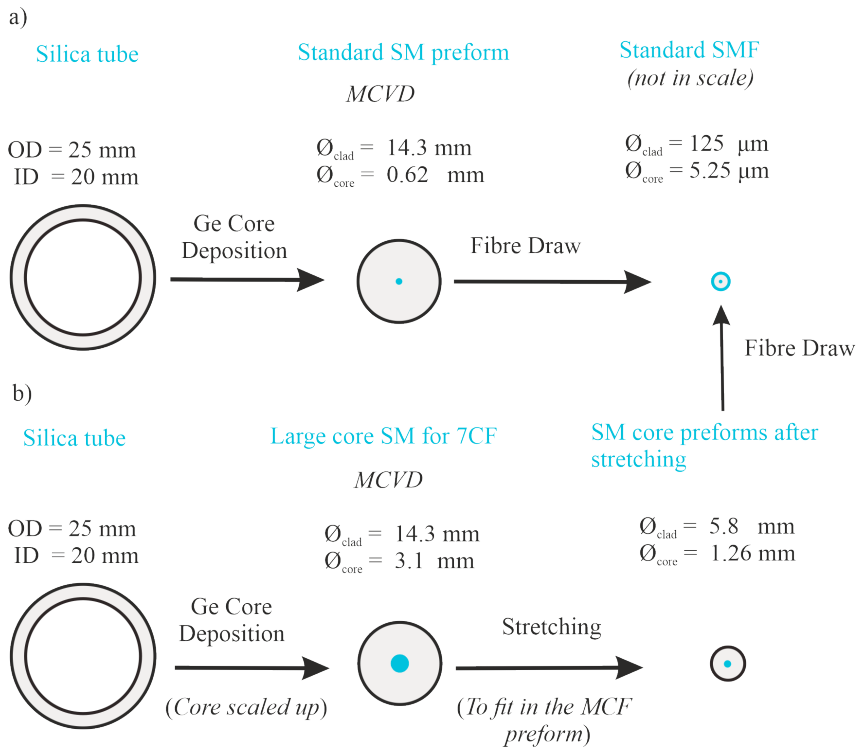

FIGURE 3.2: Schematic of the stages used during the fabrication process of a) a standard SM preform and of b) a SM preform used for the assembly of a MC preform. In the latter case, the Ge deposition intends to a larger core, so as for every core of the MCF to support SM transmission when the MC preform is drawn in a 125μm fibre.

3.1.2 Creation of a MC preform

The fabrication process of the MC preform started with the SM preform fabrication that has been described in the previous section, Fig. 3.2. The SM preforms were then stretched in order to be inserted into the cladding preform, Fig. 3.9. Stretching the preform allows it to be elongated, reducing the diameter according to the conservation of mass, whilst maintaining an identical core to clad ratio.

The cladding preform is 30mm in diameter with 5.8mm diameter holes and it was made by KOHUKU using the slurry casting method, Fig. 3.9. In this technique the starting point is silica powder that is ground with distilled water and an organic binder until the mix becomes a slurry. Then a polymerisation initiator is added and the slurry is transferred into a metal mold. Metal rods are placed to form the holes of the preform. After the polymerisation is done the organic binder has solidified and the metal rods are removed. The preform is cleaned, dried and sintered to obtain a clear glass finish [94].

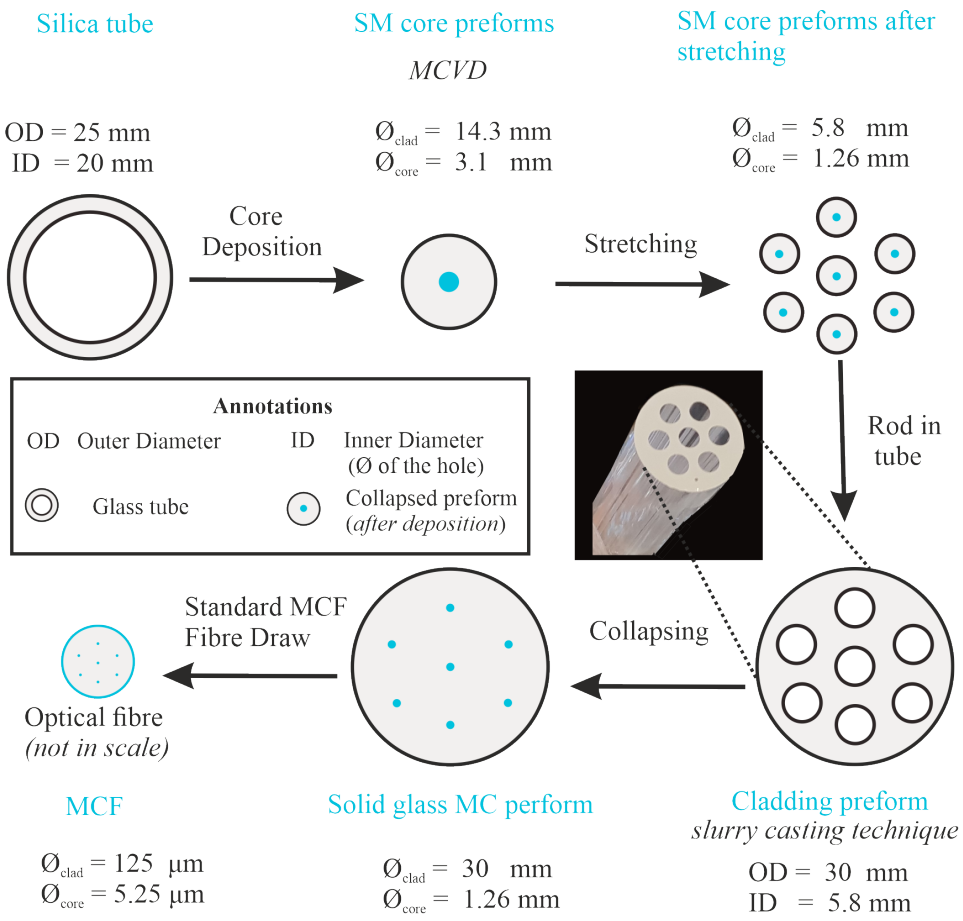

FIGURE 3.3: Schematic process of the MCF fabrication process. The SM preforms are first created and then inserted into the cladding preform's holes. The assembly is heated and sealed up until a solid glass preform is formed. The MC preform is then drawn into a fibre.

The fabricated cores were inserted into the holes and the assembly was then formed into a solid rod. This was achieved by heating the glass until it softens, and surface tension collapses the hole around the rods. This process is called collapsing and it is accelerated by creating a pressure lower than the atmospheric in the holes using a vacuum system, which also aids in reducing the likelihood of trapped gas causing bubbles in the final preform.

3.1.3 Drawing of MCF

The drawing of MC fibres follows the standard drawing process, since the preform that has been formed into a solid rod, reacts no differently to a standard single core preform. For the draw the preform is being fed in a graphite resistance furnace. This type of furnace requires an inert atmosphere to prevent the oxidation of the graphite element [33]. That is secured by having a flow of Ar inside the furnace that displaces the oxygen.

As the preform is fed in the furnace, its end is heated until it softens enough for the glass to deform. This creates a neck-down region which results in a reduction of the diameter that should be small enough to go through the coating applicators.

Circular dies 270μm in size are used for a 245μm coating. The fibre diameter is measured by a laser micrometer which consists of a laser beam and a receiver. As the laser beam scans the measuring area, it gets shadowed by the fibre that is placed in the direction of the beam. By measuring the shadow time, the fibre diameter can be calculated.

Once the fibre has been threaded through the coating applicators, it is then put through a capstan – which controls the draw speed of the fibre. At this start-up of the process, a certain amount of fibre is lost while the fibre is gradually being reduced in diameter.

As soon as the desired diameter is reached, the coating is applied, usually at a low speed. Normally two layers of coating are applied (a soft primary and a hard outer coating) but it can be a single layer coating too. The soft primary acts as a buffer between the hard outer layer and the fibre - so less stress is transferred through. The main advantage of using two coatings is that it makes it easier to strip the coating away. After the coating application is applied, the draw speed is increased to the required level.

After that, the fibre goes through the laser micrometer before reaching to the bottom of the tower. At that point the filament goes into the capstan which provides the drawing force and it is finally wrapped to a drum that can support up to 35Km-40Km of standard fibre. The uniformity of the fibre diameter depends on the control of the preform feed rate, the preform temperature, and the pulling tension. The equations that describe the drawing process are based on the conservation of mass stating that the volume of the preform before the drawing should be equal to the volume of the fibre after the draw [98]:

$$V_{\text{preform}} = V_{\text{fibre}} \tag{3.1}$$

$$l_{\text{preform}}\pi\frac{d^2_{\text{preform}}}{4} = l_{\text{fibre}}\pi\frac{d^2_{\text{fibre}}}{4} \tag{3.2}$$

$$\upsilon_{\text{feed}}\, d^2_{\text{preform}} = \upsilon_{\text{draw}}\, d^2_{\text{fibre}} \tag{3.3}$$

where V_{preform}, V_{fibre} is the volume of the preform and the fibre respectively, l_{preform}, l_{fibre} is the length of the preform and fibre respectively, d_{preform}, d_{fibre} is the diameter of the preform and fibre respectively, υ_{feed}, υ_{draw} is the feed and draw speed respectively. The feed speed is the speed at which the preform is fed into the top part of the furnace and draw speed is the speed at which the fibre is exiting the bottom of the furnace.

3.2 D-shaped preform fabrication

The fabrication of the D-shaped fibre starts by manufacturing the MC preform in the way it was described in Sec. 3.1.1, 3.1.2. The MC solid glass preform was then stretched to increase its length, since a certain amount of the preform is lost in

the start-up process of the fibre draw. As a final step of the preform fabrication, the 18 mm diameter preform, was mounted on a milling bed and a diamond milling tool was used to mill one of its side by 1.6 mm. The amount of preform to be milled was an estimate based on the the fact that the preferential bend is down to the degree of asymmetry in the fibre. If the aforementioned amount resulted in insufficient bending preference of the fibre, further iteration in the fibre design would be considered and another attempt would be made.

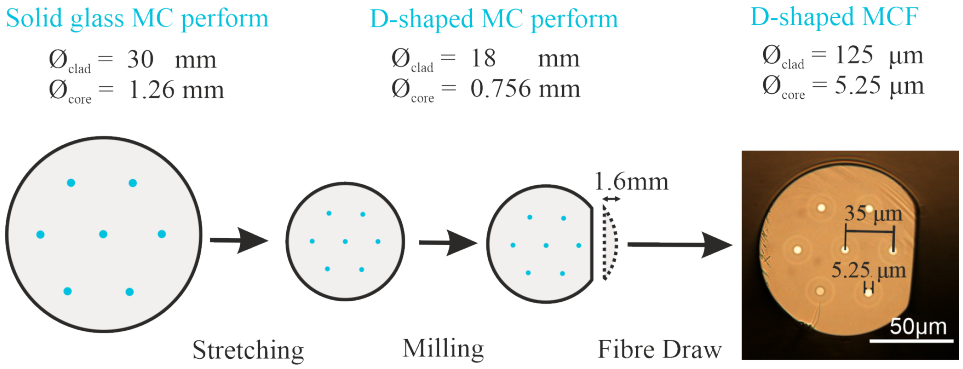

FIGURE 3.4: Drawing of the fabrication stages of a D-shaped MCF. The solid glass MC preform is first formed and then stretched, to increase the total length of the preform prior to drawing. In this way the yield of the process increases. One side of the cladding is subsequently milled lengthwise to create the D-shaped geometry and the fibre is then drawn to the desired dimensions.

Two options were investigated for the milling direction of this preform and they are depicted in Fig. 3.5. Each one has its own advantages and disadvantages. The first milling option offers the advantage of an increased sensitivity since two of the cores $(5, 3)$ have the maximum possible distance from the bending plane. However there is a risk of not being able to use the core close to the milled side, due to high mode leakage in case of excessive milling. Option 2 offers the margin for more milling before affecting the cores, hence enhancing the preferential bend of the fibre. However the expected sensitivity is lower compared to option 1 since cores 1 (or 2) and 6 (or 7) do not have the maximum distance from the bending plane.

Option 1 was finally preferred for the D-shaped fibre since it offers the option of increased sensitivity and the amount of milling can be controlled in a way so as not to cause mode leakage. This fibre can be installed on the medium of interest by gluing it along the structure. For the purpose of the curvature tests described in the next sections, the fibre was wrapped around spools of various diameters using a rewinding machine.

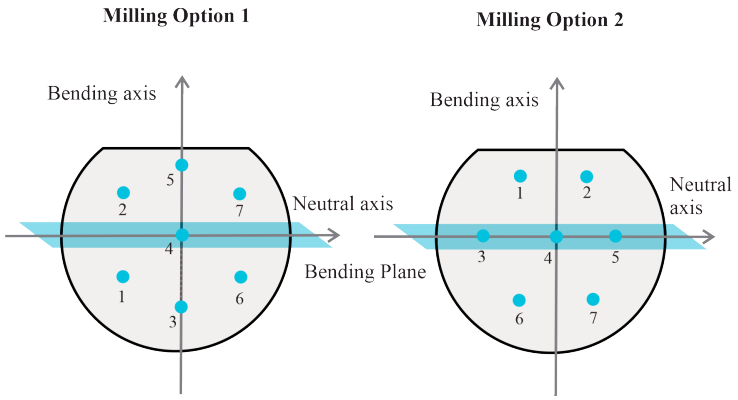

FIGURE 3.5: Schematic of the two possible directions for milling with respect to the fibre cores. The first milling option offers the advantage of an increased sensitivity since two of the cores (5,6) have the maximum possible distance from the bending plane.

3.3 D-shaped fibre draw

In order to maintain the D-shape, a temperature of 1900°C, 100°C lower than the standard drawing temperature was used. The fibre was drawn with a tension of 160 g at a speed of 60 m/min. For the draw of the D-shaped fibre the standard pressurized-coating system was used along with circular dies. Dual coating was also applied with the thickness of the primary being 185μm and the thickness of the secondary 245μm. The layout of the drawing tower used for the fabrication of the D-shaped fibre can be seen in Fig. 3.6.

It is important to note that the draw of this fibre geometry presents a significant challenge compared to the standard MCF. As the fibre is pulled, it is crucial for the D-shaped side to always maintain the same orientation along the length of the fibre. The preferential bending of the fibre means that as the fibre is bent round the capstan at the base of the drawing tower it will stay in the same orientation. If the fibre was inadvertently twisted during the start up (when the end is dropping down) this twist will be preserved throughout the draw. As the twisted part of the fibre enters the capstan it rotates the fibre above, imparting another twist on the fibre in the furnace. This process then repeats once that part of the fibre reaches the capstan. If there is a built-in twist in the fibre along a certain length while shape sensing is attempted, a said core may appear under compression while it is actually under tension rendering ambiguous the determination of the bending direction.

Due to the height of the tower and it being on multiple floors, it was not possible to stop the fibre from twisting during the start up process. All efforts were made to minimise the twist making it a significant improvement over the standard circular multi-core fibre, which has constant random twists during drawing.

Fig. 3.4 shows the geometry of the multi-core fibre that was created. The fibre has a pitch of 35 μm and a core diameter of 5.25 μm.

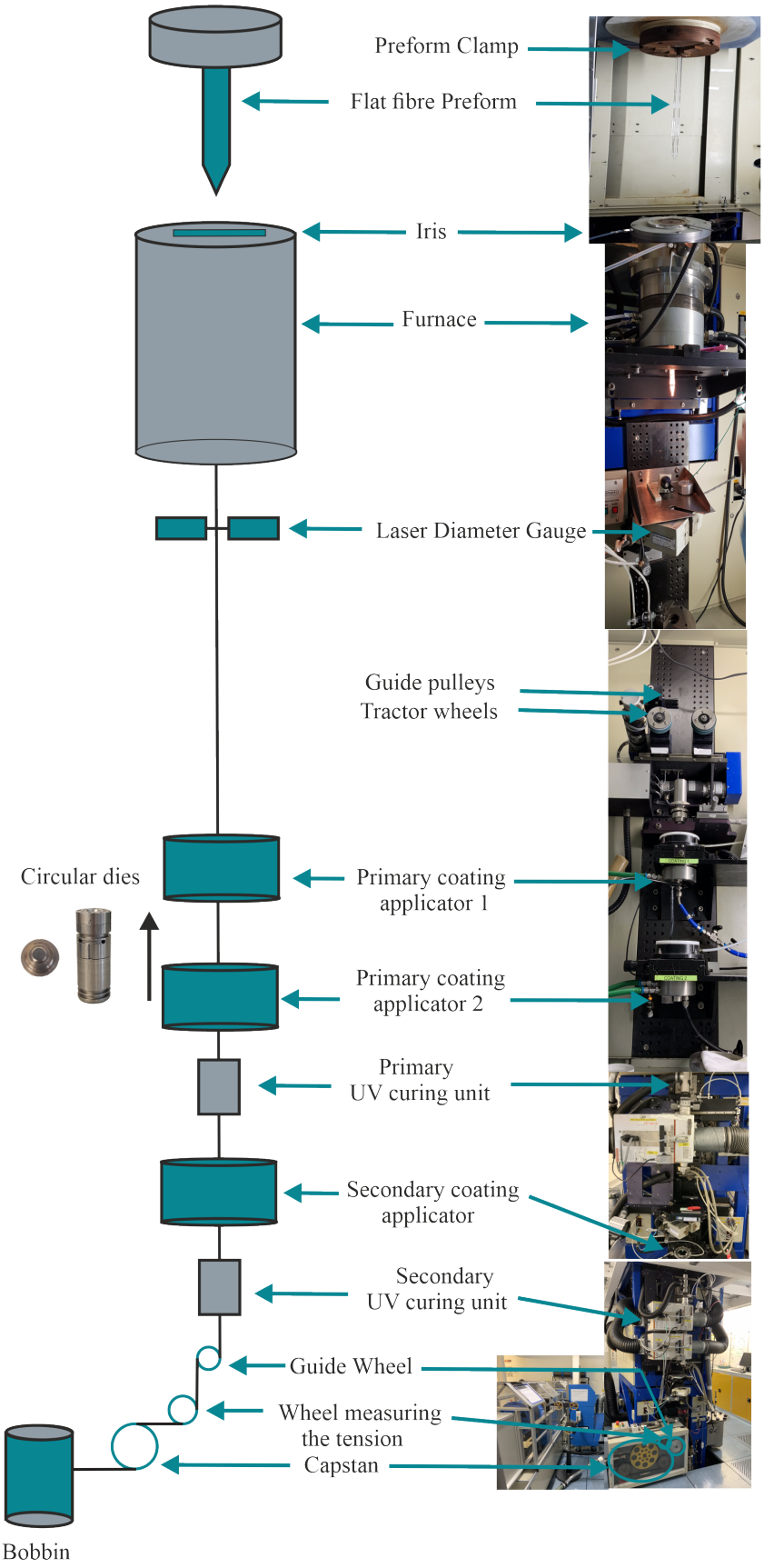

FIGURE 3.6: Schematic of the drawing tower configuration used for the D-shaped fibre fabrication. Circular dies and a pressurized coating system have been used for this type of draw.

3.4 Flat fibre fabrication

As with the D-shaped fibre, the fabrication of the flat fibre starts with the MC preform assembly. The solid MCF preform is then stretched to a 3:1 ratio, inserted into a sleeving tube and then the sleeved before the milling. The fabrication stages of the flat fibre preform are depicted in Fig. 3.7 and they will be described in detail in the next sections.

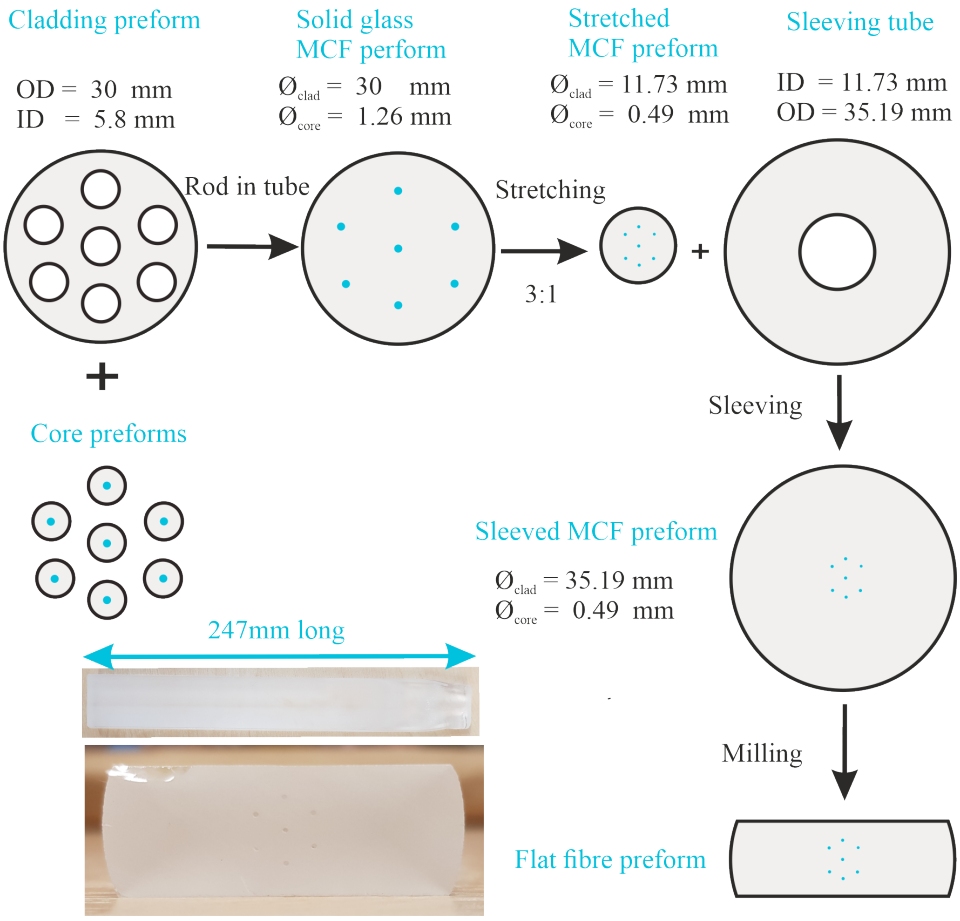

FIGURE 3.7: a) Core preforms that were fabricated using MCVD were inserted in the cladding preform fabricated by the slurry casting method. The 7CF preform that was produced after the sealing process was then stretched to a 3:1 ratio in order to fit into the sleeving tube. After sealing, the sleeved MCF was milled to the desired size.

3.4.1 Stretching

First the tip of the preform was heated to become smooth and lump-free, Fig. 3.8 (a). A rod handle was subsequently joined to the other end and the burner was passed a few times to smooth the diameter. This step is important as anything non uniform will be accentuated during the stretch. Once the diameter reached a value of around 17mm the stretching was paused the preform was separated from one of the handles, Fig. 3.8 (d) and that tip was joined to a glass handle of a smaller diameter. Ideally, it

is desired for the diameters of the handle rods to match the diameter of the preform at every stage of the stretching.

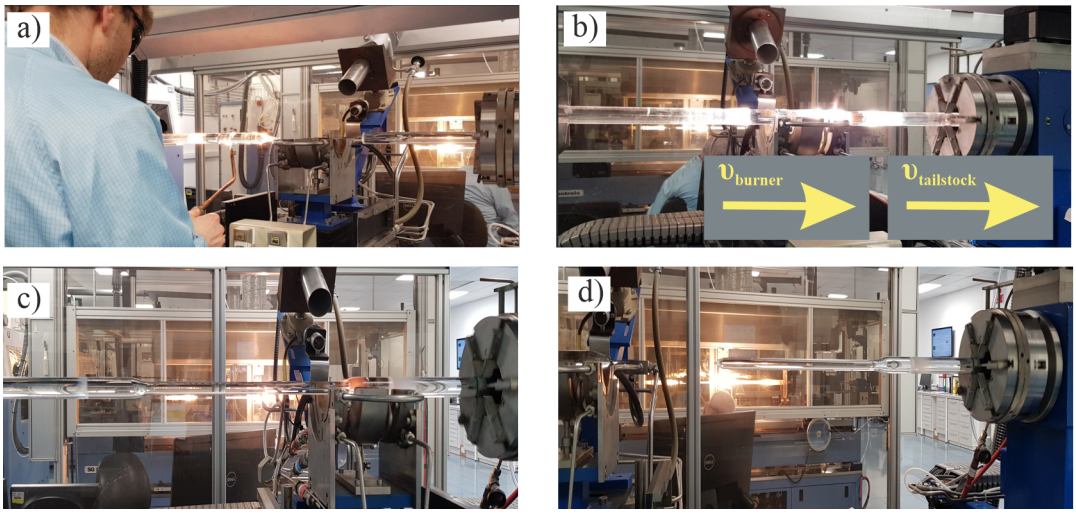

FIGURE 3.8: Stretching stages: a) The tip of the 7CF preform is heated in order to make it lump-free. b) The preform is stretched. c) Thinning of the preform due to stretch. d) Separation of the handle rod from the 7CF preform in order to later join a handle rod of a matching diameter.

In the next stage the preform had to be stretched to a 3:1 ratio in order to be sleeved subsequently. In order to achieve the 3:1 ratio, the 30mm 7CF preform had to be stretched to a diameter of 11.73mm. In order to perform the stretch Fig. 3.8 (b), (c), the final position of the tailstock was specified and its speed as well as the speed and the flow of the burner were controlled. Typical values for the speed is 50mm/min and burner flow of $40-60$ lpm H_2 with a $2:1$ ratio to O_2 respectively. It is noted that the speed and the burner flow were kept constant during a single stretch pass. They were only altered for each new pass, in order to maintain the same temperature and achieve the required end diameter.

The equations that govern the stretching process follow the mass conservation,

$$V_{\text{before stretching}} = V_{\text{after stretching}} \tag{3.4}$$

$$l_{\text{before stretching}}\, \pi\, \frac{d^2_{\text{before stretching}}}{4} = l_{\text{after stretch}}\, \pi\, \frac{d^2_{\text{after stretching}}}{4} \tag{3.5}$$

$$v_{\text{feed}}\, d^2_{\text{preform}} = v_{\text{pull}}\, d^2_{\text{fibre}} \tag{3.6}$$

$$(v_{\text{burner}} - v_{\text{tailstock}})\; d^2_{\text{before stretching}} = v_{\text{tailstock}}\, d^2_{\text{after stretching}} \tag{3.7}$$

where $V_{\text{before stretching}}$, $V_{\text{after stretching}}$ is the volume of the glass before and after stretching respectively, $l_{\text{before stretching}}$, $l_{\text{after stretching}}$ is the length of the preform before and after stretching respectively, $d_{\text{before stretching}}$, $d_{\text{after stretching}}$ is the diameter of the preform before and after stretching respectively, $v_{\text{tailstock}}$, v_{burner} is the speed of tailstock and burner respectively, v_{feed}, v_{pull} is the feed and pull speed respectively.

According to Eq: (3.4)-(3.7) and for a diameter of 11.73mm the length of the preform after the stretching is 1.25m Fig. 3.9.

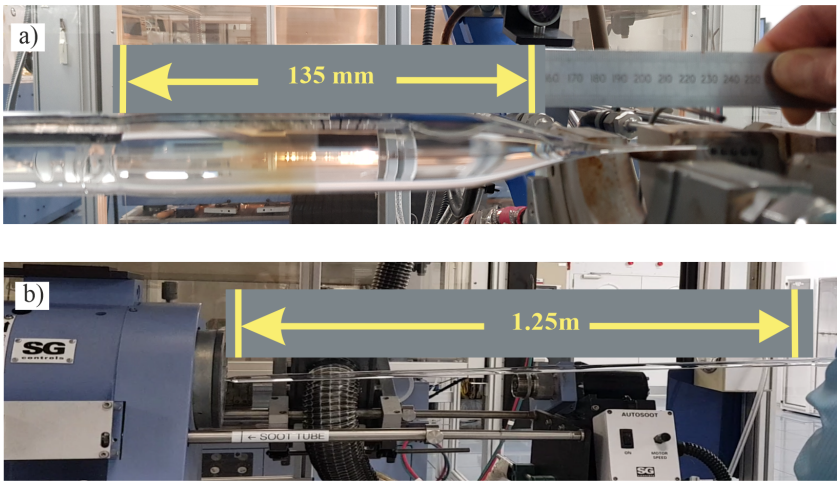

FIGURE 3.9: a) The length of the 7CF preform used for the fabrication of the ribbon fibre before stretching is 135mm while b) 1.25m after.

3.4.2 Sleeving

A sleeving tube with Cross Sectional Area (CSA) of 863.74mm and a length of 600mm was used for the process, Fig. 3.10.
The process starts with the preparation of that glass Fig. 3.10 (a). After polishing, it was then etched by using gas phase etching. In this technique SF_6 is used a precursor which reacts with SiO_2 according to the reaction [99],

$$SF_6(g) + \tfrac{3}{2}\,SiO_2(g) \rightarrow \tfrac{3}{2}\,SiF_4(g) + SO_2(g)^{+}\,\tfrac{1}{2}\,O_2(g)$$

This removes a layer of SiO_2 from the inner surface of the glass, where the diffusion of OH^- will have occurred, revealing a pristine uncontaminated layer [98]. The OH^- contamination may have three sources: a) thermal diffusion of OH^- from the starting deposition tube into the core during processing b) incorporation of OH^- from impurities in the starting reagents and carrier oxygen gas and c) contamination which results from leaks in the chemical delivery system.

Finally, the stretched 7CF rod was inserted into the sleeving tube, Fig. 3.10 (b) and it was sealed by putting it under vacuum Fig. 3.10 (c). It is noted that the length of preform with a uniform diameter was about 600mm, which is also the length of the sleeve tube. A significant amount of the glass is lost at the start of the stretching process as the process is being stabilised.

3.4.3 Milling

The surface of the glass was milled off in order to create rectangular sides, using a rotary grinding process. The sleeved preform was clamped on the milling bed

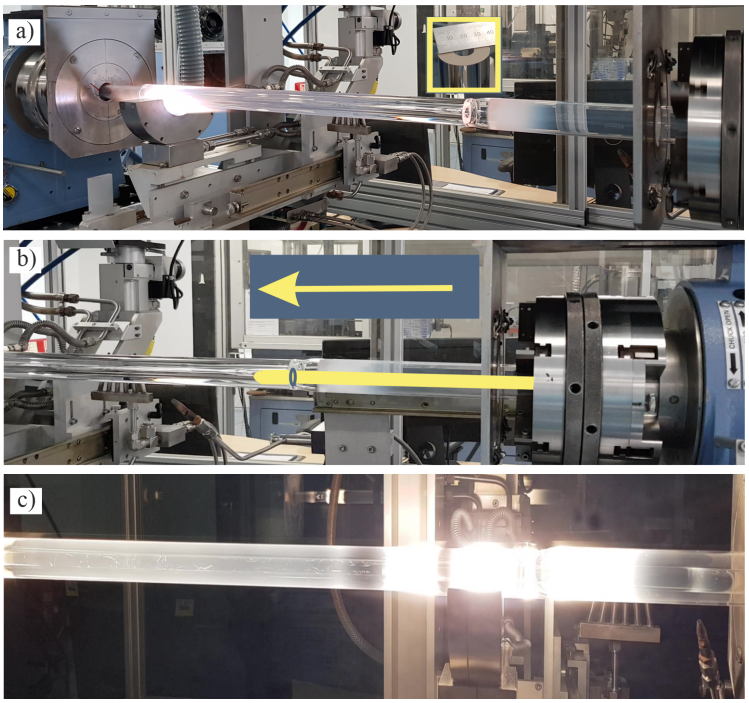

FIGURE 3.10: a) Preparation of the sleeving tube by polishing it and etching it using SF_6 The dimensions of the sleeving tube that was used for sleeving to 1:3 ratio were: Outer Diameter: 35.95mm, Inner Diameter: 13.88mm. Length: 600mm. b) Insertion of the stretched MCF preform into the sleeving tube. c) Sealing process.

Fig. 3.12 (a) and the diamond tool rotated as shown in Fig. 3.11 in order to grind the surface.

The bed was moved upwards by the milling-off step and once the milling tool came into contact with the glass, the bed was moved in the horizontal plane in order to grind along the length. The milling head has a diameter of 30mm but since the preform's horizontal dimension is 35mm the milling had to be performed in a rectangular shape as shown in the inset of Fig. 3.11 in order to cover the whole surface of the glass.

The head was moved by 12mm relative to the centre of the preform in order to mill off the right side. Once that side was finished it was moved −12mm relative to the centre, as shown in the inset of Fig. 3.11 in order to finish off with the left side. After milling the upper part of the preform it had to be rotated and clamped upside-down in order for the bottom part to be milled as well. The milling was performed in various steps. First a large volume of glass was milled off with a step of 500μm, Fig. 3.12 (b).

During the processing the preform cracked due to the force of the milling and the lack of support at the center of the length. This resulted in two separate preforms, with a length of 247mm and 300mm respectively that had to be milled independently. Before restarting the milling process, each one of the two preforms was first glued to an aluminium surface using hot glue to reduce the risk of further cracking whilst milling. The aluminium surfaces were then clamped onto the bed in order

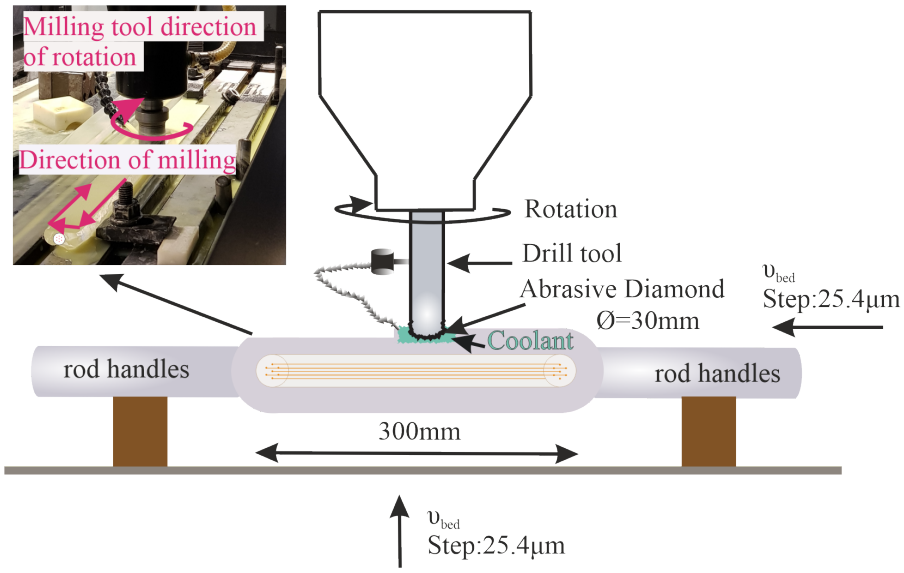

FIGURE 3.11: Top: The sleeved 7CF preform clamped on the milling bed. The bed can be moved upwards with a step of 25μm in order to adjust the amount of glass we want to take off. It can be also moved horizontally for milling along the length of the workpiece.

to subsequently carry on with the milling. The layout of the preform glued on the aluminium surface can be seen in the inset of Fig. 3.11. Each one of the two preforms was milled-off separately 3.12 (c).

Fig. 3.13 depicts the 247mm and 300mm in length preforms respectively, after their last milling pass. The deviation from the desired milling is $\pm 200\mu$m in preform resulting in a core position error of $\sim$ 200nm and $> 2\mu$m in fibre for the cores along the short and long axis respectively.
The offset of the cores could be attributed to the inability of the head to be locked in place. Because of that the bed had to be moved upwards which is less accurate than the head moving down.

One more factor affecting the milling accuracy is the flexing of the preform. As the surface of the glass is ground off, it bends away from the mill bit. This makes the glass thicker at one end so it creates uncertainty in the amount of glass milled off. To avoid this issue the entire preform had to be fixed in a metal plate so it can not bend. It is noted that the milling uncertainty due to the flexing of the preform affects only the short axis. The position error in the long axis is down to deformation during drawing, owing to the minimisation of energy and would require compensating for in the design stage by using feedback from a previous attempt.

3.4.4 Flat fibre draw

For coating standard circular fibres, circular coating is used. However, this coating geometry is not ideal for rectangular fibres as a flat surface is simpler to lay onto the structure under test. For the work described in this thesis, custom-made gravity fed rectangular split-dies were used with their dimensions shown in Fig. 3.15.

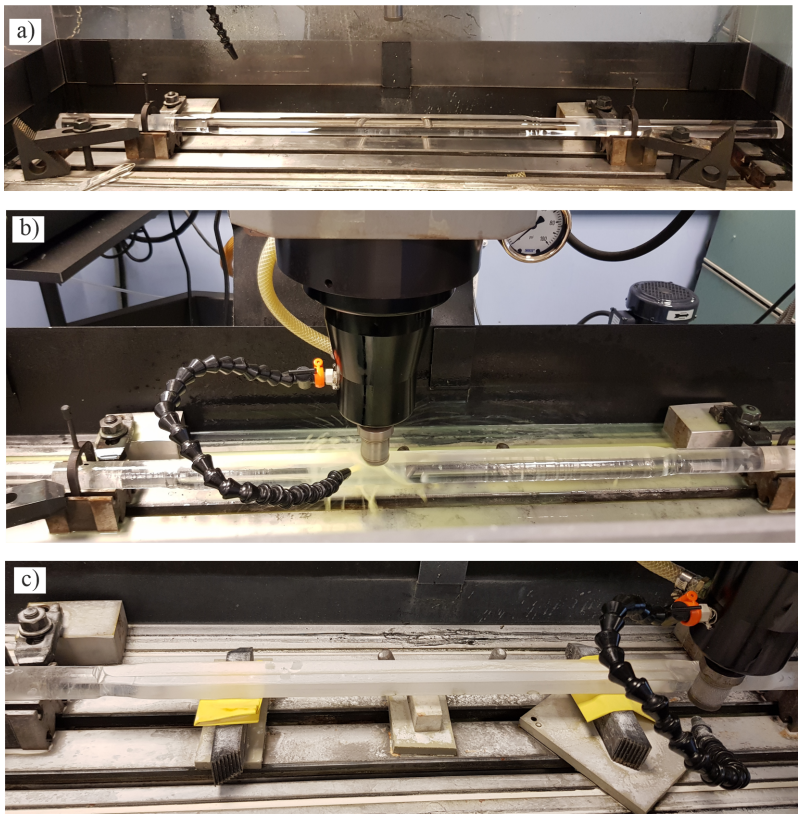

FIGURE 3.12: a) The sleeved 7CF preform clamped on the milling bed. b) The first pass of the drill, 500μm off. c) After having milled both sides. Supports have been added to avoid fracture due to the gradual thinning of the preform.

As was the case for the D-shaped fibre, it is also important to avoid any twist of the flat fibre during the draw since this will cause a frozen-in twist within the fibre. For the flat fibre draw, the furnace was operated at around 1830°, a temperature lower than the common draw temperature (2000°) that is necessary to avoid the circularisation of the fibre. The feed rate was 1.1mm/min, and the pulling speed was 10.1m/min.

Right beneath the coating applicator the two parts of the die were assembled together. In the case of flat fibre draw, a split die system a 500μm x 250μm die was used. This is for adding a 62.5μm coating thickness in all sides of the fibre. As the fibre passed through the die, the coating (DeSolite® $3471-3-14$) was applied and then the fibre went through the curing unit where the coating was solidified.

Two draws were performed with the first aiming to optimise the drawing temperature. As previously mentioned this type of fibre needs to be pulled in a temperature lower than the usual temperature the circular fibres are drawn for the geometry to be preserved. As a starting point, the first pull was attempted at a temperature of 1910°. It is worth noting that in order for the preform to be clamped in the drawing tower, a circular rod had to be attached to the rectangular preform. This is the end that is drawn last and it is called End of the Pull (EOP). The attachment of a circular rod to the rectangular preform leaves the edges of the preform unsupported

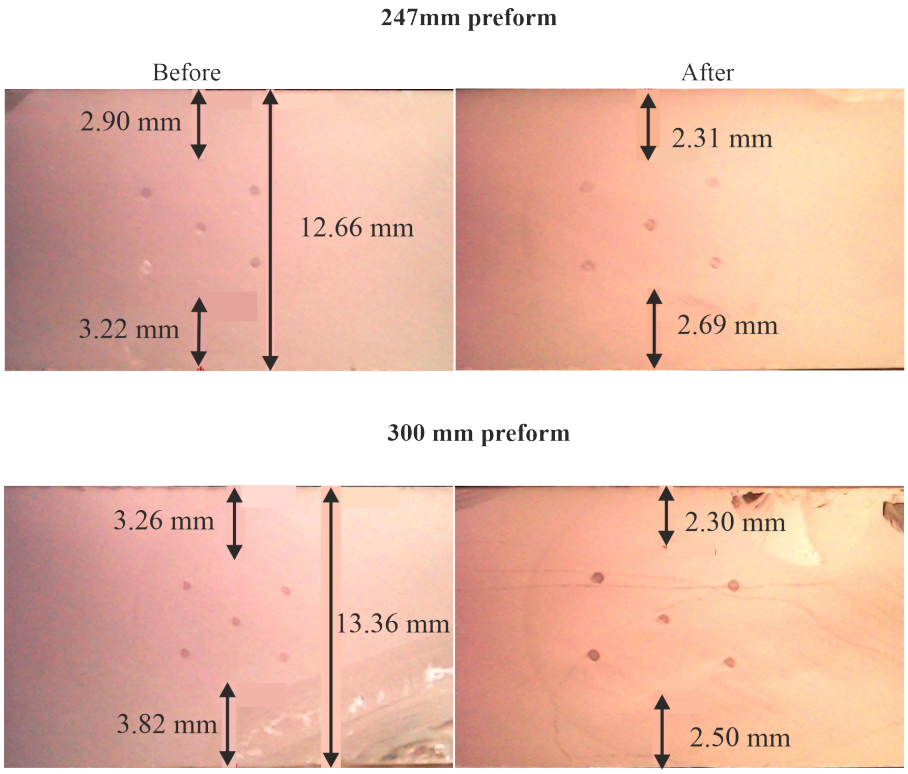

FIGURE 3.13: Preform dimensions before and after the last milling pass for a 247mm and 300mm preform.

and as a result the edges are drawn first and so the fibre becomes more rounded compared to the Beginning Of Pull (BOP) as depicted in Fig. 3.14 EOP-Draw 1.

At the second attempt of the first pull the temperature was reduced to 1810° to stiffen up the neck down (from preform to fibre) to reduce the likelihood of twisting. It is noted that the intercore distances are significantly smaller than 35μm, Fig. 3.14 and so a second draw needs to be attempted. It is also stressed that due to the nature of the first draw which was essentially a test draw, a lot of fibre was lost in the optimisation process and the large difference between the BOP and EOP is due to the fact that we effectively got only the very end of EOP side.

After optimising the temperature during the first draw a second one was performed at a temperature of 1830°. The cross-sections of the BOP and EOP are shown in Fig. 3.14. It is noted that there is a small difference in the dimensions between the BOP and the EOP something that is expected. Also, the short axis has a tendency to expand while the longer axis has a tendency to contract, as the structure attempts to become more round due to the minimisation of energy.

There are some challenges in the fabrication of the flat fibre. The first one refers to the preservation of the rectangular geometry during the draw that can be addressed by optimising the draw temperature, requiring trial and error. A second problem area is the twist of the fibre as it is being pulled down. The twist has an impact on the measurement of the diameter as the diameter gauge is set up for circular fibres whose diameters do not change as they are drawn. When the rectangular

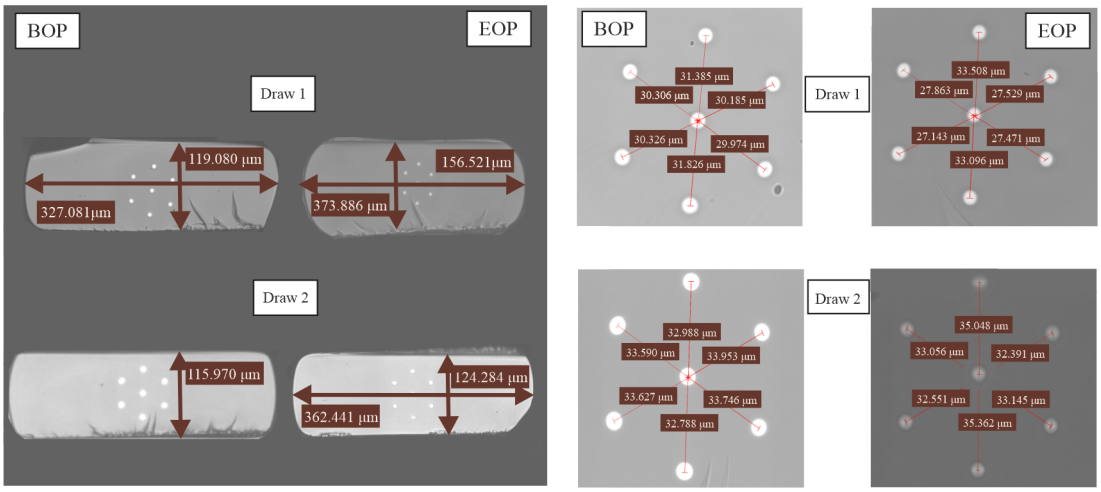

FIGURE 3.14: Pictures of the cross sections and their intercore measurements of the fibre for both ends (Beginning Of Pull and End Of Pull) for Draw 1 and Draw 2.

fibre twists, the shadow changes and the diameter reading will subsequently change without necessarily reflecting a true change in the fibre diameter. A false reading of the diameter will lead the user to a modification of the feed rate and draw speed, and those changes may affect the geometry of the finished fibre.

3.5 Summary

In this chapter a detailed description of the process used for the fabrication of the multi-core fibres used in this study is provided. The manufacturing stages of stretching, sleeving and milling are described and the differences in the fibre draw processes between the D-shaped and the flat fibre are mentioned. The standard 7CF, the D-shaped 7CF and the flat 7CF have been fabricated in house by Dr. Laurence Cooper for the purposes of this PhD project.

In the next chapter the shape sensing results using a D-shaped fibre, are presented.

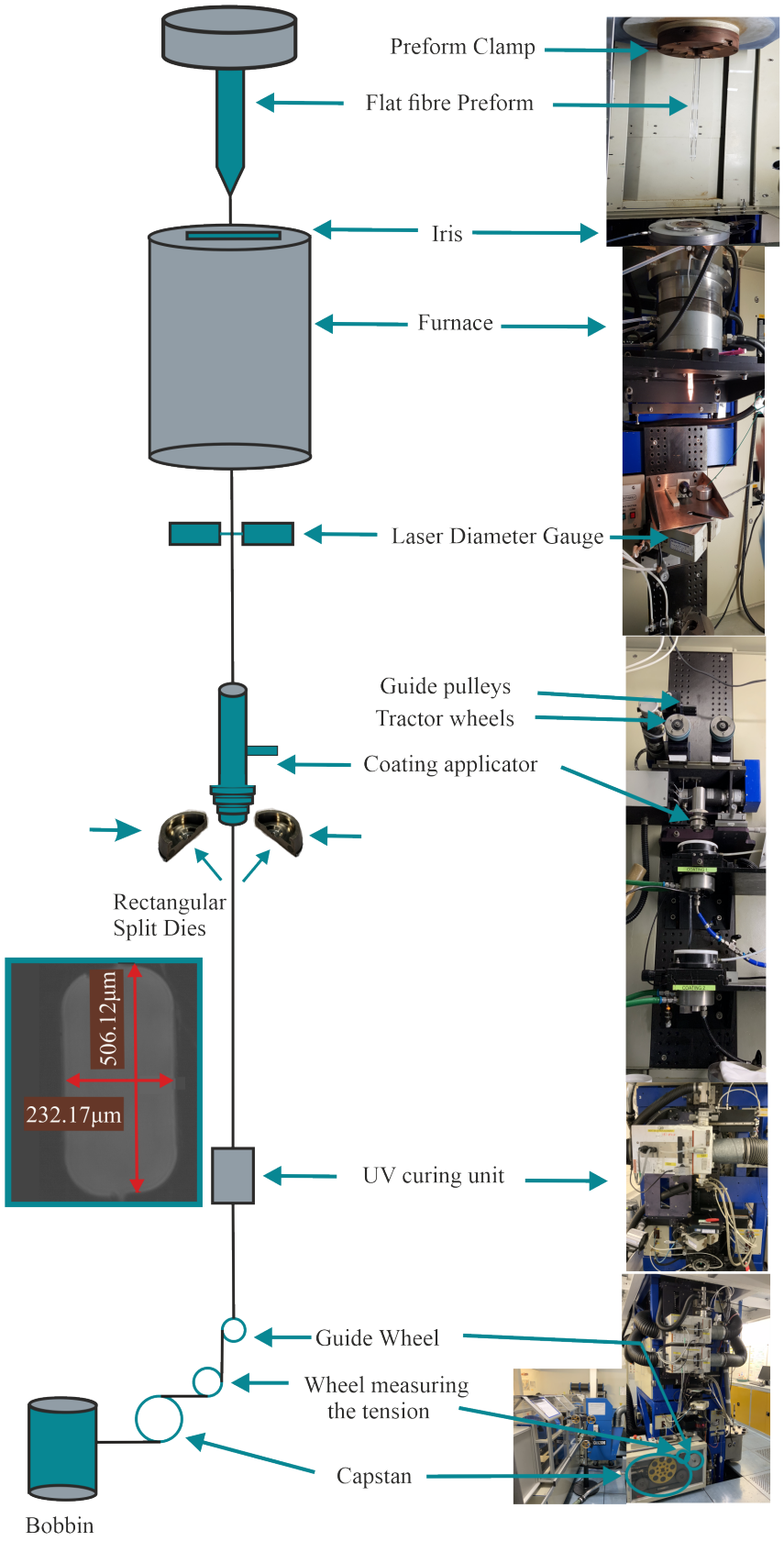

FIGURE 3.15: Schematic of the drawing tower configuration used for the flat fabrication. Custom made rectangular split dies have been used for this type of draw.

Chapter 4

Curvature sensing based on a D-shaped fibre

4.1 Introduction

A common obstacle when attempting to do shape sensing using multi-core optical fibres, is the random twist of the fibre that is introduced when the fibre is wrapped around the structure of interest. This twist can distort the 3-axes coordinate system needed for shape or curvature sensing which subsequently results in a large error in the determination of the curvature. In the work by Zhao et al. [19], an optical microscope was used to manually orient the fibre and maintain the relative position of the cores with respect to the bending plane, as discussed in section 2.6.2. However, this approach might be impractical as it is extremely time-consuming and cannot be easily implemented in the field.

In this work, a multi-core fibre with a D-shape geometry is proposed as a way to achieve preferential bending. A fibre with said geometry bends preferentially along a certain direction due to its asymmetry, based on the fact that it is thinner along the axis where the milled side is and the associated moment of inertia is maximum. As a result, the energy required for compression and stretching of the fibre along the axis that is parallel to the flat side is minimized, forcing the fibre to always bend along a plane which is parallel to the flat side. Although BOTDA is a powerful technique for long range sensing, it requires access to both ends of the fibre. In contrast to BOTDA, the approach used in this work that is based on BOTDR, requires a simpler interrogation setup and access to only one end of the sensing fibre.

The underlying principle of curvature sensing is detailed in section 4.2 followed by a description of the experimental setup in section 4.3. It is noted that the BOTDR setup was designed, assembled and tested for this project by the author. The experimental procedure and the curvature results related to this new, D-shaped multi-core fibre are presented in sections 4.4 and 4.3 respectively. Discussion and analysis of the experimental results are presented in section 4.6 and the final section highlights the outcome of the study.

4.2 Principle of Operation

The operation of the sensor is based on measuring the strain-induced Brillouin Frequency Shift (BFS), that was discussed in section 2.4.4, in different cores of a MCF. As the fibre bends, different cores of the MCF experience different strain levels. By

measuring the BFS in different cores, the curvature can be calculated. In this section, the impact of bending on the BFS of different cores of a 7-Core Fibre (7CF) is analysed and the equation that determines the curvature of the fibre is derived [18].

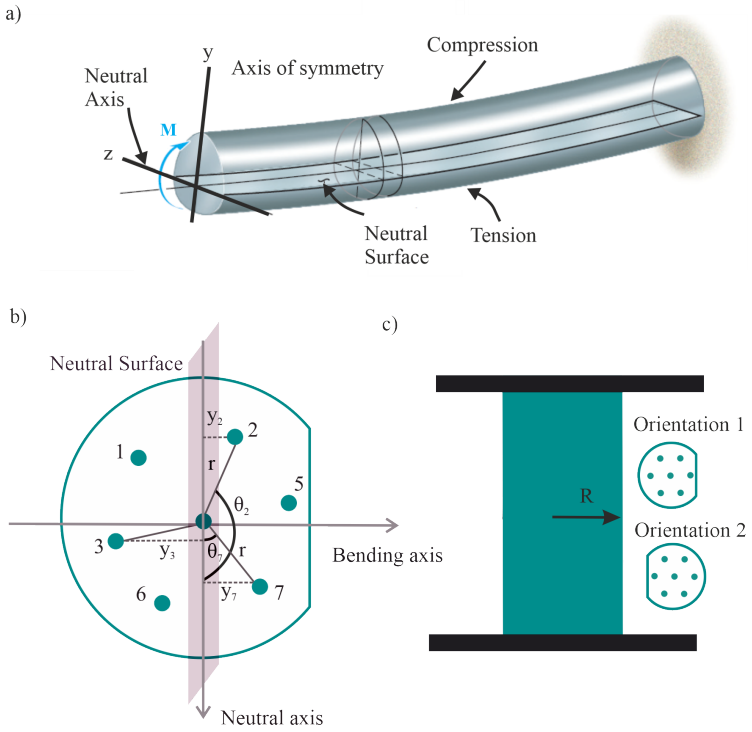

FIGURE 4.1: (a) Deformation of a beam due to bending. One region of the beam is under tension (positive strain) the other is under compression (negative strain), depending on the direction of the bending moment. There is a surface along the middle where the length remains the same and so the strain is zero. This surface is called neutral surface and the axis that lies along this surface and is normal to the bending axis is called neutral axis (b) Coordinate system and cores' arrangement relative to the neutral axis. (c) Preferential bending of the D-shaped 7CF around the bobbin. The bending plane is parallel to the flat side of the fibre.

Consider a uniform, homogeneous beam with a cross-sectional area that is symmetric around an axis subjected to bending and the bending moment is applied perpendicular to an axis of symmetry as shown in Fig. 4.1(a). In this case the bending moment causes the material within the bottom portion of the bar to stretch and the material within the top portion to compress. Consequently, between these two regions there must be a surface, called the neutral surface, in which the material will not undergo a change in length [100]. This axis, that lies along the neutral surface is called the neutral axis. The above description applies to the case of an optical fibre as well [18] and so by using the strain-curvature relationship [100] for the fibre cross-section shown in Fig. 4.1(b) the radius of curvature can be written as,

$$R = \frac{y_2}{\epsilon_{2,4}} = \frac{y_7}{\epsilon_{7,4}} \tag{4.1}$$

$$R = \frac{y_2}{\epsilon_{2,4}} = \frac{y_3}{\epsilon_{3,4}}, \tag{4.2}$$

where R is the radius of curvature, y_2, y_3, y_7 are the distances of the cores $2, 3, 7$ from the neutral axis, respectively and $\epsilon_{2,4}, \epsilon_{3,4}, \epsilon_{7,4}$ are the difference in the strain values between cores $2, 3, 7$ and the central core (core 4), respectively. From Fig. 4.1 (a), it can be shown that:

$$y_2 = r_2 \cdot \sin\theta_2 = r_2 \cdot \sin\left(\theta_7 + \frac{2\pi}{3}\right) \tag{4.3}$$

$$y_3 = r_3 \cdot \sin\theta_3 = r_3 \cdot \sin\left(\theta_2 + \frac{2\pi}{3}\right) \tag{4.4}$$

$$y_7 = r_7 \cdot \sin\theta_7, \tag{4.5}$$

where $r_2 = r_3 = r_7 = 35\mu$m is the 7CF core pitch and $\theta_2, \theta_3, \theta_7$ are the angles between cores $2, 3, 7$ and the neutral axis, respectively. By substituting Eqs. (4.3), (4.4) and (4.5) into Eqs. (4.1) and (4.2) and using some mathematical manipulation, it can be shown that:

$$\theta_2 = \cot^{-1}\left(\frac{\frac{\epsilon_{3,4}}{\epsilon_{2,4}} - \cos\left(\frac{2\pi}{3}\right)}{\sin\left(\frac{2\pi}{3}\right)}\right) \tag{4.6}$$

$$\theta_7 = \cot^{-1}\left(\frac{\frac{\epsilon_{2,4}}{\epsilon_{7,4}} - \cos\left(\frac{2\pi}{3}\right)}{\sin\left(\frac{2\pi}{3}\right)}\right). \tag{4.7}$$

In these equations, the values of $\epsilon_{2,4}$, $\epsilon_{3,4}$, and $\epsilon_{7,4}$ are determined by measuring the BFS using a BOTDR setup and the strain information is then used to determine the values of θ_2 and θ_7. By replacing the value of θ_2 and θ_7 in Eq. (4.4) and (4.3) the values of r_3, r_2 can be calculated. Finally, by substituting these values in Eq. (4.1) and Eq. (4.2), the radius of curvature is determined. To simplify the mathematical analysis, it is assumed that the opposite cores within the 7CF experience similar strain levels with opposite signs.

4.3 Experimental Setup

Fig. 4.2 shows a schematic diagram of the experimental setup that can be divided into three principal sections. The pulse generation, the sensing as well as the microwave detection section.

Light from a Tunable Laser Source (TLS) at 1533 nm is amplified by an Erbium-Doped Amplifier (EDFA 1) and then split by a 70/30 coupler. Light from the 70% arm of the coupler is amplitude-modulated using an Electro-Optic Modulator (EOM) to generate a train of 20 ns pulses with a repetition rate of 1 MHz.

The light is further amplified by another amplifier (EDFA 2) before entering an Acousto-Optic Modulator (AOM), which limits the Amplified Spontaneous Emission (ASE). ASE is the process by which a 980nm photon, that is absorbed by the valence electrons and subsequently excited to the conduction band, decays back to the valence band by the emission of a photon. This decay happens after a certain time that depends on the electron lifetime in that state.

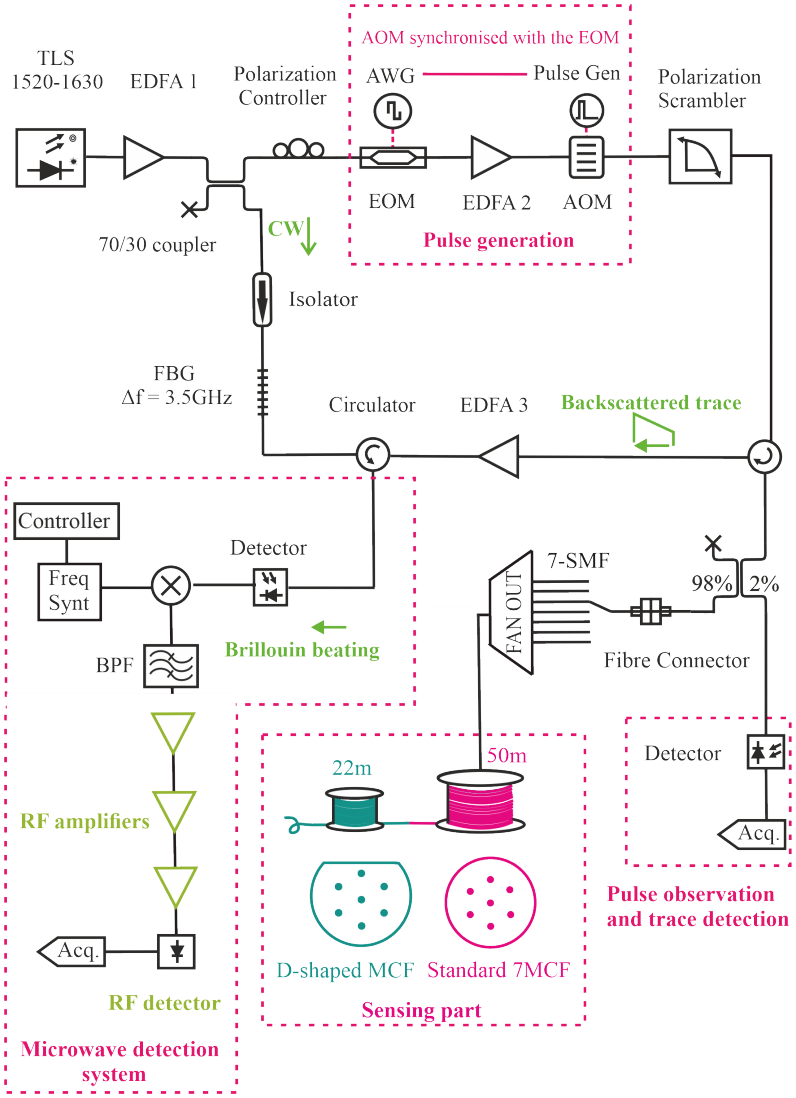

FIGURE 4.2: Experimental Setup. TLS, Tunable Laser Source; AWG, Arbitrary Wave Function; EOM, Electro-Optic Modulator; EDFA, Erbium-Doped Fibre Amplifier; AOM, Acousto-Optic Modulator; BPF, Band Pass Filtre; YIG, Yttrium Iron Garnet synthesiser; Freq Synt, Frequency Synthesiser.

The ASE lasts for the duration of the pumping and adds noise to the detector since the pulse "sits" on top of the ASE background which may saturate the detector. To remove the ASE an AOM is required which is synchronised with the EOM, Fig. 4.3. The AOM operates by diffracting the light due to a periodic refractive index variation in the crystal which is caused by a piezoelectric element.

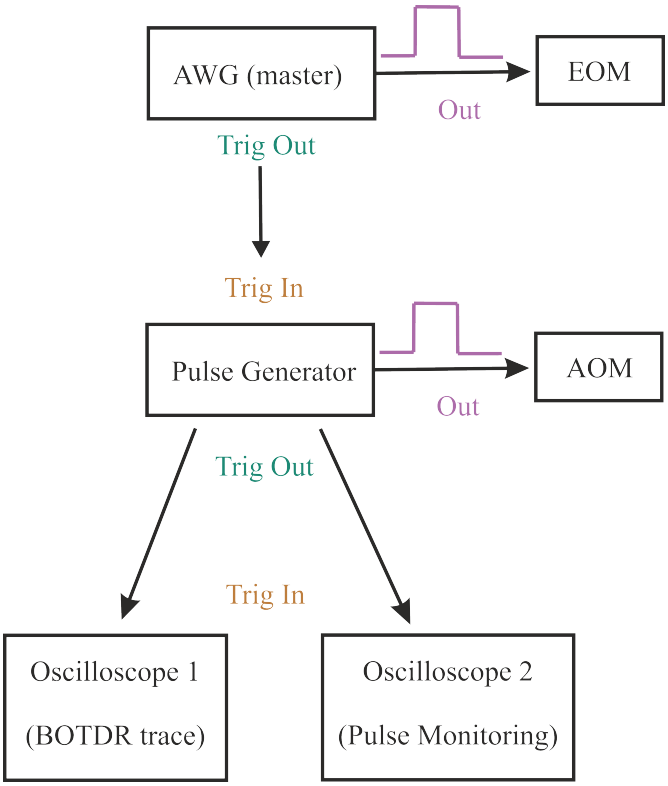

FIGURE 4.3: The Arbitrary Waveform Generator (AWG) output is used as the EOM input. The AWG also triggers the pulse generator whose output is the input of the AOM. In this way the EOM is synchronised with the AOM. The pulse generator triggers the two oscilloscopes which serve for the pulse monitoring as well as for receiving the Brillouin OTDR signal.

When the two devices are synchronised light passes only for the duration of the pulse. In this way only a part of the generated ASE (the part that has a duration that coincides with the duration of the pulse) reaches the detector instead of the whole amount that is generated throughout the whole time the pumping lasts. An AOM is used, instead of an EOM, due to its higher extinction ratio (50dB to 55dB) compared to (20dB) of the EOM.

After the pulse has been generated, it enters a polarisation scrambler. This is crucial for the mixing afterwards. By scrambling the polarisation entering the fibre, the polarization of the light that is backscattered is also scrambled. So when light coming from the TLS is mixed with the backscattered light of random polarisation coming from the sensing fibre, polarization fading is avoided. Polarisation fading refers to fact that the Brillouin interaction between the backscattered light and the light coming from the source depends on the degree of parallelism of the States of Polarisation (SOPs) [69]. When the SOPs are mutually orthogonal they do not interact. By scrambling the state of polarisation of the backscattered light and averaging the sensor readings over multiple pulses, a sufficient SNR can be recorded.

The amplified probe pulse with a peak power of 1 W is then launched into the sensing fibre via the first port of a circulator. The peak power is set in such a way

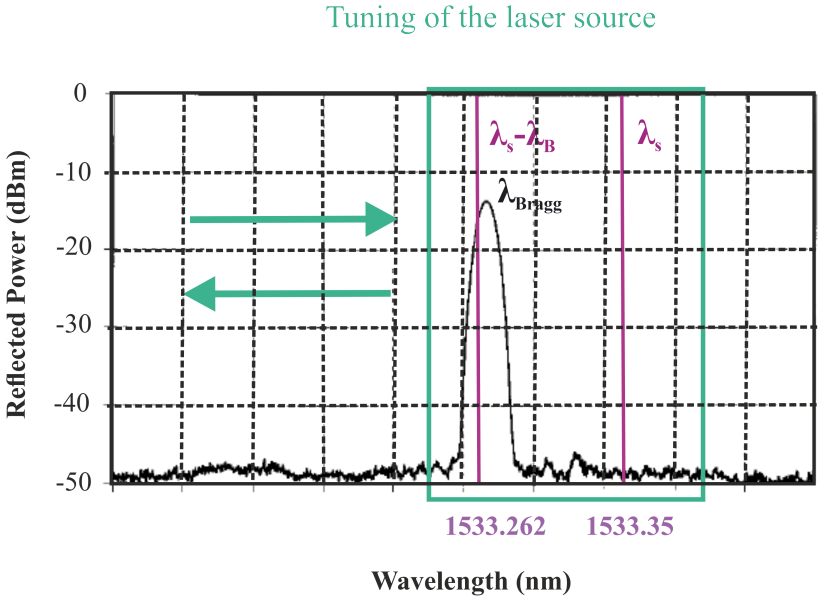

FIGURE 4.4: The FBG is used to separate the Brillouin component from the Rayleigh. The reflection spectrum was taken by [101] and has been edited to serve as an example.

so as to avoid non linear Brillouin and Raman scattering effects, section 2.4.5. A 98/2 tap coupler is added after the second port of the circulator to allow to 2% of the power to be used to monitor the probe pulse, while the remaining 98% of the power is sent to the sensing fibre via a fanout demultiplexer. The fabrication process of this fanout device is described in section 2.3.1. A 50 m length of standard 7CF is spliced to 22 m of D-shaped 7CF. The backscattered light from the sensing fibre, returns through the third port of the circulator to the setup and it is amplified by a third optical amplifier (EDFA 3).

A narrow bandwidth FBG ($\lambda_B = 1533.35$ nm, BW = 3.5 GHz) is used to separate the Brillouin anti-Stokes from the Rayleigh backscattering. The frequency of the continuous wave is tuned in such a way so as for the backscattered Brillouin component to be in the reflection spectrum of the FBG. This means that the Rayleigh component of the backscattered light, which has the same frequency (wavelength) as the source, λ_s will pass through, since it will be in the transmission window of the FBG, while the Brillouin anti-Stokes backscattered component which is at wavelength $\lambda_s - \lambda_{Brillouin}$ will be reflected. Fig. 4.4 shows the way the frequency of the source is tuned in order for the Brillouin component to be within the FBG's transmission window.

After isolating the Brillouin component, the Brillouin backscattered trace is mixed with the seed laser source and the generated beat signal, corresponding to the Brillouin frequency shift at around 11 GHz, is detected using a 15 GHz photodetector with a responsitivity $I \sim 0.95$A/W at 1550 nm. The optical mixing is necessary since the Brillouin component has a frequency of $f_s + f_B$ which is at $\sim$ 193 THz and therefore cannot be detected by any commercial detector due to the limited

bandwidth of the electronic components. In an optical heterodyne detection scheme the current at the output of the square-law detector is given by [102],

$$\begin{aligned}
\mathrm{I_{photodiode}} &\sim |\ \mathrm{E_s} + \mathrm{E_b}\ |^2 \\
&= \left[|\mathbf{E}_\mathrm{s}|e^{i(\kappa\mathbf{r}+\omega_\mathrm{s}t)} + |\mathbf{E}_\mathrm{b}|e^{i(\kappa\mathbf{r}+\omega_\mathrm{b}t)}\right]\left[|\mathbf{E}_\mathrm{s}|e^{i(\kappa\mathbf{r}+\omega_\mathrm{s}t)} + |\mathbf{E}_\mathrm{b}|e^{i(\kappa\mathbf{r}+\omega_\mathrm{b}t)}\right]^* \\
&= |\mathbf{E}_\mathrm{s}|^2 + |\mathbf{E}_\mathrm{b}|^2 + |\mathbf{E}_\mathrm{s}||\mathbf{E}_\mathrm{b}|e^{i(\omega_s-\omega_b)t} + |\mathbf{E}_\mathrm{s}||\mathbf{E}_\mathrm{b}|e^{-i(\omega_s-\omega_b)t} \Rightarrow \\
\mathrm{I_{photodiode}} &= |\mathbf{E}_\mathrm{s}|^2 + |\mathbf{E}_\mathrm{b}|^2 + 2|\mathbf{E}_\mathrm{s}||\mathbf{E}_\mathrm{b}|\cos[(\omega_s-\omega_b)t]
\end{aligned}$$

where the * denotes the complex conjugate and,

$$\begin{aligned}
\mathbf{E}_\mathrm{s}(\mathbf{r},t) &= |\mathbf{E}_\mathrm{s}|e^{i(\kappa\mathbf{r}+\omega_\mathrm{s}t)} \\
\mathbf{E}_\mathrm{b}(\mathbf{r},t) &= |\mathbf{E}_\mathrm{b}|e^{i(\kappa\mathbf{r}+\omega_\mathrm{b}t)}
\end{aligned}$$

correspond to the electric field of the source and backscatter light respectively. The high frequency the terms cannot pass through the 15 GHz photodetector so it is the Brillouin frequency shift term at around 11 GHz that passes through.

At the last section of the setup the electronic mixing takes place. To generate the 3D BGS it is essential to scan all the frequencies around the Brillouin peak. To do so, the frequencies have to be down-converted using a microwave detection system. The down-conversion is necessary since a 5GSa/s (period $2\cdot10^{10}$s), 350MHz bandwidth oscilloscope is used for the acquisition, while the signal to be detected has a period of $1\cdot10^{-10}$s. This means that there is only one data point within one acquisition period and so according to the Nyquist theorem [103], the signal cannot be reconstructed successfully.

To translate the signal in frequency a mixer has to be used. A mixer produces an output signal that is the product of the two input signals. Passive mixers use one or more diodes and rely on their non-linear relation between voltage and current to provide the multiplying element [104]. For simplicity one ideal diode can be considered, whose current is given by [105]:

$$I = I_s(e^{\frac{eV}{\kappa T}} - 1) \tag{4.8}$$

where I_s is the reverse bias saturation current, V is the voltage across the diode, k is the Boltzmann constant, T is the absolute temperature of the p-n junction and e is the magnitude of the charge of the electron. Using a Taylor expansion and keeping only the first non-linear term, the current of the diode I can be written as,

$$I = I_s \frac{e}{\kappa T}\left(V - \frac{e}{2\kappa T}V^2\right) \tag{4.9}$$

In our case the 11 GHz Brillouin signal is mixed with frequencies at ~ 10 GHz produced by an YIG synthesiser. As a result, the voltage reaching the mixer is the sum of the voltage of the frequency synthesiser $V_{\text{synthesiser}}$ and the voltage of the Brillouin backscattered $V_{\text{Brillouin}}$, $V = V_{\text{synthesiser}} + V_{\text{Brillouin}}$.
If $V_{\text{synthesiser}} = V_0 \sin(2\pi f_{\text{synth}} t)$ and $V_{\text{Brillouin}} = V_1 \sin(2\pi f_{\text{Brillouin}} t)$ then the quadratic term of the Taylor expansion results in higher frequency terms and a term $\cos\,[2\pi(f_{\text{synth}} - f_{\text{Brillouin}})t]$ - as described in Eq. (4.3) - which gives an Intermediate Frequency (IF) of $\sim$ 1GHz.

After mixing, the signal is passed through a Band-Pass Filter (BPF) centred at 1 GHz, with a bandwidth of 50 MHz. The higher frequency terms cannot pass through the filter and so it is only the intermediate term that passes through.

Finally, the IF signal is amplified by three RF amplifiers with a gain of 30 dB each at 1 GHz and then it is rectified using a microwave diode rectifier that generates a signal proportional to the intensity of the Brillouin backscattering at the chosen frequency. The signal is then sent to an oscilloscope that collects the trace for every scanned frequency.

4.4 Experimental Procedure

Four spools of different diameter (59 mm, 114 mm, 150 mm, 227 mm) were used for the curvature test. 22 m of the D-shaped fibre were wrapped around each of the spools using a rewinding machine and four different tests were carried out separately. Typical attenuation values of a MCF are $\simeq$ 1dB/Km. It is noted that a 10m/min rewinding speed was used to ensure that the D-shaped fibre would keep its orientation during the rewinding process. This speed is low compared to the 500m/min that is normally used when rewinding the standard fibres. The frequencies of the YIG synthesiser were scanned through a 300 MHz frequency range at 5 MHz steps using an Arduino controller. The selected YIG frequency determined the Brillouin beat frequency that was measured: i.e. the measured component of the Brillouin spectrum was equal to the YIG frequency plus 1 GHz (the IF). The signal was fed to a storage oscilloscope with a sampling rate of 5 GSa/s, which was used to average 10,000 time-domain traces to improve the Signal to Noise Ratio (SNR). The traces were then transferred to the PC and the Brillouin spectra were built by collecting such traces over a range of frequencies determined by the YIG synthesizer [106]. The processes of scanning the frequencies, capturing the data and building the Brillouin gain spectra were automated using a Python script. The automation process, described in detail in Appendix A reduces the time needed for a complete set of measurements and hence eliminates the introduction of errors due to temperature variations or drift of the electronic equipment.

4.5 Results

Fig. 4.5 shows the anti-Stokes Brillouin gain spectrum (BGS) of an outer core of a standard 7CF from 0 m to 60 m spliced to 22 m of D-shaped 7CF. As mentioned earlier, the D-shaped fibre shows a preferential bending direction with its neutral plane parallel to the flat side. This results in insignificant twist of the cores across the length. This phenomenon can be clearly seen in Fig. 4.5 where the BGS corresponding to the D-shaped fibre shows little deviation from its mean value compared with the BGS of the standard 7CF which exhibits notable fluctuations. The horizontal and vertical axes of this diagram represent the distance along the sensing fibre and the BFS, respectively.

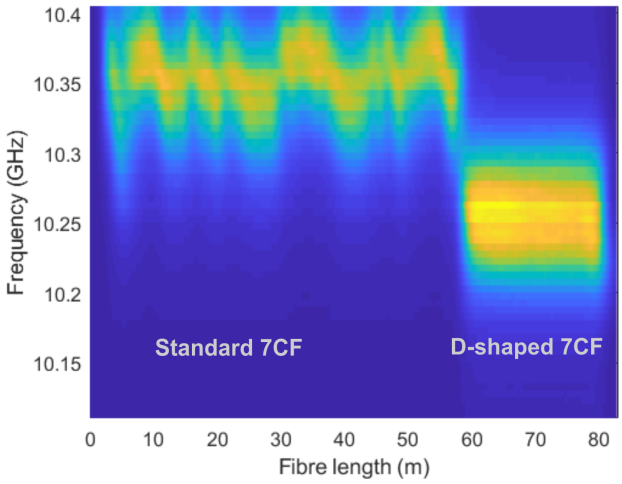

FIGURE 4.5: BGS of an outer core of a standard 7-core fibre (0 m – 60 m) and of a D-shaped 7-core fibre (60 m – 80 m).

4.6 Discussion

Fig. 4.6 shows the fitted curves for the anti-Stokes BGS as a function of the frequency shift for six out of seven cores at the distance of 64.18 m of the D-shaped 7CF wrapped on a 114 mm diameter bobbin. It should be noted that the core closest to the milled side experiences high mode leakage losses and hence it is not taken into consideration for the curvature calculations.

The strain levels corresponding to opposite cores were compensated so as to be symmetrical around zero as shown in Fig. 4.7(a). More specifically, the pairs of cores 1 & 7, 2 & 6 and 3 & 5 are expected to experience values of strain equal in amplitude but opposite in sign, since they are located in diametrically opposite sides within the fibre cladding, as shown in Fig. 4.1(a). However, in practice, the strain values of the opposite cores are not completely symmetric around zero due to the fact that the position of the bending plane does not coincide with the position of the neutral core that has been used as a reference. An additional source of error resides in the different types of preforms used to produce the various cores, which might result in

additional in-built stress. This is due to the fact that during the fabrication process preforms with non identical refractive indices are usually used as the core material. This happens due to size limitations, as a standard-sized preform will make a single core fibre. For the fabrication of a 7CF, there is a requirement of 7 times the core material to make the same length of fibre. Practically, this means that two to three different preforms have to be used to make one multi-core fibre. Although this is expected to create a small discrepancy in the strain coefficient of the cores [107], a compensation process is applied to alleviate this issue. More specifically, the mean strain value of a said core and the core opposite to it was subtracted from the strain value of the said core at a specific position. For instance,

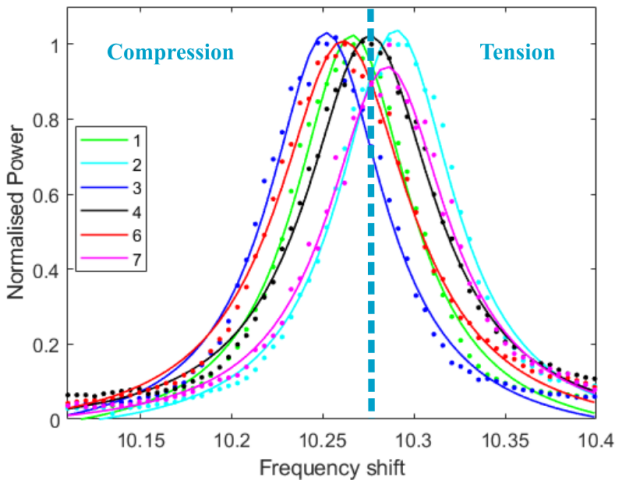

FIGURE 4.6: BGS of a D-shaped fibre wrapped on a 114 mm spool at 64.18 m. Cores 1, 3, and 6 are under compression relative to core 4 (central) while cores 2, and 7 are under tension.

$$\epsilon_1(\mathrm{x_i})_{\mathrm{comp}} = \epsilon_1(\mathrm{x_i}) - \epsilon_{\mathrm{mean}}(\mathrm{x_i}) \tag{4.10}$$

$$\epsilon_{\mathrm{mean}}(\mathrm{x_i}) = \left[\frac{\epsilon_1(\mathrm{x_i}) + \epsilon_7(\mathrm{x_i})}{2}\right], \tag{4.11}$$

where $\epsilon_{\mathrm{comp}}(\mathrm{x_i})$ represents the compensated strain of core 1 at position i. A similar procedure was followed for the pair of cores 2 & 6. However the strain values of core 3 were not compensated since the core positioned opposite to it, core 5, was experiencing high mode leakage due to its proximity to the flat side of the D-shaped fibre.

The bending radius at 64.18 m was calculated using three non-adjacent cores and Eq. (4.1)-(4.7). The BFS for each core, calculated by Lorentzian fits, were $f_1 = 10.2661\,\mathrm{GHz}$, $f_2 = 10.2901\,\mathrm{GHz}$, $f_3 = 10.2518\,\mathrm{GHz}$, $f_4 = 10.2757\,\mathrm{GHz}$, $f_6 = 10.2613\,\mathrm{GHz}$, and $f_7 = 10.2852\,\mathrm{GHz}$. Using the strain coefficient value of $0.046\,\mathrm{MHz}/\mu\epsilon$ [108] for all cores and the strain compensation method described above, the strain level of the cores were, $\epsilon_1 = -207.32\,\mu\epsilon$, $\epsilon_2 = 312.49\,\mu\epsilon$, $\epsilon_3 =$

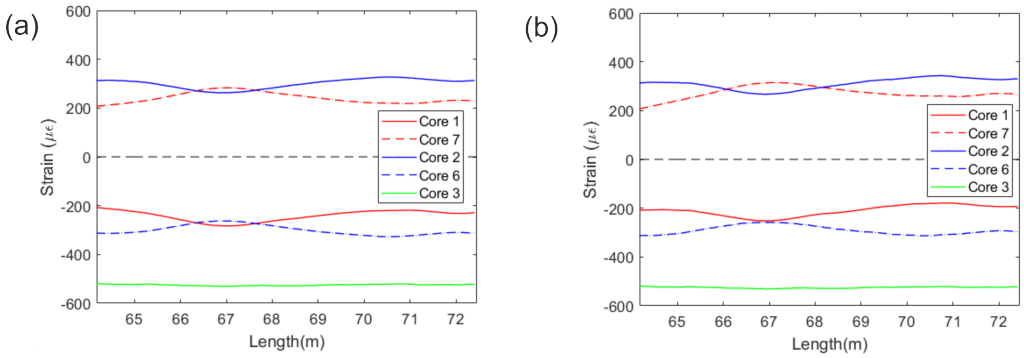

FIGURE 4.7: Strain distribution as a function of length. Core 5 is not depicted due to the high mode leakage loss. (a) With compensation. (b) Without compensation.

$-518.82\,\mu\epsilon$, $\epsilon_6 = -312.49\,\mu\epsilon$, and $\epsilon_7 = -207.32\,\mu\epsilon$. The strain values were replaced in Eq. (4.6) - (4.7) to determine $\theta_2 = -0.6412$, and $\theta_7 = 0.4073$. The values of θ were substituted in Eq. (4.3) - (4.5) to obtain $r_2 = 20.8987\,\mu$m, $r_3 = 34.7583\,\mu$m, and $r_7 = 13.8649\,\mu$m. The values of r_2, r_3, r_7 and ϵ_2, ϵ_3, ϵ_7 were replaced to Eq. (4.1), (4.2) to determine the radii of $R_2 = 6.6878$ cm, $R_3 = -6.6995$ cm, and $R_7 = 6.6878$ cm. The mean radius of the three cores was subsequently calculated to determine the radius of the fibre at that point. This process was repeated for all the points along the sensing fibre. Finally, the mean bending radius along the length of the fibre as well as the standard deviation, were determined for that spool.

The experimental procedure as well as the analysis described in section 4.4, 4.6 were repeated for the three remaining spools resulting in three independent tests that were carried out separately. Similar diagrams of normalised power as a function of frequency shift were created for each core of the three remaining bobbins and the BGS from non-adjacent cores were used to calculate the bending radius of each bobbin.

Fig. 4.9 shows the mean bending radius along the length of 2.5 m as well as their standard deviation for the four different spools used in this study, as a function of the actual bending radii. The blue curve depicts the ideal relation between the theoretical and the experimental values. The measurements match the expected linear behaviour.

A possible source of error is the noise originated from various components of the system such as the detector or the amplifiers. A drift in the laser intensity, as well as the temperature variation during the scanning of the frequencies which takes around 7 minutes, could also affect the accuracy in the determination of the bending radius.

The D-shaped fibre greatly enhances the preferential bending compared to the standard circular 7CF, as shown in the BGS of Fig. 4.5 where the twist of the standard fibre is reflected to the fluctuations of the BGS. Despite this significant improvement, the D-shaped fibre still experiences flips when it is wrapped around the bobbin with either the flat side of the fibre being in the inner part of the bobbin

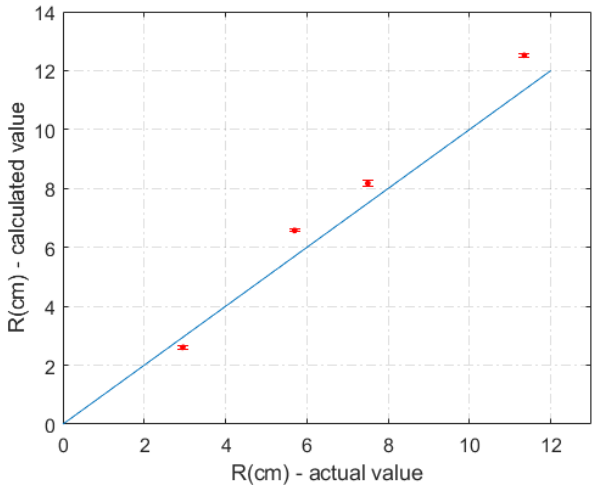

FIGURE 4.8: Measured bending radius against the real bending radius.

or in the outer as shown in Fig. 4.1. These flips are reflected in the BGS as regions of up-shift and down-shift around a central value.

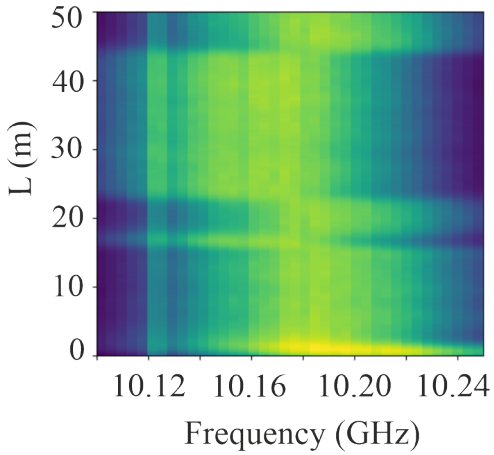

FIGURE 4.9: BGS of an outer core or the case of a D shaped fibre wrapped around a bobbin. Two distinct regions of up-shift and down-shift are clearly seen, corresponding to the flip of the D-shaped fibre while it is being wrapped around the bobbin. The flip happens between two possible configurations of the fibre in relation to the bobbin. The flat side can reside either on the inner part of the spool or on the outer.

Those flips although only distort the sign of the curvature (positive or negative) render it challenging to accurately determine the bending radius when it comes to a case of long range sensing. In the above picture there are flips happening throughout the 50m long fibre.

In the next chapter, a MC fibre with both sides flat will be investigated for curvature sensing purposes. This fibre offers the advantage of an enhanced preferential bending owing to the two flat sides that aim to the elimination of the fibre twist.

This unique fibre offers an easier application on the structure of interest owing to the easier identification of the flat sides.

4.7 Summary

A fully distributed optical fibre bend sensor based on a multi-core D-shaped fibre was demonstrated. BOTDR setup was used to measure diameters ranging from 59 mm to 227 mm with deviations between 9% and 15% depending on the diameter of the spool. The D-shaped geometry allows for the preferential bending of the fibre with the flat side either on the inner or on the outer side of the bend, offering a solution to the fibre twist issue that is a common issue when trying to do shape sensing. In this way, the need to manually inspect the orientation of the cores is eliminated rendering the use of this fibre in the field practical. In the next chapter, a MC fibre with both sides will be presented. This fibre offers an enhanced preference in bending owing to the two flat sides as well as an easier application to the structure of interest, thanks to the easier identification of the flat side.

Chapter 5

Curvature sensing based on a flat fibre

5.1 Introduction

A major advantage of the flat fibre is the stronger preferential bending compared to the D-shaped fibre, owing to the two flat sides. This renders it a better candidate for use in the field since it is easier to place it onto the structure under test, given that the flat side can be easily identified.

Although better suited for bending, a flat fibre presents significant practical challenges when it comes to its handling owing to its non-circular geometry that cannot be accommodated in a self-apparent way by the currently existing devices. In this work, various striping, cleaving and splicing techniques have been explored, based on widely available equipment. With this in mind, cleaving and splicing recipes were developed and optimised using commercially available and portable splicer and cleaver units, rendering the handling of this fibre feasible even in the field.

In section 5.2, the various ways for cleaving the flat fibre are analytically described. The technique for performing splices between a flat and a circular fibre as well as between two flat fibres, are presented in sections 5.3 and 5.4 respectively. In section 5.5 results from a three-point beam test are presented and in the final section the conclusions are summarised.

5.2 Fibre preparation

A fibre with a rectangular cladding presents an extra difficulty with its handling, since all the fibre tools, and devices are optimised for circular symmetric fibres. Many different techniques had to be developed in order to achieve an adequate cleave and connection of this fibre to circular fibres. This section will give an overview of the methods used and the results achieved.

The common mechanical stripping tools cannot be used for fibres with a cladding diameter larger than 250μm fibre. Some ways of stripping these type of fibres include the use of a razor blade, or a variant of chemical cleaving. In this last technique, the fibre coating can be briefly soaked in a solvent like acetone until it softens and swells, thus facilitating the peeling off of the coating [109].

The simplest and most straightforward way to experiment with cleaving the flat fibre was by using a ceramic cleaver. In this technique the fibre is first scored and then gentle pressure is applied with a finger for the glass to break in a smooth

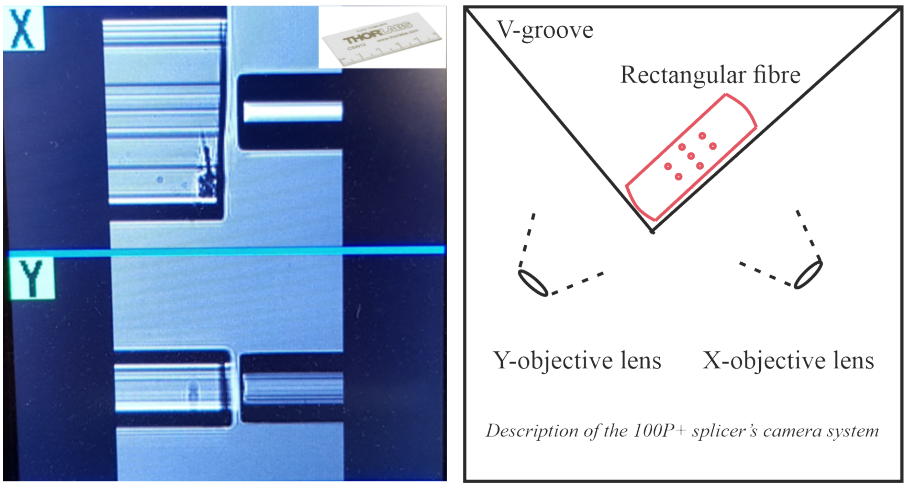

FIGURE 5.1: Left: View of the rectangular fibre (left side of the image) through the splicer's imaging system. The cleave was done using the ceramic cleaver shown in the inset. The estimation of the cleave angle, 6.6°, is based on an algorithm using images from both cameras (Picture on the right).

manner along the stress lines created by the scratch. To inspect the quality and the angle of the cleave, a 100P+ Fujikura fusion splicer was used, that implements its own algorithm in conjunction with its camera imaging system to analyse the cleave angle. Fig. 5.1 shows the splicer's camera images of the flat fibre as well as an estimation of the cleave angle. One disadvantage of performing a manual cleave is the difficulty in achieving repeatable results.

To improve the cleave, manual polishing of the fibre was attempted. This process involves rubbing the fibre against diamond films with different grit sizes in order to get rid of any protruding fibre as well as to smooth the surface of the fibre. To secure the fibre inside the FC/APC connector, and to ensure that the bond would be temporary, high temperature quartz wax was used. The wax application was achieved by heating the wax using a hot plate. After the polishing was complete, the heating process was repeated in order to remove the wax from the connector.

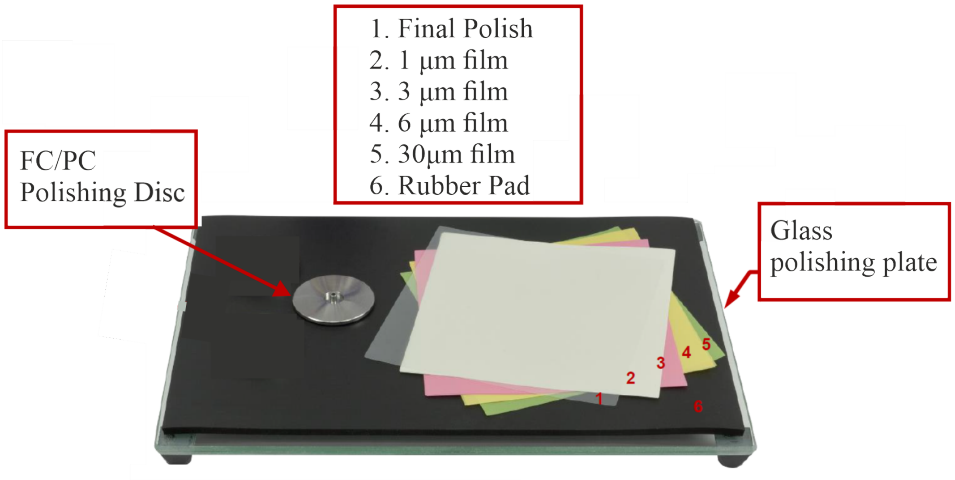

FIGURE 5.2: Manual optical fibre polishing equipment

Fig. 5.2 shows the equipment used for performing the manual polishing of the fibre. Fig.(a), (b) show that the polishing angle can be reduced by 0.9° in the case of a successful polish, however the result may worsen after the polish, as shown in Fig. 5.3(c), (d) if excess force is applied. Overall the polishing process is time-consuming and not only it needs a lot of practice to master, but also requires an adequate cleave as a starting point. This can be proven to be quite challenging in the case of a fibre diameter that is significantly larger than the standard one.

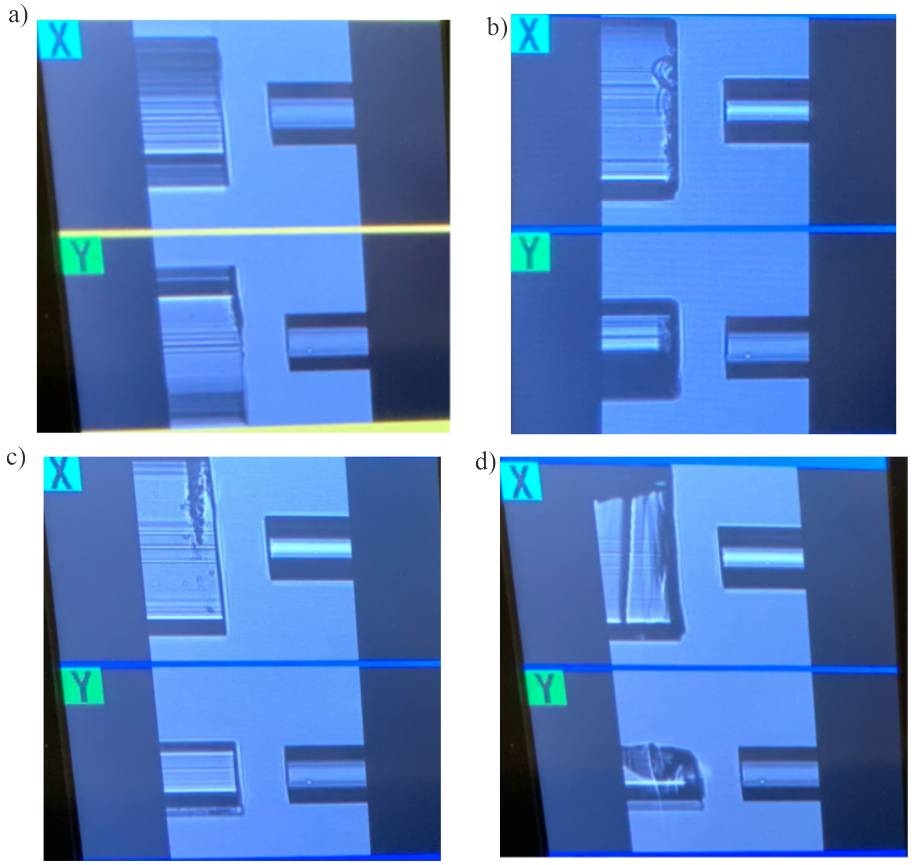

FIGURE 5.3: Cleave angle a) before polishing, 1.8°, b) after polishing, 0.9°, c) before polishing, 1.7° d) after polishing, 8.6°.

In order to overcome the inconsistency issues associated with the manual cleaving, the option of using a Fujikura CT-106 cleaver for large diameter fibres was explored. This type of cleaver uses a pulsation method for the blade to gently score the fibre and apply tension simultaneously. It also offers the choice to control the cleaving parameters, such as the blade speed, the clamping force or the cleave tension in order to achieve the ideal cleave. A lot of trials were performed in order to come down to a cleaving recipe for the large diameter flat fibre with the focus being mainly on the optimisation of the cleaving tension and clamping force. It is noted that this machine is not designed to be used for non-circular fibres so there was no guarantee that an adequate cleave could be achieved. However, after optimising the cleaving parameters, consistent and repeatable results were reached. The parameters used for achieving a cleaving angle of 0.1°, Fig. 5.5 (a) with a CT-106 cleaver

were: clamping force: 2050 gf for both right and left clamps, cleave tension: 575 gf, blade speed: 2800 μ/s. It is worth mentioning that Fujikura CT-106 cleaver is designed for $> 1^{\circ}$ cleaving angles.

5.3 Flat fibre to circular fibre splice

After optimising the recipe for the flat-fibre cleave, butt-coupling the fibre using the high precision stages of the 100P^{+} fusion splicer was attempted. However even the smallest vibrations can affect the strength of the Brillouin signal rendering the method inadequate for performing the shape sensing test. So the option of splice was the only way forward.

A 100P^{+} Fujikura splicer is a highly specialised piece of equipment that is loaded with various recipes for splicing the common type of fibres. It also offers the user the choice to manually control the alignment of the fibre with respect to the rotation angle theta as well as with respect to the X and Y-axis. Given that the attempted splice had never been explored before, a fully manual control of the process was chosen.

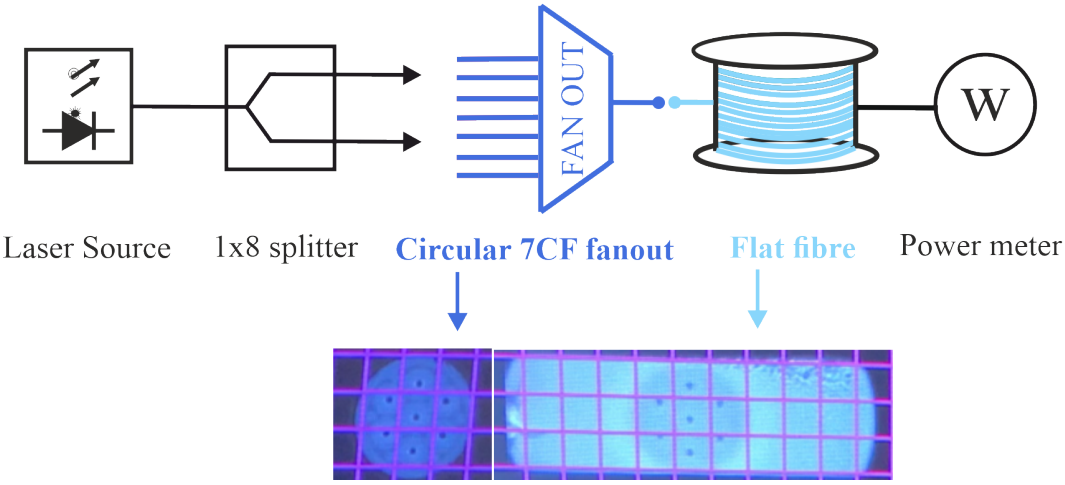

FIGURE 5.4: Setup for the active flat-to-circular fibre splice.

A first alignment with respect to the θ angle was performed using the grid lines of the splicer's imaging system as a guide. After that, and in order to achieve a precise alignment in the X and Y direction, an active alignment was performed using a setup that is shown in Fig. 5.4. Light from a 1550 nm laser source was injected into the fibre to be spliced and the output was sent via a 1 x 8 splitter into the standard 7CF fanout. Movement of the fibres in the X and Y plane was performed to maximise the power measured in the power meter connected to the flat fibre end. Fig. 5.5 (b) shows an image of the interface between the two fused fibres. The estimated loss was 0.17dB.

However it turned out that due to the $0.5-1\mu$m mismatch between the standard 7CF and the rectangular fibre, the route of splice had to be abandoned and a custom-made rectangular fibre fanout was ordered from Chiral Photonics. The fabrication

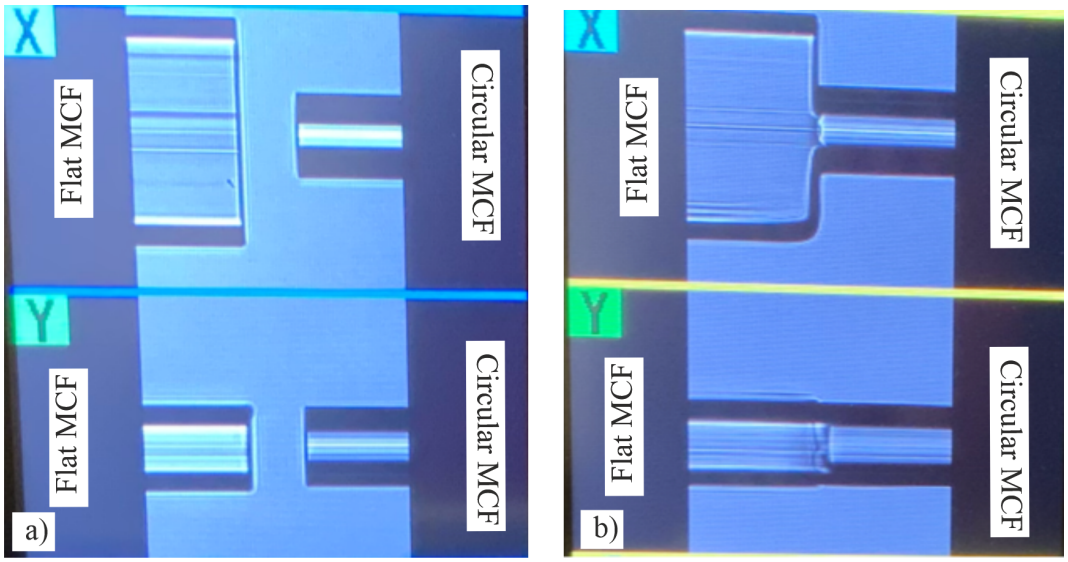

FIGURE 5.5: a) Cleave angle of the flat fibre 0.1° achieved by a CT-106 cleaver b) Splice loss of 0.17dB achieved by using a 100P+ fusion splicer.

process of this type of fanout is described in Section 2.3.2. The average insertion losses of the flat fibre fanout were 4dB prior to connectorisation.

5.4 Flat fibre to flat fibre splice

An 100P+ splicer was also used for this type of splice. For placing the fibre inside the splicer, the standard V-groove 400μm Fujikura holders were used and the fibre was positioned with the configuration seen in Fig. 5.6 (a) so as for uniform heating to be achieved. It is noted that it is very tricky to force the fibre to rest in the V-groove holder with a certain configuration, since its unique geometry creates a natural tendency for the fibre to rest with the flat side parallel to the surface of interest. Despite overcoming the challenge of placing the fibre into the splicer with any one of the two orientations shown in Fig. 5.6 (a), the splicer was prompting various error messages due to the inability of its motorised imaging system to focus properly on the fibre. As with most splicers and cleavers, this machine is optimised for circular symmetric fibres so any deviation from this geometry requires a lot of trial and error and a compromise for the final result that can pragmatically be achieved.

As a workaround, the fibre was placed with its flat side laying on the one side of the V-groove, as seen in Fig. 5.6 (b). The disadvantage of this configuration is the non uniform heating of the fibre due to the fact that one side is always closer to the electrodes compared to the other, as it can be seen in Fig. 5.6 (c). However, given the limitations in the degrees of freedom of movement of the electrodes and the fibre holders, the splicing process was optimised in view of these restrictions.

A fully manual, active splicing was performed and the two fibres were first aligned with respect to the θ angle, using the grid lines of the splicer's imaging system as

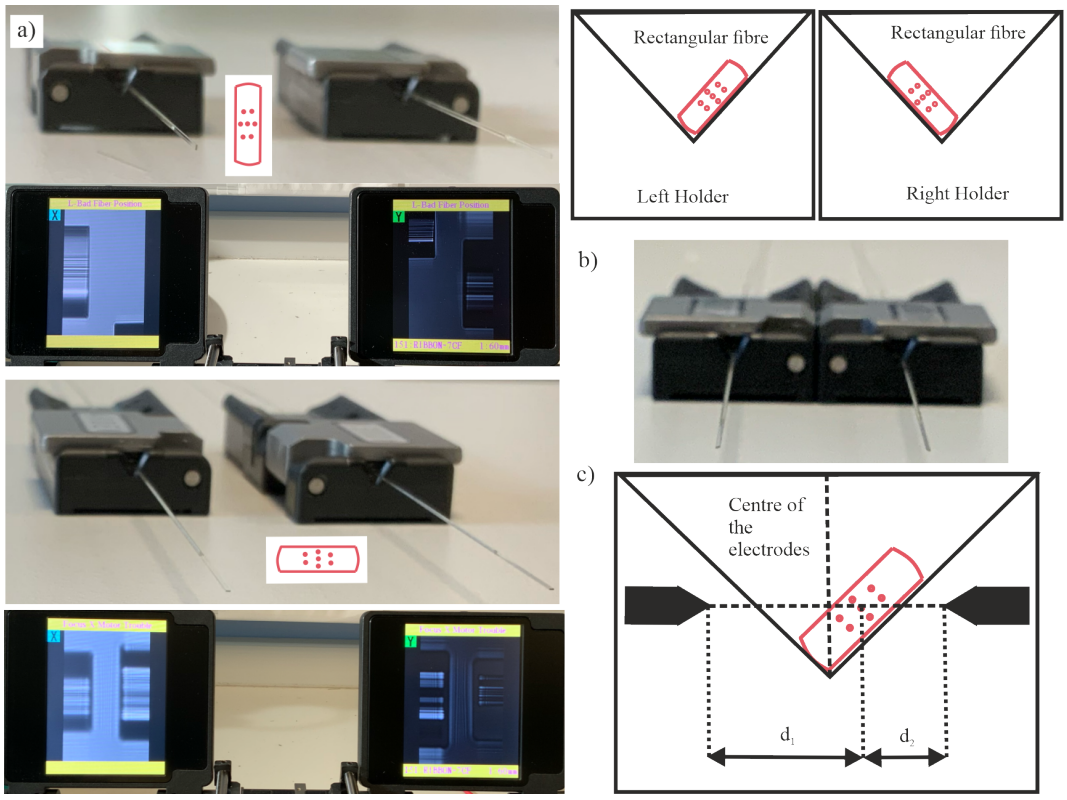

FIGURE 5.6: a) Possible resting position for the uniform heating of the flat fibre. b) Placement of the flat fibre in the splicer's holders to perform the splice c) Resting position of the fibre relative to the electrodes. The right side of the fibre is being heated more compared to the right due to its closeness to the electrode.

a guide. After that, and in order to achieve a precise alignment in the X and Y direction, an active alignment was performed using a setup that is shown in Fig. 5.7. Light was injected by a 1550nm laser source and it was sent via a 1 x 8 splitter into the standard 7CF fanout. Precise alignment of the fibres in the X and Y plane was performed to maximise the power measured in the power meter connected to the flat fibre end.

The splice achieved is shown in Fig. 5.7. Due to the non-uniform heating owing to the non-symmetrical way the fibre sits on the holders relative to the electrodes, an inadequate joint is formed in the upper part of the cladding area. However since this is far from the core region, where the splice looks visually better, it should not affect the overall quality and splice performance.

5.5 Three-point bending test

A major advantage of the flat fibre is the stronger preferential bending compared to the D-shaped fibre, owing to the two flat sides. Also it is easier to deploy it onto the structure under test since the flat side can be easily identified. Measuring bending radii in the range of 1m in the lab is desirable before deploying the fibre into the field. To simulate such big bends a simple setup emulating a three point bending

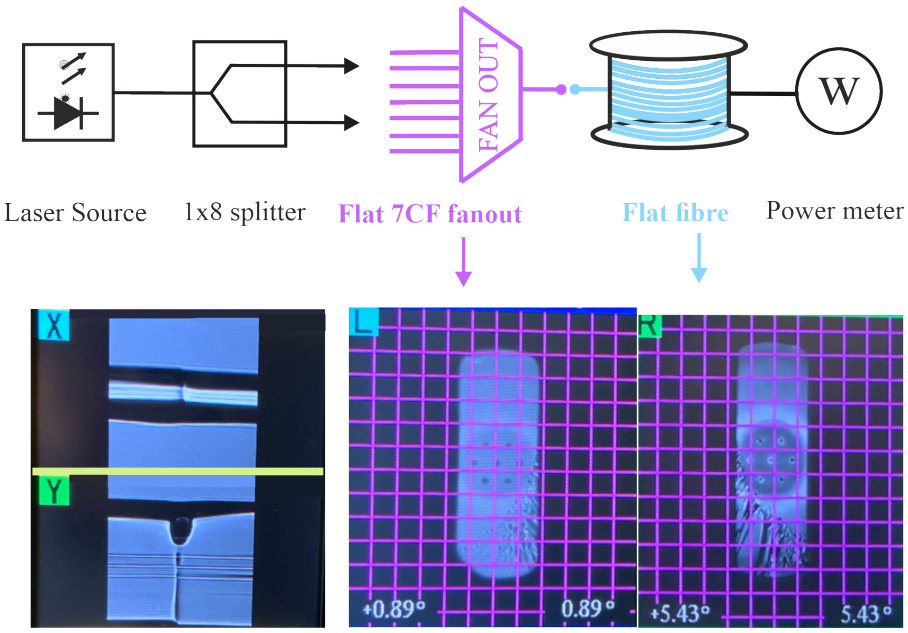

FIGURE 5.7: Setup for the active flat-to-flat fibre splice. Image of the spliced interface between the two flat fibres.

test was created in the lab. The three point bending test is a classical experiment in mechanics. It represents a beam resting on two roller supports that is subjected to a concentrated load applied in the middle of the beam.

In this section a first attempt to perform curvature sensing deploying the flat multi-core fibre on an aluminium flat surface is presented. A mock-up of a three-point bending system is used as the experimental setup in the lab. One alternative way of performing this measurement could be with the use of two single core fibres, one on top and the other on the bottom of the aluminium beam. However, in this case the issue of correlating one single location within the two fibres arises, due to the fact that the two fibres will not present the same length due to bending. This effect is diminished with the use of a MCF where similar strain, temperature and length conditions are secured owing to the position of the cores into the same cladding.

The lab-based setup, consisting of an aluminium flat beam and three stands used as the three point fixtures, is shown in Fig. 5.8 (a). The two fixtures that support the beam allow it to roll while bending and the central one is used for applying the load.

As a first approximation for the calculation of the bending radius for the points along the beam the deflection curve is considered as an arc of a circle. Fig. 5.8 (b) shows a simplified schematic for the calculation of the bending radius of the beam. The displacement of the beam by distance w is equivalent to a bending radius R. It is easily shown that for an angle θ,

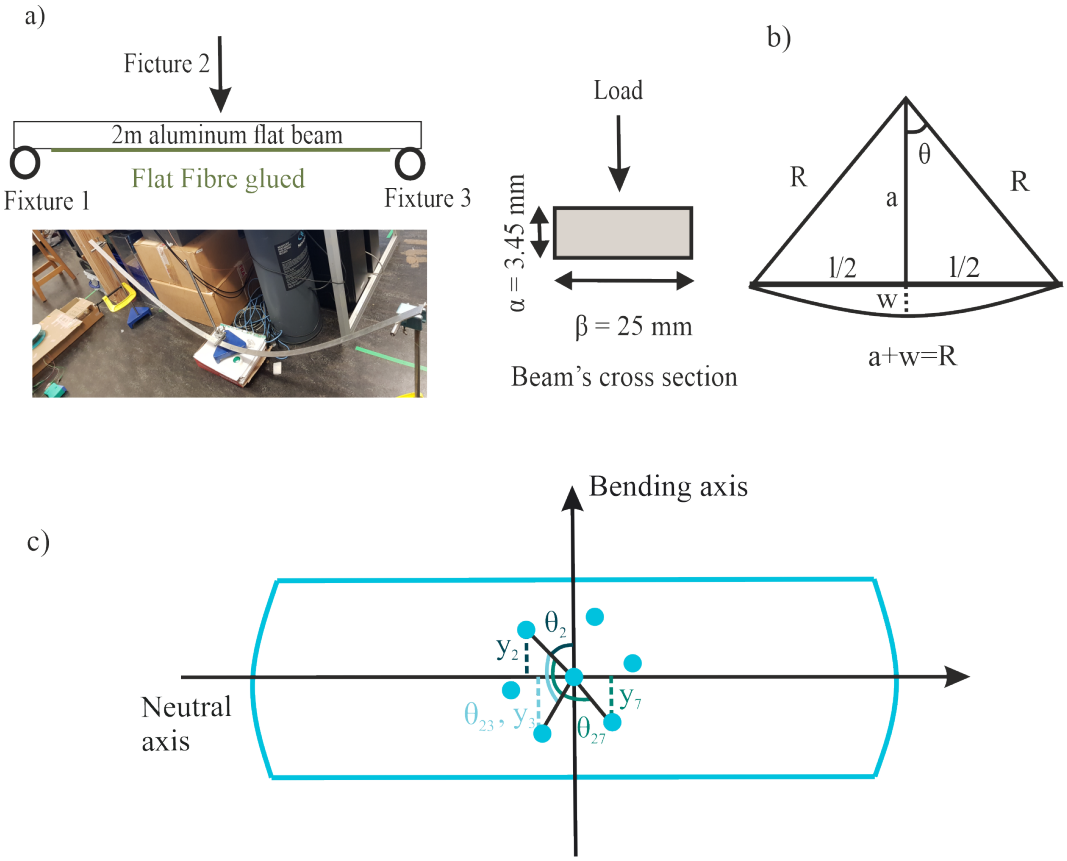

FIGURE 5.8: (a) Schematic of the three-point beam test, and image of the experimental setup in the lab. Dimensions of the beam's cross section. (b) Simplified schematic for the calculation of the bending radius of the beam represented as an arc length. (c) Schematic of the flat fibre and the coordinate system used for the curvature measurement. The cores' layout has been rotated by an arbitrary angle for illustrative purposes.

$$\cos\theta = \frac{R - w}{R} \tag{5.1}$$

$$\sin\theta = \frac{L}{2R} \tag{5.2}$$

where L is the length of the beam. By using the trigonometric identity $\cos^2\theta + \sin^2\theta = 1$ and solving with respect to R the formula that gives the bending radius of the beam can be expressed as,

$$R\,(\mathrm{m}) = \frac{1 + w^2\,(\mathrm{m})}{2\,w\,(\mathrm{m})} \tag{5.3}$$

where R is the bending radius of the beam and w is the vertical displacement of the beam from its straight position.

The geometric model is a good approximation for the central point of the beam

and for small deflections since it assumes that all the points along the beam experience the same bending radius. However in reality, the intermediate point of the beam is under larger deflection compared to the points at the edge of the beam and so a smaller bending radius is expected for the central point compared to the points at the edge of the beam. To accurately predict the bending radius along the whole length of the structure, beam theory equations for calculating the bending radius as a function of the distance from the mid-point have to be used.

The equation that gives the bending radius R as a function of the bending moment M along the points of the beam, is originated by engineers beam theory [110]:

$$R(x) = \frac{EI}{M(x)} \tag{5.4}$$

The three-beam test is equivalent to a simple supported beam with a central load. For this case, the bending moment M is given as a function of the distance along the length of the beam by the formula $M = Fx/2$. As a result Eq. (5.4) becomes [111],

$$R(x) = \frac{2EI}{F}\frac{1}{x} \tag{5.5}$$

where E is aluminium's elastic Young modulus equal to 70GPa, I is the area moment of inertia that is calculated for the axis that is perpendicular to the applied loading, and F is the load that is applied to the beam. The elastic Young modulus is a measure of the resistance of a material to elastic deformation under load. The larger the Young modulus, the stiffer a material is.

The area moment of inertia is a geometrical property of an area which reflects how its points are distributed with regard to an arbitrary axis. The area moment of inertia along the β-axis for the rectangular cross section with dimensions shown in Fig. 5.8 is given by,

$$I = \frac{\beta\alpha^3}{12}. \tag{5.6}$$

The load F can be computed by the equation giving the displacement at the middle point of a simply supported beam with a concentrated load in the middle [111],

$$F = \frac{w_{L/2}48EI}{L^3} \tag{5.7}$$

where $w_{L/2}$ is the displacement at the middle point of the beam, and $L = 1.9$m is the total length of the beam.

The dependence of bending radius on the position along the length of the beam is shown in Fig. 5.9 for the case of the aluminium beam with a cross section $\alpha\beta$ used for this test. The x-axis represents the distance from one support fixture until the mid-point of the beam. The figure shows that the bending radius tends to infinity for $x = 0$ as is predicted by Eq. (5.5). This is expected, since the beam is free to roll on the support and therefore this point experiences almost no bend (bending radius tends to infinity). Eq. (5.5) gives a bending radius of 1m for the mid-point of the beam. The geometric calculation gives 1.8m because as explained above it considers a uniform bending radius along the whole length of the beam.

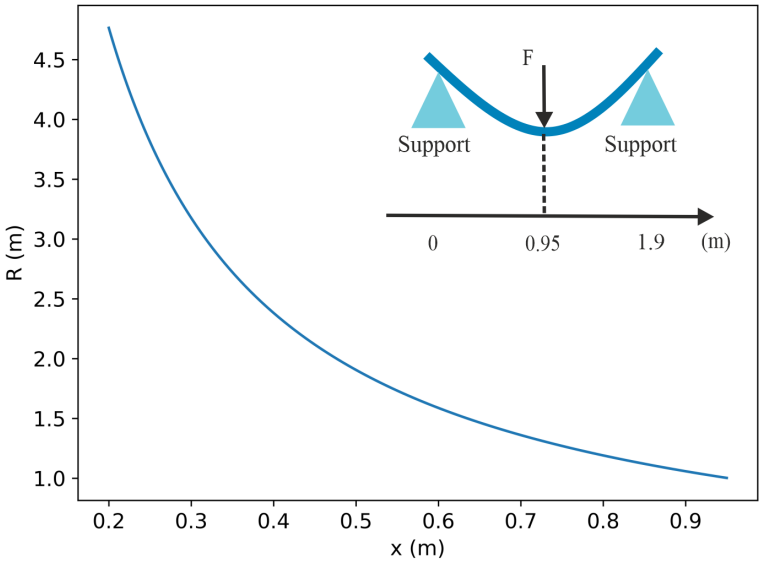

FIGURE 5.9: Plot of the theoretical relationship between bending radius and distance along the beam, Eq. (5.4). The bending radius varies as a function of the distance of the centre, increasing for the points closer to the edge of the beam. At the intermediate point of the beam (0.9m), where a load corresponding to a 30cm displacement has been applied, the bending radius is slightly above 1m.

To perform curvature sensing, two cores provide sufficient information and so the central and an outer one can be used. Below, the process for calculating the bending radius from the frequency shift data of two cores, is presented.

The Brillouin frequency shift has a linear dependence on strain and temperature according to the relationship,

$$\frac{df_B}{f_B} = C_s\, d\epsilon + C_T\, dT \tag{5.8}$$

where C_s is the strain coefficient of the normalised Brillouin frequency shift and C_T is the temperature coefficient. The differentials df, $d\epsilon$ and dT are of the frequency, strain and temperature respectively.
By integrating Eq. (5.8) [112]:

$$\int_{f_{B,\epsilon_0}}^{f_{B,\epsilon_i}} \frac{df_B}{f_B} = C_s \int_{\epsilon_0}^{\epsilon_i} d\epsilon + C_T \int_{T_0}^{T} dT \tag{5.9}$$

$$\ln\left[\frac{f_{B,\epsilon_i}}{f_{B,\epsilon_0}}\right] = C_s\ (\epsilon_i - \epsilon_0) + C_T\ (T - T_0) \tag{5.10}$$

$$\epsilon^{\text{meas}} = \ln\left[\frac{f_{B,\epsilon_i}}{f_{B,\epsilon_0}}\right] = C_s\ \epsilon_i \tag{5.11}$$

where f_{B,ϵ_i} ,ϵ_i and T_i are the frequency shift, strain and temperature respectively of the i-core and f_{B,ϵ_0}, ϵ_i, T_0 are the frequency shift, strain and temperature at the reference core. If the central core is used as reference, then $\epsilon_0 = 0$ because the central core is located at the neutral axis along which the strain is zero and all the cores have the same temperature as the central given that they are all located at the same cladding, $T_i = T_0$.

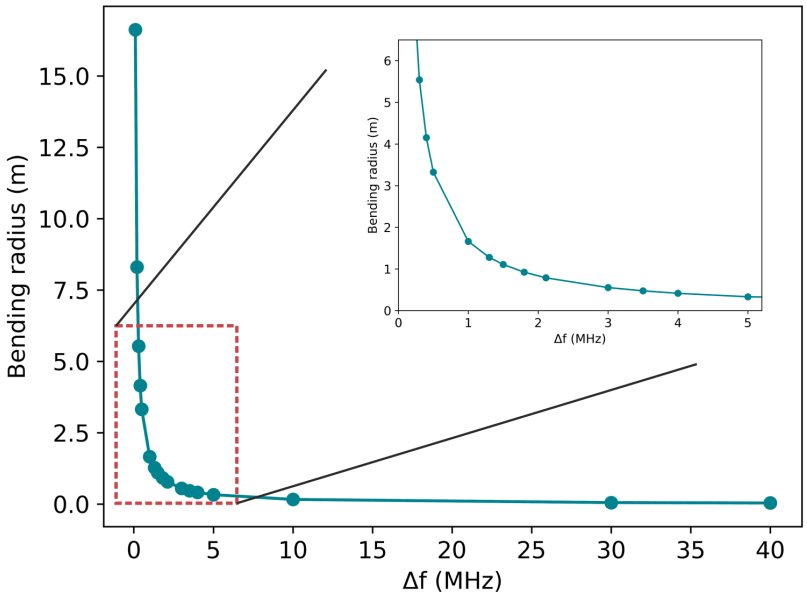

FIGURE 5.10: The relation between the frequency shift and bending radius for $C_s = 4.6$ and $f_{\text{central}} = 10.3248$GHz. Zoom-in for the region $\Delta f < 5$MHZ.

The distance of the i-core from the neutral axis y_i, can now be expressed as a function of the angle between the bending axis and the i-core Fig. 5.8 (c) as follows:

$$\epsilon_i(s) = -\kappa(s)\ y_i(s) = -\kappa(s)\ r_i\ \cos\theta_i(s) \tag{5.12}$$

where r_i is the radial distance from the centre of the fibre cross section to the location of the i-core. More specifically the relations for the strain ϵ_2 and ϵ_7 of the diametrically opposed cores 2 and 7 can be written,

$$\epsilon_2(s) = -\kappa(s)\ r_2\ \cos\theta_2(s) \tag{5.13}$$

$$\epsilon_7(s) = -\kappa(s)\ r_7\ \cos\left[\theta_2(s) + \theta_{27}(s)\right] \tag{5.14}$$

Assuming that $\theta_2 = 0$ and $\theta_{27} = \theta_2 + \pi$ and $r_2 = r_3 = r_7 = r = 35\ \mu$m and by combining Eq. (5.11) with Eqs. (5.13)-(5.16) the measured strain can be written as,

$$\epsilon_2^{\text{meas}}(s) = \ln\left[\frac{f_{B,\epsilon_2}}{f_{B,\epsilon_0}}\right] = -\kappa(s)\ r\ C_s \tag{5.15}$$

$$\epsilon_7^{\text{meas}}(s) = \ln\left[\frac{f_{B,\epsilon_7}}{f_{B,\epsilon_0}}\right] = \kappa(s)\ r\ C_s \tag{5.16}$$

$$R_2 = \left|\frac{-C_s r}{\ln\left(\frac{f_{B,2}}{f_{B,\text{central}}}\right)}\right| \tag{5.17}$$

$$R_7 = \left|\frac{-C_s r}{\ln\left(\frac{f_{B,7}}{f_{B,\text{central}}}\right)}\right| \tag{5.18}$$

where $\Delta f = f_{\text{outer}} - f_{\text{central}}$ is the difference in the frequency shifts between the central and one outer core.
A general expression for the bending radius as a function of the frequency shift difference can be given by,

$$R = \left|\frac{-C_s r}{\ln\left(\frac{\Delta f + f_{B,\text{central}}}{f_{B,\text{central}}}\right)}\right| \tag{5.19}$$

The plot relating the frequency shift difference Δf to the bending radius shows that this curve is almost linear for frequency shifts $\Delta f > 10$MHz, while it decays exponentially for $\Delta f < 5$ MHZ, as shown in Fig. 5.10.

For the three-beam test performed, ~ 1.8m length of the flat MCF was glued at the bottom of the aluminium beam and the central point of the beam was displaced by 30cm. The total length of the sensing fibre is 94m. A short length of the sensing fibre ~ 3m was left free at the end beam for the points of interest to be away from any reflection points at the end of the fibre that could distort the measurements. The other end of the fibre is wrapped around a bobbin. The beam was displaced by 30cm to allow a bending radius in the order of 1m to be studied. This deflection apart from causing a bending radius in the desired step of interest for applications such as sub-sea cables, is also in the safe side in regards to causing any breakage in the fibre.

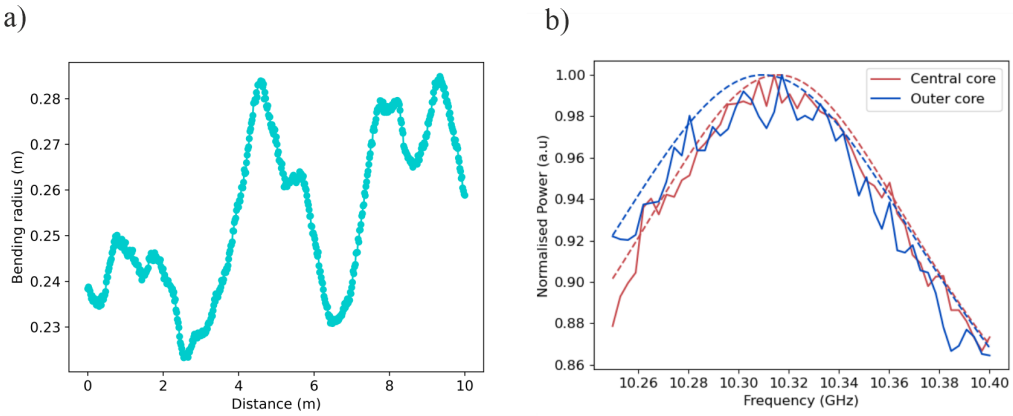

FIGURE 5.11: a) Bending radius as a function of distance for the last 10m of the sensing fibre. b) Lorentzian fits for the central and the outer core for a location corresponding to 4.59m.

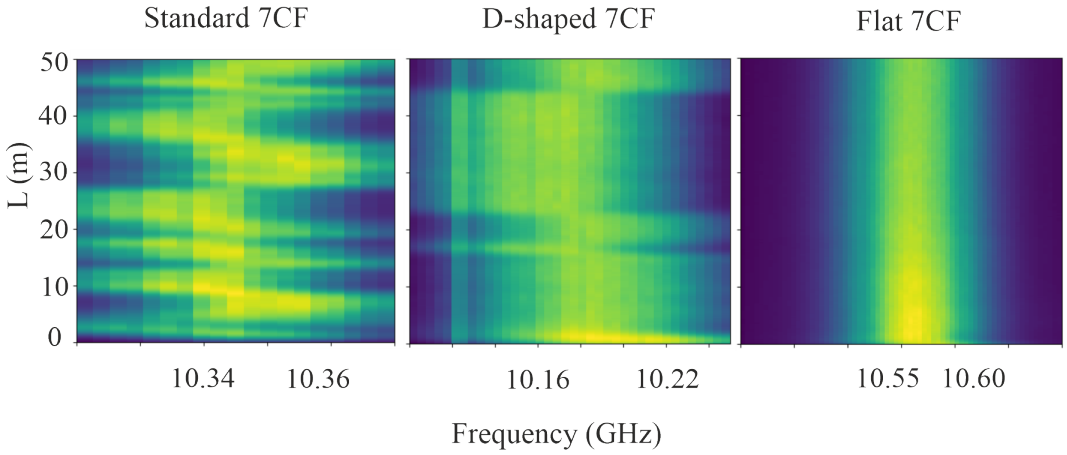

FIGURE 5.12: BGS of an outer core for the case of a standard, D-shaped and flat fibre.

In a first approximation it is assumed that the strain is not transferred through the glue, from the beam to the fibre and the fibre simply touches the beam following its curvature. In this case the assumption that the central core lies on the neutral axis is valid and Eq. (5.19) can be used for the bending radius calculation.

Figure 5.11 a), b) show the bending radius for the last 10m of the sensing system and the fitted Lorentzians for the location corresponding to 4.6m for the central and an outer core respectively. Brillouin OTDR spectra were acquired with $10,000$ averages and a scanning step of 3MHz.

From Eq. (5.19) it is shown that the frequency shifts expected for a bending radius of $\sim$ 1m is in the order of 2MHz. The experimental results show that the computed frequency shifts for the last 10m of the sensing fibre are between 5MHz and 8MHz corresponding to a maximum bending radius of ~ 0.28m.

The method used to calculate the bending radius described in this section assumes that all the points along the length of the beam experience the same bending radius. In reality, the points closer to the edge of the beam will experience higher bending radius compared to the mid point, since the beam is more flat towards its

edges. Further tests will follow to improve the measured curvatures: An acquisition with larger number of averages will contribute to the reduction of the noise seen in the Lorentzian fits. Decreasing the scanning range from 3MHz to $\sim$ 1MHz will also provide spectra with higher resolution leading to a more accurate determination of the peak. The use of a narrower bandwidth band pass filter (less than 50MHz that was currently used) could contribute to a narrower detected BGS linewidth rendering the determination of frequency shifts in the range of $\sim$ 1MHz less ambiguous.

Although further tests need to be performed aiming to the improvement in the determination of the bending radius, the flat multi-core fibre is proven a very promising candidate for use in shape sensing applications. Its unique geometry that greatly enhances the preferential bending eliminates the issue of twist, which is a common problem that comes with the multi-core fibres when used for shape sensing applications. The elimination of twist is depicted in the BGS of this unique fibre. Fig. 5.12 shows the BGS for an outer core for the case of a standard 7CF, the D-shaped 7CF and a flat 7CF wrapped around a spool. It is noted that the BGS of a standard 7CF presents notable fluctuations that reflect the random flips of the fibre as it is wrapped around the bobbin. In the case of the D-shaped 7CF there are fewer fluctuations within a 50m length and it can be clearly seen that the D -shaped fibre flips between two states (either the flat side sits on the inner side of the spool or on the outside). Finally, the flat 7CF shows no visible fluctuations proving that its asymmetric design enhances the preferential bending, rendering a promising candidate for long range curvature sensing.

5.6 Summary

In this chapter various methods for handling the flat fibre were described. A flat to circular as well as a flat to flat fibre splice were achieved with the use of commercial equipment designed for circular fibres. In the last part, curvature results of a three-point beam test were presented as a first attempt towards the real-field application of the fibre. BGS of the flat fibre showed noticeable uniformity confirming the elimination of twist, as predicted.

Chapter 6

Conclusion and Future Work

6.1 Summary

Optical fibre sensors offer many advantages in comparison to their conventional counterparts, such as immunity to external electro-magnetic fields and small dimensions. The multi-core fibres in particular are ideal candidates for shape sensing due to the intrinsic 3D coordinate system they offer. However the twist of the multi-core fibre associated to its wrapping around the structure of interest, results in a twist of the cores, which in turns distorts the 3D coordinate system based on their fixed position. This dissertation demonstrated ways to overcome this issue by designing and fabricating two multi-core fibres presenting enhanced bending preference.

As outlined in Chapter 4, a D-shaped fibre was designed and fabricated to address the issue of the fibre twist that was observed in the standard circular 7CF. Using Brillouin Optical Time-Domain Reflectometry which offers the advantage of large sensing range and measurement of absolute strains/temperatures, curvature tests on spools of different diameter were performed. The curvature measurements showed a good match with the theory. Although the Brillouin gain spectra associated with this fibre showed significant improvement of the twist issue compared to the standard 7CF, the flip of the fibre between two different states showed that this issue remains.

To completely address this, a new multi-core fibre with two flat sides was designed, to further enhance the fibre's bending direction. Brillouin gain spectra associated to this fibre showed no noticeable fluctuations for the whole length of the sensing fibre confirming the elimination of the fibre twist. To simulate the use of the fibre in a real field application, a three-beam setup was built in the lab. Tests for further improvement of the curvature measurements acquired using this setup are planned as a future work. Apart from resolving the twist issue, a flat multi-core fibre offers the advantage of an easy attachment to the structure of interest owing to the easy identification of the flat side.

Due to its unique geometry, cleaving and splicing of this fibre was not feasible using the conventional techniques and equipment. Hence, an extensive study of various methods for its handling was conducted and the developed techniques were presented in Chapter 5. Commercial cleaving and splicing equipment was used for the handling of the flat fibre such as a large diameter Fujikura CT − 106 and a 100P$^+$ splicer. Tolerable splices and cleaves were achieved to accommodate for

the needs of the flat multi-core fibre, within the restrictions accompanying devices that are designed and optimised for circular fibre. More specifically, the V-groove fibre holders although ideal for circularly symmetric fibres, didn't allow to the flat fibre to be placed in a symmetric way with respect to the electrodes to achieve uniform heating hence compromising the quality of the splice. One additional factor increasing the complexity of the task was the limited degree of freedom of motion of the electrodes and the holders as well as the inability of the motorised imaging system to focus properly on the fibre due to its geometry and size. Alternative ways for achieving splices and cleaves could be tested using a laser CO_2 cleaver and a Vytran splicer allowing a more customised way of handling the fibre.

An alternative method to fusion splicing for creating an interconnection between the flat fibre and another fibre could be achieved by applying a glue-based fibre-array technology currently used for creating interconnection between hollow core fibres and standard fibres [113]. This technique relies on gluing the fibres on an optical fibre array and then precisely aligning its end faces with the use of micropositioning stages. By applying a non-thermal technique, the risk of the deformation of the end face of the flat fibre due to heat is avoided during the gluing that involves far lower temperatures compared to the temperatures encountered in the fusion splicing techniques.

Future work also includes the optimisation of certain fabrication stages of the flat fibre such as polishing after grinding that could improve the strength of the fibre, minimising fractures. Also, the use of bespoke mounts would contribute to better grinding accuracy, improving the core positioning. The coating of this fibre requires the use of dies with a rectangular geometry. However due to challenges in the micromilling technology pertaining to the accuracy of machining of the corners, the edges of the coated fibre remain disproportionally coated compared to the rest of the fibre leading to increased fibre weakness. An alternative way of applying the coating would be via ultrasonic spraying techniques in order to ensure uniformity and avoid the need of custom made rectangular dies that come with the challenges in the corner shaping.

Another change to improve the sensitivity of the fibre as a curvature sensor could be achieved by increasing the core spacing. The bending-induced strain in an optical fibre is a continuous function that becomes zero for a core that lies on the neutral plane while it is linearly increasing with increasing distance from the neutral plane. Since there is a linear relationship between strain and distance from the neutral plane for a given bending radius, the sensitivity of the sensor increases when increasing the intercore distance. However, the right balance should be achieved between increasing the clad to core ratio to avoid mode leakage, sacrificing the strength of the fibre as well as its compatibility with regards to conventional splicing and cleaving equipment.

Although the rectangular fibre offers the advantage of an easy identification of the flat side, however its handling is more challenging compared to that of a circular

symmetric fibre. To get a similar preferred bending effect without losing the circular geometry, alternative designs could be investigated, where stress members could be added or empty holes could be created, to change the distribution of the mass in the fibre and hence controlling the amount of its bending. In this way the bending preference can be enhanced while a circular geometry is maintained.

To get the full potential of this promising technology the curvature sensing theory developed in this thesis could be extended to its fully 3D implementation, by developing and testing a shape reconstruction algorithm that could describe the shape of a multi-core fibre or a bundle of fibres in the 3D space. The algorithm is based on the Frenet Serret formulas that are a system of equations that express the kinematic properties of a particle moving along a continuous, differentiable, curve in the three-dimensional space. More specifically, they relate the tangent, normal and binormal unit vectors called $\mathbf{T}$ (unit vector tangent to the curve), $\mathbf{N}$ (unit vector normal to the curve), $\mathbf{B}$ (the cross product of $\mathbf{T}$ and $\mathbf{N}$) respectively, to the curvature κ and torsion τ of a curve in 3D space. Assuming that the initial conditions of the vectors $\mathbf{T}(0)$, $\mathbf{N}(0)$, $\mathbf{B}(0)$, $\mathbf{r}(0)$ -$\mathbf{r}$ is the position vector- are known at the starting point, and based on an iterative process, the algorithm allows the extraction of the shape of the fibre in the 3D space.

In the framework of this PhD thesis, an automatic data acquisition script was developed in Python for the averaging of thousands of data points and the post processing creation of the Brillouin Gain Spectra. A future update of the system could involve the use of an optical switch to allow the cores to be scanned one after the other automatically eliminating the need for manual selection of the cores in a sequential mode, resulting in a full automation of the system. Also, low level machine code could be used for faster communication with the digitizer or alternatively a PCI-e with streaming capabilities could be used to directly access the data on the PC without any delay.

Lastly, in order for any fibre to be deployed in the field where harsher conditions prevail, a use of a protective cable as an outer coating has to be considered. This coating needs to offer the possibility of strain transfer between the structure and the fibre. A study of different cables and their response to strain as well as to bending could be investigated, in order to render feasible the use of this fibre under harsher conditions, such as in radioactive or in underground excavated environments.

Appendix A

Data Acquisition Automation

The need for automating the data acquisition part of the research that is conducted in a lab, becomes more and more prominent, as the degree of complexity of an experiment increases. The use of software for controlling scientific instruments for data acquisition increases productivity and elevates experimental data quality since it improves the accuracy of the data collection. In this way reproducibility is secured. Also, the data processing time is reduced enabling experimentation that otherwise would be impossible.

The experiments conducted in the framework of this PhD project, involved the processing of thousands of data points averaged for thousands of times, a procedure that would be otherwise impossible without the development of an algorithm automating the data acquisition process. MATLAB, LabVIEW and Python are some of the popular choices for programming languages used in lab automation. Among those, Python was chosen because it has a large community of users, it is free, open, and hence transferable.

A flow-chart of the data acquisition algorithm used for capturing and processing the data, is shown in Fig. A.1. The computer controls the data acquisition via a Python [114] script.

To gain the strain information from every point along the sensing fibre a large number of averages need to be acquired in a wide range of frequencies. A frequency synthesiser is an electronic component used to generate a set of discrete frequencies and whose frequency stability is derived from either a built-in or an external crystal oscillator [104]. The MLSL-0911 Micro Lambda model used in this work, operates with a three-wire communication protocol. Since the PCs do not support such output ports, a micro-controller has to be mediated between the PC and the frequency synthesiser in order to transfer the data from the PC to the frequency synthesiser's input pins. An Arduino board was chosen as the micro-controller since the frequency synthesiser's manufacturer provided support for it. The section of the Python script referring to Arduino, sends the frequency to Arduino in ASCII format.

Arduino then sends the said frequency to the synthesiser and for this specific frequency the oscilloscope captures the data and transfers them to the PC. After the data of voltage, time and frequency are transferred to the PC, post processing begins. More specifically, Lorentzian curves are fitted into the voltage as a function of frequency data in order to accurately determine the frequency shift corresponding

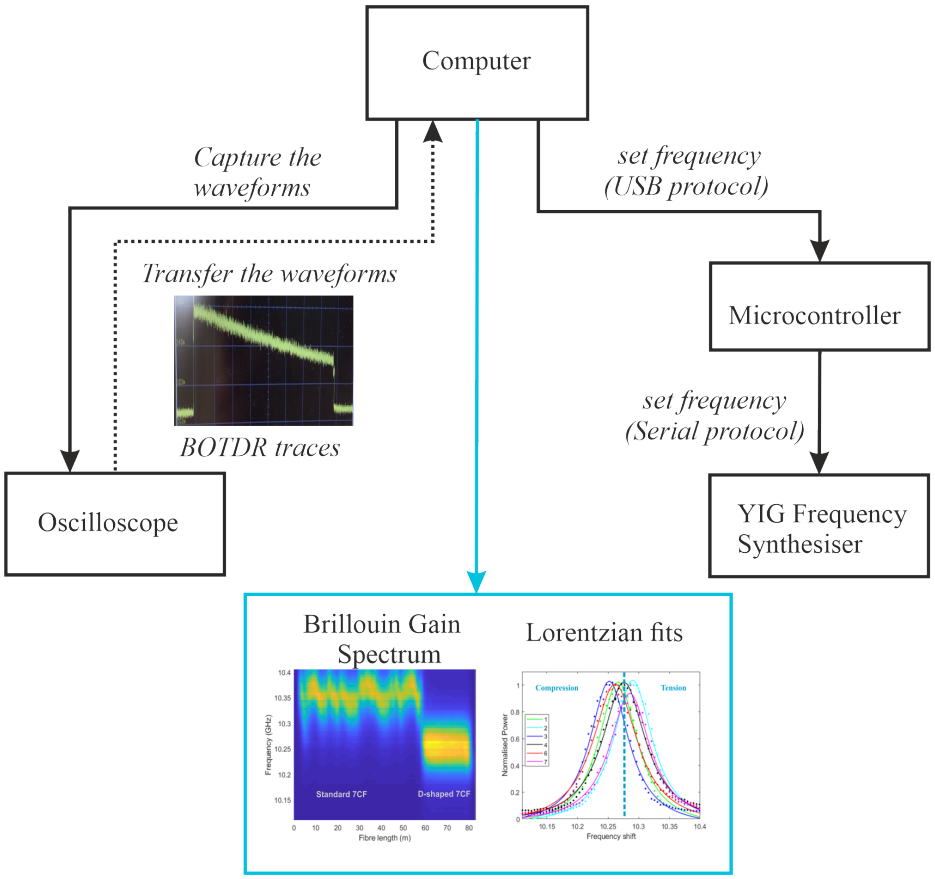

FIGURE A.1: The computer controls all the processes via a Python script. The desired frequencies are sent to the micro-controller (Arduino board) via a USB protocol and then the microcontroller sends those frequencies serially to the YIG synthesiser. The computer sends the necessary commands to the oscilloscope for it to capture the data and the waveforms are subsequently transferred to the PC. After post-processing, the 3D Brillouin spectrum as well as Lorentzian fits are produced.

to the peak of the Lorentzian needed to infer the strain and curvature at the specific position of the fibre.

A pseudo code for the the acquisition of the backscattered signal from every point along the fibre is described below: First, the communication between the PC and the programmable devices (Arduino and Oscilloscope) is initialised.

The acquisition and data transfer details for the acquisition of data from the oscilloscope are then set. Parameters like the number of averages, the number of points transferred, the period of the signal, or the channel of the scope from which the transfer of data occurs, are denoted in an initial section of the code. A Keysight, 5GSa/s, 350MHz bandwidth oscilloscope is used for the data acquisition. The communication between the PC and the oscilloscope is achieved with the use of SCPI (Standard Commands for Programmable Instruments)[115] which is a set of standard syntax that controls measurement devices such as oscilloscopes, signal generators, Optical Spectrum Analysers etc.

After the oscilloscope parameters have been set, the data capture loop begins. The frequency of the synthesiser is set and then the capture of waveforms and their transfer to the PC happens. The time and voltage data are saved into arrays.

In the post processing stage, 3D and 2D plots of the data are produced. Lorentzian fits are plotted for a specific location along the length of the fibre, to extract the frequency shifts corresponding to the peak of the Lorentzian. Those values are then used to calculate the strain and the curvature of to this particular position along the fibre.

Data Acquisition Pseudocode:

Initialise communication: Arduino, Oscilloscope
Set up oscilloscope parameters (SCPI commands)
- Time (i.e signal period)
- Capture channel (i.e range, impedance)
- Trigger channel (i.e level)
- Acquisition(i.e mode, no of averages, no of points)
- Data Transfer (i.e data format)

Data capture loop
- set synthesiser's frequency
- capture waveform from the oscilloscope
- transfer waveform to the PC
- save time, voltage data into arrays

Post Processing
- 3D Plot (BGS): Voltage = f (time, frequency)
- Lorentzian fit: Voltage = f (frequency)
- Extract frequency shifts (peak of the BGS)
- Translate frequency shifts to strain ϵ = f (frequency shift)
- Calculate bending radius from strain R = f (strain)

A future upgrade of the entire system could include the addition of an optical switch just before the fanout. In this way all the cores can be scanned one after the other without the need to do this change manually. This improvement could result in the system's fully automation.

List of Publications

Journal Publications

A. Zafeiropoulou, A. Masoudi, A. Zdagkas, L.Cooper, and G. Brambilla, "Curvature sensing with a D-shaped multicore fibre and Brillouin optical time-domain reflectometry," Opt. Express 28, 1291-1299 (2020)

Conference contibutions

(1) (Oral) **A. Zafeiropoulou**, A. Masoudi, L. Cooper, and G. Brambilla, "*D-shaped multicore fibre for distributed curvature sensing with BOTDR*," in Optical Sensors and Sensing Congress, OSA Technical Digest (Optical Society of America, 2020).

(2) (Poster) **A. Zafeiropoulou**, Ali Masoudi, Apostolos Zdagkas, Laurence Cooper, and Gilberto Brambilla, "*D-shaped multicore fibre and its application in curvature monitoring with Brillouin Optical Time-Domain Reflectometry*," in 27th International Conference on Optical Fiber Sensors, OSA Technical Digest (Optical Society of America, 2021).

(3) (Poster) **A. Zafeiropoulou**, A. Masoudi, L. Cooper, and G. Brambilla, "*Distributed shape sensing with a multicore fibre based on BOTDR technique*," in 26th International Conference on Optical Fiber Sensors, OSA Technical Digest (Optical Society of America, 2018), paper ThE15.

(4) (Tutorial) A. Masoudi, **A. Zafeiropoulou**, A. Donko, W. Talataisong, R. Ismaeel, M. Beresna, and G. Brambilla, "*New Approaches to Optical Fiber Sensing*," in CLEO Pacific Rim Conference 2018, OSA Technical Digest (Optical Society of America, 2018), paper F1E.1.

Workshops

(1) (Poster) **A. Zafeiropoulou**, A. Masoudi, L. Cooper, and G. Brambilla, "*Distributed shape sensing with a seven-core fibre based on BOTDR technique*,"Fibre Optic Shape and Deformation Sensing: An Emerging Technology, Institute of Physics, London UK (2019).

FINESSE Training Events

(1) (Poster) **A. Zafeiropoulou**, Morten Ibsen and Laurence Cooper, "*Design and Optimisation of Optical Fibres for 3D Shape Sensing Applications in Civil Engineering Structures*", PhD School on Fundamentals of Optical Sensors, Vrije Universiteit Brussel (VUB), Brussels, Belgium, June 2017

(2) (Video) **A. Zafeiropoulou**, "*History of Optical Fibre Sensors*",PhD School on Distributed Sensing Methods, University of Alcala, Alcala, Spain, September 2017

(3) (Oral) **A. Zafeiropoulou**, Ali Masoudi, Laurence Cooper, Gilberto Brambilla, "*Distributed shape sensing with a multicore fibre based on botdr technique*", PhD School on Speciality Fibres, Leibniz Institute of Photonic Technology (IPHT), Jena, Germany, April 2018

(4) (Oral) **A. Zafeiropoulou**, Ignazio Floris, Ravil Idrisov, "*SmartB, pitching activity on company deploying optical fibre sensors on bridges*", PhD School on Entrepreneurship in Photonics, CommScope, Leuven, Belgium, December 2018

(5) (Oral) **A. Zafeiropoulou**, Ali Masoudi, Laurence Cooper, Gilberto Brambilla, "*Distributed curvature sensing with 7-core fibre based on BOTDR*", Department of Engineering, University of Cambridge, UK, September 2019

Secondments

(1) (2-weeks secondment) "*OFDR technique with a multicore fibre*", THALES, France, April 2018

(2) (3-months secondment) "*Simulations of multicore fibres' bend in COMSOL and Lumerical.*", Brussels Photonics B-PHOT, Vrije Universiteit Brussel (VUB), Brussels, Belgium, November 2018-February 2019.

Bibliography

1. Mountassir, O. E. & Strang-Moran, C. Offshore Wind Subsea Power Cables, 6.
2. Rochat, E, Chin, S & Ravet, F. *Using Brillouin distributed sensing to reduce installation risk and optimize cable operation of subsea power cable* in (), 12.
3. Klug, F, Lackner, S & Lienhart, W. Monitoring of Railway Deformations using Distributed Fiber Optic Sensors. en, 8.
4. Mitschke, F. *Fiber Optics* (Springer Berlin Heidelberg, Berlin, Heidelberg, 2010).
5. Marcuse, D. Loss Analysis of Single-Mode Fiber Splices. *Bell System Technical Journal* **56,** 703–718. https://ieeexplore.ieee.org/document/6768444 (May 1977).
6. Senior, J. M. & Jamro, M. Y. *Optical fiber communications: principles and practice* 3rd ed (Financial Times/Prentice Hall, Harlow, England ; New York, 2009).
7. Inao, S., Sato, T., Sentsui, S., Kuroha, T. & Nishimura, Y. *Multicore optical fiber* in *Optical Fiber Communication* (Optical Society of America, 1979), WB1. http://www.osapublishing.org/abstract.cfm?URI=OFC-1979-WB1.
8. Richardson, D. J., Fini, J. M. & Nelson, L. E. Space-division multiplexing in optical fibres. *Nature Photonics* **7,** 354–362. http://www.nature.com/articles/nphoton.2013.94 (May 2013).
9. *Handbook of Optical Fibers* (ed Peng, G.-D.) http://link.springer.com/10.1007/978-981-10-7087-7 (Springer Singapore, Singapore, 2019).
10. Saitoh, K. & Matsuo, S. Multicore Fiber Technology. *Journal of Lightwave Technology* **34,** 55–66. http://ieeexplore.ieee.org/document/7214203/ (Jan. 2016).
11. Meltz, G. & Snitzer, E. *Fiber optic strain sensor* US Patent 4,295,738. 1981. https://www.google.com/patents/US4295738.
12. Gander, M. J. *Bend measurement using Bragg gratings in multicore fibre* in *Fourteenth International Conference on Optical Fiber Sensors* (eds Mignani, A. G. & Lefèvre, H. C.) **4185** (SPIE, 2000), 535 –538. https://doi.org/10.1117/12.2302270.

13. Villatoro, J. *et al.* Ultrasensitive vector bending sensor based on multicore optical fiber. *Opt. Lett.* **41,** 832–835. http://ol.osa.org/abstract.cfm?URI=ol-41-4-832 (2016).

14. Childlers, B., Gifford, D., Duncan, R., Raum, M. & Vercellino, M. *Fiber optic position and shape sensing device and method relating thereto* US Patent App. 11/180,389. 2006. https://www.google.com.pg/patents/US20060013523.

15. Villatoro, J., Arrizabalaga, O., Antonio-Lopez, E., Zubia, J. & de Ocáriz, I. S. *Multicore Fiber Sensors* in *Optical Fiber Communication Conference* (OSA, Los Angeles, California, 2017), Th3H.1. https://www.osapublishing.org/abstract.cfm?URI=OFC-2017-Th3H.1.

16. Zhao, Z., Tang, M., Lu, C., 1.Photonics Research Centre, Department of Electronic and Information Engineering, The Hong Kong Polytechnic University, Kowloon, Hong Kong & 2.National Engineering Laboratory of Next Generation Internet Access Networks, School of Optical and Electronic Information, Huazhong University of Science and Technology, Wuhan 430074, China. Distributed multicore fiber sensors. *Opto-Electronic Advances* **3,** 19002401–19002417. http://www.oejournal.org/J/OEA/Article/Details/A200222000010 (2020).

17. Cooper, L. J. *et al. Design and performance of multicore fiber optimized towards communications and sensing applications* in (eds Jiang, S. & Digonnet, M. J. F.) (San Francisco, California, United States, Apr. 2015), 93590H. http://proceedings.spiedigitallibrary.org/proceeding.aspx?doi=10.1117/12.2076950.

18. Moore, J. P. & Rogge, M. D. Shape sensing using multi-core fiber optic cable and parametric curve solutions. *Optics Express* **20,** 2967–2973 (Jan. 2012).

19. Zhao, Z., Soto, M. A., Tang, M. & Thévenaz, L. Distributed shape sensing using Brillouin scattering in multi-core fibers. *Optics Express* **24,** 25211–25223 (Oct. 2016).

20. Saridis, G. M., Alexandropoulos, D., Zervas, G. & Simeonidou, D. Survey and Evaluation of Space Division Multiplexing: From Technologies to Optical Networks. *IEEE Communications Surveys & Tutorials* **17,** 2136–2156. http://ieeexplore.ieee.org/document/7214205/ (2015).

21. Choudhury, D., Macdonald, J. R. & Kar, A. K. Ultrafast laser inscription: perspectives on future integrated applications: Ultrafast laser inscription: perspectives on future integrated applications. *Laser & Photonics Reviews* **8,** 827–846. http://doi.wiley.com/10.1002/lpor.201300195 (Nov. 2014).

22. Thomson, R. R. *et al.* Ultrafast-laser inscription of a three dimensional fan-out device for multicore fiber coupling applications, 7 (2007).

23. Thomson, R. R. *Ultrafast laser inscription of 3D components for spatial multiplexing* in (eds Li, G. & Zhou, X.) (San Francisco, California, United States, Feb. 2016), 97740O. http://proceedings.spiedigitallibrary.org/proceeding.aspx?doi=10.1117/12.2210883.

24. Thomson, R. R. *et al.* Ultrafast laser inscription of a 121-waveguide fan-out for astrophotonics. *Optics Letters* **37,** 2331. https://www.osapublishing.org/abstract.cfm?URI=ol-37-12-2331 (June 2012).

25. Mitchell, P., Brown, G., Thomson, R., Psaila, N. & Kar, A. 57 Channel (19x3) Spatial Multiplexer Fabricated using Direct Laser Inscription, 3 (2014).

26. Riesen, N., Gross, S., Love, J. D., Sasaki, Y. & Withford, M. J. Monolithic mode-selective few-mode multicore fiber multiplexers. *Scientific Reports* **7,** 6971. http://www.nature.com/articles/s41598-017-06561-w (Dec. 2017).

27. Kopp, V. I. *et al. Pitch Reducing Optical Fiber Array and multicore fiber for space-division multiplexing* in *2013 IEEE Photonics Society Summer Topical Meeting Series* (IEEE, Waikoloa, HI, USA, July 2013), 99–100. http://ieeexplore.ieee.org/document/6614505/.

28. Ismaeel, R., Lee, T., Ding, M., Belal, M. & Brambilla, G. Optical microfiber passive components: Microfiber components. *Laser & Photonics Reviews* **7,** 350–384. http://doi.wiley.com/10.1002/lpor.201200024 (May 2013).

29. Zhang, X. *et al.* In-fiber integrated optics: an emerging photonics integration technology [Invited]. *CHINESE OPTICS LETTERS,* 8 (2018).

30. Kopp, V. I. *et al.* Chiral Fibers: Microformed Optical Waveguides for Polarization Control, Sensing, Coupling, Amplification, and Switching. *Journal of Lightwave Technology* **32,** 9 (2014).

31. Senior, J. M. *Optical Fiber Communications: Principles and Practice* ISBN: 9788131732663. https://books.google.co.uk/books?id=ok0XX-3MgMoC (Pearson Education, 2009).

32. Hartog, A. *An Introduction to Distributed Optical Fibre Sensors* (Taylor & Francis Group, 2018).

33. MacChesney, J. B., Bise, R. & Méndez, A. in *Specialty Optical Fibers Handbook* (eds Méndez, A. & Morse, T. F.) 69–94 (Academic Press, Burlington, Jan. 2007).

34. Yariv, A., Yariv, P., Yeh, P. & Yeh, P. *Optical Waves in Crystals: Propagation and Control of Laser Radiation* (Wiley, 1984).

35. Zemansky, M. *Heat and Thermodynamics* (1968).

36. Maughan, S. M. *Distributed sensing using microwave heterodyne detection of spontaneous Brillouin backscatter* PhD thesis (University of Southampton, 2002).

37. Goldblatt, N. Stimulated Brillouin Scattering. *Appl. Opt.* **8,** 1559–1566. http://ao.osa.org/abstract.cfm?URI=ao-8-8-1559 (1969).

38. Wait, P. & Newson, T. Landau Placzek ratio applied to distributed fibre sensing. *Optics Communications* **122,** 141 –146. ISSN: 0030-4018. http://www.sciencedirect.com/science/article/pii/0030401895005579 (1996).

39. Masoudi, A. & Newson, T. P. Contributed Review: Distributed optical fibre dynamic strain sensing. *Review of Scientific Instruments* **87,** 011501. http://aip.scitation.org/doi/10.1063/1.4939482 (2020) (Jan. 2016).

40. Agrawal, G. *Nonlinear Fiber Optics* ISBN: 9780123970237. https://books.google.co.uk/books?id=xNvw-GDVn84C (Academic Press, 2013).

41. Koch, E. Skin attachable flexible sensor array for respiratory monitoring, 7 (2016).

42. Adnan, N. H. & Wan, K. Development of Low Cost "GloveMAP" Based on Fingertip Bending Tracking Techniques for Virtual Interaction. **12,** 12 (2012).

43. Dementyev, A., Kao, H.-L. C. & Paradiso, J. A. *SensorTape: Modular and Programmable 3D-Aware Dense Sensor Network on a Tape* en. in *Proceedings of the 28th Annual ACM Symposium on User Interface Software & Technology - UIST '15* (ACM Press, Daegu, Kyungpook, Republic of Korea, 2015), 649–658.

44. Danisch, L., Chrzanowski, A., Bond, J. & Bazanowski, M. FUSION OF GEODETIC AND MEMS SENSORS FOR INTEGRATED MONITORING AND ANALYSIS OF DEFORMATIONS, 10.

45. Keck, D. B., Maurer, R. D. & Schultz, P. C. On the ultimate lower limit of attenuation in glass optical waveguides. *Applied Physics Letters* **22,** 307–309 (Apr. 1973).

46. Berthold, J. W. in *Optical Fiber Sensor Technology: Applications and Systems* (eds Grattan, K. T. V. & Meggitt, B. T.) 225–240 (Springer US, Boston, MA, 1999). ISBN: 978-1-4757-6077-4. https://doi.org/10.1007/978-1-4757-6077-4_8.

47. Lagakos, N., Cole, J. H. & Bucaro, J. A. Microbend fiber-optic sensor. *Applied Optics* **26,** 2171 (June 1987).

48. Othonos, A. & Kalli, K. *Fiber Bragg Gratings: Fundamentals and Applications in Telecommunications and Sensing* ISBN: 9780890063446. https://books.google.co.uk/books?id=6fJRAAAAMAAJ (Artech House, 1999).

49. Miller, G. A., Askins, C. G. & Friebele, E. J. *Shape sensing using distributed fiber optic strain measurements* in (Santander, Spain, June 2004), 528. http://proceedings.spiedigitallibrary.org/proceeding.aspx?doi=10.1117/12.566653.

50. Gander, M. J. *et al.* Bend measurement using Bragg gratings in multicore fibre. *Electronics Letters* **36,** 120–121. ISSN: 0013-5194 (2000).

51. Flockhart, G. M. H. *et al.* Two-axis bend measurement with Bragg gratings in multicore optical fiber. *Opt. Lett.* **28,** 387–389. http://ol.osa.org/abstract.cfm?URI=ol-28-6-387 (2003).

52. Et al., C. *Method and Apparatus for determining the shape of a flexible body* US Patent 6,256,090 B1. 2001. http://www.google.it/patents/US4741207.

53. Davis, M. A., Kersey, A. D., Sirkis, J & Friebele, E. J. Shape and vibration mode sensing using a fiber optic Bragg grating array. *Smart Materials and Structures* **5,** 759–765. https://iopscience.iop.org/article/10.1088/0964-1726/5/6/005 (Dec. 1996).

54. Flockhart, G., Cranch, G. & Kirkendall, C. Differential phase tracking applied to Bragg gratings in multi-core fibre for high accuracy curvature measurement. en. *Electronics Letters* **42,** 390. ISSN: 00135194. https://digital-library.theiet.org/content/journals/10.1049/el_20060261 (2020) (2006).

55. Bao, X. & Chen, L. Recent Progress in Distributed Fiber Optic Sensors. *Sensors* **12,** 8601–8639. ISSN: 1424-8220. http://www.mdpi.com/1424-8220/12/7/8601 (June 2012).

56. Lu, P. *et al.* Distributed optical fiber sensing: Review and perspective. *Applied Physics Reviews* **6,** 041302. http://aip.scitation.org/doi/10.1063/1.5113955 (Sept. 2019).

57. Zhao, S. *et al.* Performance Investigation of OFDR Sensing System With a Wide Strain Measurement Range. *JOURNAL OF LIGHTWAVE TECHNOLOGY* **37,** 7 (2019).

58. Yang Du *et al.* Cryogenic Temperature Measurement Using Rayleigh Backscattering Spectra Shift by OFDR. en. *IEEE Photonics Technology Letters* **26,** 1150–1153. ISSN: 1041-1135, 1941-0174. http://ieeexplore.ieee.org/document/6804638/ (2020) (June 2014).

59. Kreger, S. T., Gifford, D. K., Froggatt, M. E., Soller, B. J. & Wolfe, M. S. *High Resolution Distributed Strain or Temperature Measurements in Single- and Multi-Mode Fiber Using Swept-Wavelength Interferometry* en. in *Optical Fiber Sensors* (OSA, Cancún, Mexico, 2006), ThE42. ISBN: 978-1-55752-817-9. https://www.osapublishing.org/abstract.cfm?uri=OFS-2006-ThE42 (2020).

60. Lally, E. M., Reaves, M., Horell, E., Lute, S. & Frogatt, M. *Fiber optic shape sensing for monitoring of flexible structures* in *Proc.SPIE* **8345** (SPIE, 2012), 83452 –83459.

61. Duncan, R. G. *et al. High-accuracy fiber-optic shape sensing* in (ed Peters, K. J.) (San Diego, California, Apr. 2007), 65301S. http://proceedings.spiedigitallibrary.org/proceeding.aspx?doi=10.1117/12.720914.

62. Froggatt, M. E. & Duncan, R. G. *pat.*

63. Rogge, M. D. & Moore, J. P. *pat.*

64. Chan, H. M. & Parker, A. R. *pat.*

65. Westbrook, P. S. *et al.* Continuous Multicore Optical Fiber Grating Arrays for Distributed Sensing Applications. *Journal of Lightwave Technology* **35,** 1248–1252. http://ieeexplore.ieee.org/document/7849199/ (Mar. 2017).

66. Westbrook, P. S. *et al. Integrated optical fiber shape sensor modules based on twisted multicore fiber grating arrays* in (ed Gannot, I.) (San Francisco, California, United States, Feb. 2014), 89380H. http://proceedings.spiedigitallibrary.org/proceeding.aspx?doi=10.1117/12.2041775.

67. Horiguchi, T. & Tateda, M. BOTDA-nondestructive measurement of single-mode optical fiber attenuation characteristics using Brillouin interaction: theory. *Journal of Lightwave Technology* **7,** 1170–1176. ISSN: 0733-8724 (1989).

68. Barnoski, M. K. & Jensen, S. M. Fiber waveguides: a novel technique for investigating attenuation characteristics. *Appl. Opt.* **15,** 2112–2115. http://ao.osa.org/abstract.cfm?URI=ao-15-9-2112 (1976).

69. Bergman, A. M. A. & Tur, M. State of the art of Brillouin fiber-optic distributed sensing. *Optics & Laser Technology* **78,** 81 –103. ISSN: 0030-3992. http://www.sciencedirect.com/science/article/pii/S0030399215002571 (2016).

70. Galindez, C. & Lopez-Higuera, J. Brillouin Distributed Fiber Sensors: An Overview and Applications. **2012** (Oct. 2012).

71. Zhao, Z., Soto, M. A., Tang, M. & Thévenaz, L. Distributed shape sensing using Brillouin scattering in multi-core fibers. *Opt. Express* **24,** 25211–25223. http://www.opticsexpress.org/abstract.cfm?URI=oe-24-22-25211 (2016).

72. Pytel, A., Kolakowska, A., Jozwik, M., Szostkiewicz, L. & Yandg, Z. *Brillouin scattering effect in the multicore optical fiber applied to fiber optic shape sensing* in *Proc.SPIE* **10435** (SPIE, 2017), 104350N1–7.

73. Ba, D. *et al.* A High-Performance and Temperature-Insensitive Shape Sensor Based on DPP-BOTDA. *IEEE Photonics Journal* **10,** 1–10 (2018).

74. Shimizu, K., Horiguchi, T., Koyamada, Y. & Kurashima, T. Coherent self-heterodyne detection of spontaneously Brillouin-scattered light waves in a single-mode fiber. *Opt. Lett.* **18,** 185–187. http://ol.osa.org/abstract.cfm?URI=ol-18-3-185 (1993).

75. Fellay, A., Thévenaz, L., Facchini, M., Niklès, M. & Robert, P. *Distributed sensing using stimulated Brillouin scattering : towards ultimate resolution.* in *12th International Conference on Optical Fiber Sensors* (OSA, Williamsburg, Virginia, 1997), OWD3. https://www.osapublishing.org/abstract.cfm?uri=OFS-1997-OWD3.

76. Coscetta, A., Minardo, A. & Zeni, L. Distributed Dynamic Strain Sensing Based on Brillouin Scattering in Optical Fibers. en. *Sensors* **20,** 5629. ISSN: 1424-8220 (Oct. 2020).

77. Horiguchi, T., Kurashima, T. & Koyamada, Y. *Measurement of temperature and strain distribution by Brillouin frequency shift in silica optical fibers* in (eds Dakin, J. P. & Kersey, A. D.) (Boston, MA, Mar. 1993), 2–13. http://proceedings.spiedigitallibrary.org/proceeding.aspx?articleid=1001262.

78. Horiguchi, T., Shimizu, K., Kurashima, T., Tateda, M. & Koyamada, Y. Development of a distributed sensing technique using Brillouin scattering. *Journal of Lightwave Technology* **13,** 1296–1302. http://ieeexplore.ieee.org/document/400684/ (July 1995).

79. Horiguchi, T., Kurashima, T. & Tateda, M. Tensile strain dependence of Brillouin frequency shift in silica optical fibers. *IEEE Photonics Technology Letters* **1,** 107–108 (May 1989).

80. Lee, B. Review of the present status of optical fiber sensors. *Optical Fiber Technology* **9,** 57–79. https://linkinghub.elsevier.com/retrieve/pii/S1068520002005278 (Apr. 2003).

81. Annamdas, K. K. K. & Annamdas, V. G. M. *Review on developments in fiber optical sensors and applications* in (eds Mendez, A., Du, H. H., Wang, A., Udd, E. & Mihailov, S. J.) (Orlando, Florida, Apr. 2010), 76770R.

82. Lopez-Higuera, J. M., Rodriguez Cobo, L., Quintela Incera, A. & Cobo, A. Fiber Optic Sensors in Structural Health Monitoring. *Journal of Lightwave Technology* **29,** 587–608. http://ieeexplore.ieee.org/document/5709958/ (Feb. 2011).

83. Barrias, A., Casas, J. & Villalba, S. A Review of Distributed Optical Fiber Sensors for Civil Engineering Applications. *Sensors* **16,** 748. ISSN: 1424-8220. http://www.mdpi.com/1424-8220/16/5/748 (May 2016).

84. Amanzadeh, M., Aminossadati, S., Kizil, M. & Rakić, A. D. Recent developments in fibre optic shape sensing. *Measurement* **128,** 119 –137. ISSN: 0263-2241. http://www.sciencedirect.com/science/article/pii/S0263224118305608 (2018).

85. Du, C., Dutta, S., Kurup, P., Yu, T. & Wang, X. A review of railway infrastructure monitoring using fiber optic sensors. *Sensors and Actuators A: Physical* **303,** 111728 (Mar. 2020).

86. Wu, T., Liu, G., Fu, S. & Xing, F. Recent Progress of Fiber-Optic Sensors for the Structural Health Monitoring of Civil Infrastructure. *Sensors* **20,** 4517. https://www.mdpi.com/1424-8220/20/16/4517 (Aug. 2020).

87. Floris, I., Adam, J. M., Calderón, P. A. & Sales, S. Fiber Optic Shape Sensors: A comprehensive review. *Optics and Lasers in Engineering* **139,** 106508. https://linkinghub.elsevier.com/retrieve/pii/S0143816620319461 (Apr. 2021).

88. *Bariatric Robotic Surgery: A Comprehensive Guide* (eds Domene, C. E., Kim, K. C., Vilallonga Puy, R. & Volpe, P.) http://link.springer.com/10.1007/978-3-030-17223-7 (Springer International Publishing, Cham, 2019).

89. Laby, K. P. *et al. pat.*

90. Gue, C. Y. *et al.* The monitoring of an existing cast iron tunnel with distributed fibre optic sensing (DFOS). *Journal of Civil Structural Health Monitoring* **5,** 573–586. http://link.springer.com/10.1007/s13349-015-0109-8 (Nov. 2015).

91. Piccolo, A *et al.* Tunnel convergence analysis by distributed optical fiber strain sensing with means of finite element – inverse analysis method, 13.

92. Templeton, E. H., Kominsky, D., Brown, T. & Nesnas, I. *A Novel Sensing Tether for Rovers* in *2018 AIAA Aerospace Sciences Meeting* (American Institute of Aeronautics and Astronautics, Kissimmee, Florida, Jan. 2018). https://arc.aiaa.org/doi/10.2514/6.2018-1534.

93. Mori, T. *et al.* Silica glass tubes by new sol-gel method. *Journal of Non-Crystalline Solids* **100,** 523–525. ISSN: 00223093. https://linkinghub.elsevier.com/retrieve/pii/0022309388900762 (Mar. 1988).

94. Yamamoto, J. *et al. Fabrication of Multi Core Fiber by Using Slurry Casting Method* in *Optical Fiber Communication Conference* (OSA, Los Angeles, California, 2017), Th1H.5.

95. Samir, Perpar & Batagelj. *Fabrication of a single-mode seven-core optical fiber using the stack-and-draw procedure* in *2016 International Workshop on Fiber Optics in Access Network (FOAN)* (IEEE, Lisbon, Portugal, Oct. 2016), 1–4. http://ieeexplore.ieee.org/document/7764545/.

96. Nagel, S., MacChesney, J. & Walker, K. An Overview of the Modified Chemical Vapor Deposition (MCVD) Process and Performance. *IEEE Transactions on Microwave Theory and Techniques* **30,** 305–322 (1982).

97. Lewin, M. & Preston, J. *Handbook of Fiber Science and Technology Volume 2: High Technology Fibers: Part B* (Taylor & Francis, 1989).

98. Cooper, L. J. *Fabrication of novel geometry fibre lasers for high power applications* , 2005. https://eprints.soton.ac.uk/38958/.

99. Oh, K. & Paek, U. *Silica Optical Fiber Technology for Devices and Components: Design, Fabrication, and International Standards* (Wiley, 2012).

100. Hibbeler, R. *Mechanics of Materials* (Pearson, 2016).

101. Petermann, I., Sahlgren, B., Helmfrid, S., Friberg, A. T. & Fonjallaz, P.-Y. Fabrication of advanced fiber Bragg gratings by use of sequential writing with a continuous-wave ultraviolet laser source. *Applied Optics* **41,** 1051. https://www.osapublishing.org/abstract.cfm?URI=ao-41-6-1051 (Feb. 2002).

102. DeLange, O. E. Optical heterodyne detection. *IEEE Spectrum* **5,** 77–85. http://ieeexplore.ieee.org/document/5215385/ (Oct. 1968).

103. Shannon, C. E. Communication in the Presence of Noise. *PROCEEDINGS OF THE IEEE* **86,** 11 (1998).

104. Hagen, J. B. Radio-Frequency Electronics: Circuits and Applications, Second Edition, 455.

105. Bobrow, L. *Fundamentals of Electrical Engineering* (Oxford University Press, 1996).

106. Alahbabi, M. N., Lawrence, N. P., Cho, Y. T. & Newson, T. P. High spatial resolution microwave detection system for Brillouin-based distributed temperature and strain sensors. *Measurement Science and Technology* **15,** 1539–1543 (July 2004).

107. Mizuno, Y., Hayashi, N., Tanaka, H., Wada, Y. & Nakamura, K. Brillouin scattering in multi-core optical fibers for sensing applications. *Scientific reports* **5,** 1–9 (2015).

108. Maughan, S. M., Kee, H. H. & Newson, T. P. Simultaneous distributed fibre temperature and strain sensor using microwave coherent detection of spontaneous Brillouin backscatter. *Measurement Science and Technology* **12,** 834–842 (June 2001).

109. Yablon, A. D. *Optical fiber fusion splicing Springer series in optical sciences* **v. 103** (Springer, Berlin ; New York, 2005).

110. Milne, D., Masoudi, A., Ferro, E., Watson, G. & Le Pen, L. An analysis of railway track behaviour based on distributed optical fibre acoustic sensing. en. *Mechanical Systems and Signal Processing* **142,** 106769 (Aug. 2020).

111. Budynas, R. G., Nisbett, J. K. & Shigley, J. E. *Shigley's mechanical engineering design* Eleventh edition (McGraw-Hill Education, New York, NY, 2020).

112. Khan, F. *et al.* Multi-Core Optical Fibers With Bragg Gratings as Shape Sensor for Flexible Medical Instruments. *IEEE Sensors Journal* **19,** 5878–5884 (July 2019).

113. Komanec, M. *et al.* Low-Loss and Low-Back-Reflection Hollow-Core to Standard Fiber Interconnection. *IEEE Photonics Technology Letters* **31,** 723–726 (2019).

114. Van Rossum, G. & Drake, F. L. *Python 3.8.3 Reference Manual* (2020).

115. *Keysight InfiniiVision 3000T X-Series Oscilloscopes Programmer's Guide* English. Version 07.21.0001. Keysight Technologies (). 1714 pp.